MODELLING THE ELECTRONEGATIVE DISCHARGE

A thesis for the degree of

PHILOSOPHIAE DOCTOR

Presented to

DUBLIN CITY UNIVERSITY

By

Derek Monahan
School of Physical Sciences
Dublin City University

Research Supervisor:
Prof. Miles M. Turner

External Examiner: Prof. Michael A. Lieberman
Internal Examiner: Dr. Tony Cafolla

August 2007

Declaration

I hereby certify that this material which I now submit for assessment on the programme of study leading to the award of Philosophiae Doctor is entirely my own work and has not been taken from the work of others save and to the extent that such work has been cited and acknowledged within the text of my work.

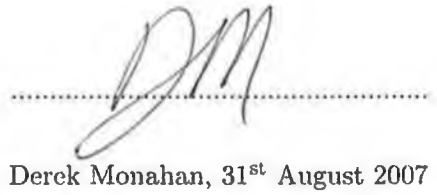

Derek Monahan, 31st August 2007

ID No.: 53143647

Abstract

A one-dimensional particle-in-cell simulation incorporating Monte Carlo collisions (PIC-MCC) has been utilized to investigate a model Ar/O_2 discharge. This benchmarking study is unique in many respects, but most notably in the size of the parameter space it encompasses. In total, data from more than fifty self-consistent kinetic simulations, covering a wide range of conditions in terms of collisionality, electronegativity, and negative ion destruction mechanism, has been compiled. This data conveys a unique perspective of the complex charge species dynamics associated with electron attaching discharges. Under certain discharge conditions quasi-neutrality violating double layer structures are observed. A largely unappreciated negative ion heating mechanism is identified, and negative ion temperatures greatly exceeding those of the surrounding gas are observed.

A generic global, or volume-averaged, plasma chemistry model has also been developed. We utilize the benchmark simulations to critically evaluate the performance of such models over a wide range of parameters. It is found, as expected, that the most significant limitation appears to be the oft-used assumption of a Maxwellian electron energy distribution. Accounting for this deficiency is shown to improve model-simulation efficacy considerably. Although many works have been published which endeavor to incorporate the effects of self-consistent electronegative plasma segregation into models exploring the primary discharge parameters and scaling laws, it is found that the conventional global model formulation is quite robust to the occurrence of such complex state-variable profiles.

Acknowledgments

First, I would like to sincerely thank my supervisor, Prof. Miles Turner, who's advice, guidance and encouragement has been pivotal to the work presented in this thesis. I consider myself extremely fortunate to have had the opportunity to learn from such an accomplished academic and to have befriended a man for whom I have the utmost respect.

I am hugely grateful to my external examiner, Prof. Mike Lieberman, for taking the time to examine my work and for his very helpful and insightful comments. I would also like to thank my internal supervisor, Dr. Tony Cafolla, in this regard, and Prof. Allen Lichtenberg for his helpful discussions and suggestions.

Over the past four years I have gotten to know a number of people here in DCU. In no particular order, I would like to thank Dave, Shane, Chanel, Angus, Peter, Muhammad, Jim, Paul, Steward, Nial, Felipe, Ronan, Bernard, Bert, Sam, Sarah, and Sheila. As friends and colleagues I could not imagine a better bunch of people.

As much as I would like to perpetuate the common misconception that the life of a research student is all work and no play, I must concede to having enjoyed equal measures of both. This I owe largely to a group of friends who have stuck around despite our diverging paths in life. In particular I would

like to thank Dave (again!), Mark, Taz, Duff, Alan and Tommy for helping me keep some perspective and ignoring the occasional uninvited rant of a "wannabe" scientist!

I must say thank you to my brothers who have afforded me a great deal of special treatment throughout my years as the family's eternal student. I cannot over stress how important this has been on occasion. I would also like thank my uncle, Martin, for the immense help he has been to both me and my parents in recent times.

Finally, I wish to reserve my foremost acknowledgement for my parents. I truly cannot put into words my gratitude for the sacrifices you have made and the opportunities you have given me over the past twenty-six odd years. To what ever extent this work may be regarded as an achievement, I owe it entirely to you.

Contents

List of Figures

Nomenclature

This section has been included in order to facilitate reading. Any variables which are not listed will be identified upon introduction. In some instances a variable may have more than one meaning. The assumed meaning should be obvious from the context in which it is used. In a situation where confusion may arise the intended meaning will be explicitly stated.

Symbol

A	chamber surface area
B	magnetic field
C	collisional operator
D	diffusion coefficient
E, E	electric field
F	force
F	microscopic phase-space distribution function
I	kinetic source term
J	ratio of ion-ion recombination loss rate to positive ion generation rate
L	characteristic discharge dimension / planar discharge length
K	reaction rate constant; thermal conductivity
P	power / normalized attachment rate constant
Q	normalized recombination rate constant
R	reaction rate ($K \sum n$)
T	temperature (assumed to be in electron volts unless preceded by Boltzmanns constant k_B)
$T_e/T_p/T_n$	electron / positive-ion / negative-ion temperature (units of Kelvin unless otherwise stated)
V	Sagdeev potential / chamber volume
X	normalized x coordinate
Z	relative ion charge
a	acceleration
a	reaction coefficient

Symbol

e	unit charge
f	ensemble-averaged distribution function
g	statistical weight
h	ion edge density parameter
l	parabolic length scale
l_-	core half width
l_p	discharge half width
m	mass
n	particle density
p	scalar pressure
q	charge
r	radial position
t	time
v	velocity
v	directed velocity
u	speed/velocity
u	velocity
x	position vector
x	one dimensional position
x	variable EDF parameter
α	electronegativity
Γ	flux
χ	fractional core volume

Symbol

Φ,ϕ	electric potential
δ	Dirac delta function; δ_{sh}, sheath width; δ kinetic energy exchange fraction
ϵ_0	permittivity of free space
$\mathcal{E}$	energy
η	normalized potential $(-e\phi/k_B T_e)$
γ	T_g/T_e; $\gamma_k = T_k/T_e$
λ_D	Debye length
λ	mean free path; ratio of volume ion generation rate wall loss rate
ν	collision frequency; ν_m momentum transfer collision frequency
ρ	charge density
σ	reaction cross-sectional area
μ	mobility
ϑ	gas fraction

Subscripts

0	plasma edge value
B	Bohm/Boltzmann
att	electron-gas attachment
c	collision; core-edge; cold
det	ion-gas detachment
e	electron
eff	effective
ex	exhaust
g	gas
h	hot
i	ion index; ion summation index
iz	ionization
j	integer; summation index
n	negative ion
p	positive ion; positive edge
rec	ion-ion recombination
rece	electron-ion recombination
s	sheath edge; sound
sh	sheath
+	net positive ion value; positive charge
-	net negative ion value; negative charge; core edge
th	thermal
th	threshold
*, **	metastables

Acronyms

EEDF	electron energy distribution function
EPF	energy probability function
DL	double layer
ICP	Inductively coupled plasma
MCC	Monte Carlo Collisions
ODE	Ordinary Differential Equation
PDE	Partial Differential Equation
PIC	particle in cell
lhs	left hand side
rf	radio frequency
rhs	right hand side
wrt	with respect to

CHAPTER

1 Introduction

Electronegative plasmas have been the subject of much research and debate for some time now. Over the past twenty years a myriad of models, theories and observations have accrued in the literature in relation to this topic. Some of this work has met with strong criticism and, for an extended period, it has been unclear which models/assumptions were most acceptable, or to what extent these models could be trusted. This situation has improved considerably in recent years, with a great deal of revision, refinement and clarification of previous work. It can now be argued that a reasonably consistent and broadly accepted view, at least of the fundamentals, has begun to emerge.

Due to the complex nature of such discharges, most studies have restricted themselves to very limited parameter spaces, with restrictions on the neutral pressure, the number of ion species, the electron/ion temperatures, and the negative-ion destruction chemistry, being common. In this work we aim to depart from this trend and assemble a set of benchmark simulations covering a relatively large parameter space.

A self-consistent, one-dimensional particle-in-cell (PIC) simulation was used to generate a detailed picture of a model electronegative discharge in the collisionless, transitional, and collisional regimes. The affect of diluting this model gas with a second electropositive gas is also examined. The model gases chosen were O_2 and Ar, due to their well studied chemistry and industrial relevance. In order to investigate both the attachment-dominated and recombination-dominated limits, the background gas composition was also manipulated.

1.1 Thesis Outline

For the benefit of the reader, the remainder of this first chapter will be devoted to briefly revising some of the elementary processes and analytical techniques which are central to the study of electronegative plasmas. With this insight, we will attempt to review the large body of literature relating to the study of these systems in the proceeding chapter. The simulations employed in this study will be discussed in chapter 3, while their output and associated analysis will be presented in chapter 4. In the penultimate chapter we will utilize this benchmark simulation data-set to mount an investigation into the limits and fidelity of the oft-used global model approximation when applied to structured electronegative discharges. Our findings and conclusions will be summarized in chapter 6.

1.2 Basic Plasma Dynamics

The Navier-Stokes equation, adopted to model the macroscopic motion of charge particles immersed in an electromagnetic field, may be expressed as follows [1]

$$mn\left[\frac{\partial \boldsymbol{u}}{\partial t} + \boldsymbol{u}\boldsymbol{\nabla}\cdot\boldsymbol{u}\right] = qn(\boldsymbol{E} + \boldsymbol{u}\times\boldsymbol{B}) - \boldsymbol{\nabla}p + \boldsymbol{f}|_c \tag{1.1}$$

where isotropic pressure has been assumed. Deferring for now the interpretation of the terms contained in equation (1.1), we may reduce the equation to a form more relevant to the discharges discussed in this work by assuming: (1) collisions with neutrals are dominant; (2) frictional forces due to particle source and sinks can be ignored; (3) the magnetic field forces are negligible. This leads to the following steady-state *momentum conservation* equation

$$mn\boldsymbol{u}\boldsymbol{\nabla}\cdot\boldsymbol{u} = qn\boldsymbol{E} - \boldsymbol{\nabla}p - mn\nu_m\boldsymbol{u} \tag{1.2}$$

where $\boldsymbol{u}\boldsymbol{\nabla}\cdot\boldsymbol{u}$, the convective acceleration, is a steady-state acceleration due to any change in velocity with changing position, $q\boldsymbol{E}$ is the force on the flow due to the local electric field, $\boldsymbol{\nabla}p$ is force per unit volume on the flow due to pressure gradients, and $mn\nu_m\boldsymbol{u}$ is the rate at which the flows momentum is lost due to collisions (characterized by the momentum transfer collision frequency, ν_m).

The convective acceleration term is clearly non-linear and posses significant difficulty when attempting to obtain analytic solutions to equation (1.2). Thus we typically make further assumptions regarding the collisionality of the flow.

For intermediate to highly collisional flows, the rhs (right hand side) terms dominate the term on the lhs (left hand side), so we may simply neglect convective acceleration. Solving the resulting linear algebraic equation for $\boldsymbol{u}$ (assuming isothermal closure for p) gives

$$u = \frac{qE}{m\nu_m} - \frac{k_B T}{m\nu_m}\frac{\nabla n}{n} \tag{1.3}$$

which may be expressed in the form of a *drift-diffusion* equation [1]

$$\Gamma = \pm \mu n E - D\nabla n \tag{1.4}$$

where μ and D are the macroscopic mobility and diffusion constants, respectively.

In the opposite pressure limit (i.e. the limit of collisionless flow) the collision and pressure terms in equation (1.2) may typically be ignored. Assuming one dimensional cold particle flow and integrating the flow from a point x to a point x' yields

$$\frac{1}{2}mu^2(x', x) = q[\phi(x') - \phi(x)] \tag{1.5}$$

which is simply an energy conservation relation for charged particle moving under the influence of a potential field.

Alternatively, for flows with very small values of m or u we may neglect the collision and convective terms and find

$$cnE + \nabla p = 0 \tag{1.6}$$

which, again assuming isothermal closure, can be integrated to find the spatial distribution of n as a function of potential

$$n(x', x) = n_0 \exp(-q\phi(x)/k_B T) \tag{1.7}$$

where n_0 is the density at the point defined by $\phi(x) = 0$. This is the well-known Boltzmann relation for the distribution of charged particles in an

electric potential.

One may use equations (1.5) and (1.7) to construct a self-consistent model of a low pressure discharge composed of electrons and singly charged ions. This was first done by Tonks and Langmuir [2] yielding the following expression for the charge particle density profile [1]

$$n(x) = \left(\frac{m_p}{2e}\right) \int_0^x \frac{\nu_{iz} n(x') \mathrm{d}x'}{[\phi(x') - \phi(x)]^{1/2}} \tag{1.8}$$

where it has been assumed that electron-ion pairs are produced in collisions of the form $\nu_{iz} n$. This simple kinetic model is often referred to as the *ion free-fall model*, as ions simply "fall" unperturbed through the monotonic potential.

1.3 Debye Shielding

Applying an electric field to an overall neutral system of charged particles causes oppositely charged particles to move in opposite directions. However, increasing macroscopic charge separation produces an increasing electric field in the direction opposite to that of the applied field. A steady-state is reached when these two electric forces cancel each other out and the net electric field in the system is zero. This phenomena, whereby charge polarization effectively shields out externally applied electric fields, is known as *Debye shielding*.

In quasi-neutral plasma systems, the electric field is not completely shielded, but instead decays exponentially as it penetrates into the plasma according to [3] (in the case of a one-dimensional plasma)

$$\boldsymbol{E} = \boldsymbol{E_0} \exp\left(-\frac{x}{\lambda_D}\right) \tag{1.9}$$

where λ_D is a parameter known as the *Debye length* and corresponds to the length scale over which an electric field penetrating into a plasma is reduced by a factor of e^{-1}.

Assuming both electrons and ions are in Boltzmann equilibrium, solving Poisson's equation at a point far from the discharge edge where ($e\phi \ll T_e, T_p$), one may obtain the following approximate expression for λ_D [3]

$$\lambda_D = \sqrt{\frac{\epsilon_0}{n_{e0}e^2(1/k_BT_e + 1/k_BT_p)}} \qquad k_BT_e, k_BT_p \ll -e\phi \tag{1.10}$$

Thus, if $k_BT_e \gg k_BT_p$, as is typically the case in low temperature plasmas, one may conclude that λ_D is characterized by the positive ion temperature.

A moment's contemplation shows that this conclusion is unsatisfactory. Due to their much lower mass, it is the electrons which move to shield the electric field, reducing it appreciably before the ions have a chance to respond. Therefore, it is their temperature which, one may reasonably conclude, should characterize this shielding length [3].

Of course the flaw in our original argument was applying the assumption of Boltzmann equilibrium to the positive ions. Instead, assuming stationary (cold) ions and Boltzmann electrons, one can re-derive equation (1.10) and obtain the conventional expression for the Debye length [1]

$$\lambda_D = \sqrt{\frac{\epsilon_0 k_B T_e}{n_{e0}e^2}} \tag{1.11}$$

More generally, equation (1.10) may be re-derived assuming n_n negative species, all of which are in thermal equilibrium with the local electric field. This yields

$$\lambda_D = \sqrt{\frac{\epsilon_0}{n_{e0}e^2 \sum_{k=0} n_n \left[\frac{\alpha_{k0}}{k_B T_k}\right]}} \qquad k_B T_e, k_B T_k \gg -e\phi \quad \forall k \tag{1.12}$$

where $\alpha_{k0} \equiv n_{k0}/n_{e0}$.

Equation (1.12) applies to plasmas having more than one negative charge species in thermal equilibrium, such as those containing two distinct electron populations; one hot and one cold. In such plasma, it is clear from equation (1.12) that the temperature of the cooler species will greatly influence the shielding length.

Another example of such a plasma is an electronegative plasma, where it has been found that, at low pressures, the spatial distribution of negative ions may be well approximated by assuming they Boltzmann equilibrium. Sheridan *et al.* [4] note that, in this case

> ... the negative ions assume the role of electrons in a two-component plasma, with the ion-acoustic velocity and Debye length determined largely by the negative ion temperature.

But how is it that the assumption of Boltzmann equilibrium may be applied to the negative ions (at low pressure) but not to positive ions?

Typically, much cooler (relative to the electrons) negative ions are confined to regions of very low field. Therefore, their drift velocities are typically small relative to their thermal motion. This clearly must be the case, as negative ions cannot access regions in which $k_B T_n \ll |e\phi| < k_B T_e$, and are quickly expelled when formed there. Thus, regions in which the assumption of Boltzmann equilibrium for negative ions must break down are conveniently depleted of negative ions. However, if negative ions are nec-

essarily confined to regions of low field, they can play no part in shielding until the field has been sufficiently reduced!

Thus, plasmas containing negative ions do have a superior ability to shield electric fields in accordance with equation (1.12) (with $T_n \ll T_e$). However, implicit in this statement is the understanding that they may only do so after an extended region in which the fields are shielded on a scale-length given by the conventional electropositive Debye length.

1.4 The Bohm Criterion

Exploiting mathematical simialrites between the equations of compressible fluid flow and those of the cold ion plasma approximation, Stangeby and Allen [5] re-derived the electropositive Bohm criterion and demonstrated its equivalence to the ion sound speed. Here we show that this analysis can be extend to plasmas containing negative ions in thermal equilibrium. Though the extension is relatively trivial, we do not know of any previous work in which this has been done. While the relation obtained for Bohm speed is simply the conventional electronegative expression, there is a subtle incisive quality to their final conclusion which other derivations lack.

Equation (1.1) may be rewritten for a collisionless, zero-temperature flow of singly charged ions, as follows [5]

$$\frac{D\boldsymbol{u}}{Dt} = \frac{e\boldsymbol{E}}{m_p} \tag{1.13}$$

where D/Dt is the convective derivative. Applying the vector identities $(\boldsymbol{u}\nabla)\boldsymbol{u} = (\nabla \times \boldsymbol{u}) \times \boldsymbol{u} + \nabla(u^2/2)$ and $\boldsymbol{a} \times \boldsymbol{b} = -\boldsymbol{b} \times \boldsymbol{a}$ one gets

$$\frac{\partial \boldsymbol{u}}{\partial t} + \nabla\left(\frac{u^2}{2}\right) - \boldsymbol{u} \times \boldsymbol{w} = \frac{e\boldsymbol{E}}{m_p} \tag{1.14}$$

where $\boldsymbol{w}$ is the flow rotation (or vorticity) given by

$$\boldsymbol{w} = \nabla \times \boldsymbol{u} \tag{1.15}$$

Comparing equations (1.13) and (1.14), we see that $\boldsymbol{w} \equiv 0 \Rightarrow$ the flow may be classed as irrotational.

Expressing $\boldsymbol{E}$ as the gradient of a scalar (the potential) and applying Stokes theorem, Stangeby and Allen show that Kelvins theorem applies to the flow and therefore, if at one time or position the flow is irrotational, it cannot subsequently acquire rotation. Assuming the flow originates from a point of zero rotation, it may therefore be assumed that $\boldsymbol{w} = 0$ everywhere.

Next, we introduce the abstract notion of a velocity potential, χ, defined as

$$\boldsymbol{u} = -\nabla\chi \tag{1.16}$$

Assuming an electronegative plasma in which both electrons and negative ions are in thermal equilibrium with the electric field, quasi-neutrality may be expressed as

$$n_p = n_e + n_n = \zeta_e n_{p0} \exp\Big(\frac{e\phi}{k_B T_e}\Big) + \zeta_n n_{p0} \exp\Big(\gamma_n \frac{e\phi}{k_B T_e}\Big) \tag{1.17}$$

where

$$\zeta_e = \frac{1}{1+\alpha} \qquad \zeta_n = \frac{\alpha}{1+\alpha} \tag{1.18}$$

Ignoring source terms, the steady-state continuity equation is

$$\nabla \cdot (n_p \boldsymbol{u}) = 0 \tag{1.19}$$

$$\Rightarrow \nabla\left[\left\{\zeta_e n_{p0} \exp\left(\frac{e\phi}{k_B T_e}\right) + \zeta_n n_{p0} \exp\left(\gamma_n \frac{e\phi}{k_B T_e}\right)\right\} \cdot \nabla\chi\right] = 0 \tag{1.20}$$

Applying the chain rule to (1.20) and rearranging gives

$$\nabla^2\chi = \frac{e}{k_B T_e}\left[\frac{1+\alpha\gamma_n}{1+\alpha}\right]\nabla\chi \cdot (-\nabla\phi) \tag{1.21}$$

Rewriting (1.14), assuming steady-state, and substituting the vectors $\boldsymbol{u}$ and $\boldsymbol{E}$ with the gradients of their respective scalar potentials gives

$$\frac{1}{2}\nabla(\nabla\chi \cdot \nabla\chi) - \nabla\chi \times w = -\frac{e}{m_p}\nabla\phi \tag{1.22}$$

$$\Rightarrow -\nabla\phi = \frac{m_p}{2e}\nabla(\nabla\chi \cdot \nabla\chi) \tag{1.23}$$

Finally, substituting (1.23) into (1.21) yields

$$\nabla^2\chi = \frac{1}{2a^2}\nabla\chi \cdot \nabla(\nabla\chi \cdot \nabla\chi) \tag{1.24}$$

where

$$a = \left[\frac{k_B T_e}{m_p}\left(\frac{1+\alpha}{1+\gamma_n\alpha}\right)\right]^{1/2} \tag{1.25}$$

is the electronegative Bohm velocity.

Stangeby and Allen noted that equation (1.24) is mathematically equivalent to the fundamental equation for compressible potential fluid flow, with a interpreted as a sound speed.

Taking the gradient of equation (1.17) and rearranging gives

$$\nabla\phi = \frac{k_B T_e}{e}\left[\frac{1+\alpha}{1+\gamma_n\alpha}\right]\frac{1}{n_p}\nabla n_p \tag{1.26}$$

This may be substituted back into equation (1.23) and the latter, and most involved, part of Stangeby and Allen's analysis may be followed exactly. Thus, all conclusions drawn with respect to simple electropositive plasmas are valid for simple electronegative plasmas. Stangeby and Allen summarized their conclusions as follows [5]

> It has been demonstrated that a sufficient and necessary condition for sheath formation is that the plasma fields should accelerate the ions until their velocity normal to the sheath is equal to the Bohm speed, independent of the ion velocity component tangential to the sheath.

The physical basis for the requirement of a minimum directed positive ion energy is astutely elucidated by Chen [6]. He notes that the requirement that the space charge formed adjacent to the point at which quasi-neutrality breaks down be positive, is equivalent to the Bohm criterion (i.e. Bohm criterion $\Rightarrow \sum_j\{q_j\frac{dn_j}{d\phi}(x_s)\} > 0$). In this context it is interesting to rewrite equation (1.25) as follows

$$\frac{1}{M_p u_s^2} = \frac{n_{es}\dfrac{1}{k_B T_e} + n_{ns}\dfrac{1}{k_B T_n}}{n_s} = \frac{1}{k_B T_{en}} \tag{1.27}$$

Thus, the reciprocal of the minimum energy of directed motion possessed by the positive ions must be $\geq$ the density weighted average of the reciprocal of the negative species thermal energy, if the positive ion density is to fall more slowly than the negative ion density in the sheath. This means of averaging

is biased towards the colder of the thermal species, which makes physical sense when one considers that these will fall off most rapidly in the space charge layer, and therefore, have a greater influence on the rate at which the negative species density decreases at the sheath edge.

The seemingly universal affinity of this velocity with the quasi-neutral ion mach speed is, of course, not a mere coincidence. A short, insightful, though not necessarily original, discussion on the physical basis of this union is given by Kono in [7]. He notes that, in regions of subsonic flow, ion sound waves propagate in all directions communicating any local pressure perturbations at a finite velocity. Any electrostatic pressure differential arising in such a region is propagated throughout the plasma, and so, large pressure differentials (i.e. regions of significant space charge) are not supported in steady state (i.e. quasi-neutrality). Large space-charge/pressure gradients are necessary in the sheath region, however. If these large pressure gradients are to remain localized the quasi-neutral bulk and the space charge edge must be separated by a point of sonic ion flow.

1.5 Boundary Layer Theory

Consider the following second order ODE

$$\epsilon\frac{d^2u}{dy^2} + \frac{du}{dy} = 1; \qquad u(0) = 0, \qquad u(1) = 2, \tag{1.28}$$

where ϵ denotes a small positive constant. This is a linear homogeneous ODE with constant coefficients and so can be solved exactly, yielding

$$u = y + \frac{1 - \exp(-y/\epsilon)}{1 - \exp(-1/\epsilon)} \tag{1.29}$$

This function is plotted in figure 1.1. It can be seen from this figure (or by

analyzing the solution) that this function has two different length scales in which it differs greatly.

As $\epsilon \ll 1$, $1 - \exp(-1/\epsilon) \simeq 1$. Also $1 - \exp(-y/\epsilon) \simeq 1$ over the entire range $0 < y < 1$ except in a very narrow region close to the zero boundary in which $y = \mathcal{O}(\epsilon)$. Thus we have the macro solution

$$u_M = y + 1 \tag{1.30}$$

and the boundary layer solution

$$u_{BL} = 1 - \exp(-y/\epsilon) \tag{1.31}$$

Suppose, however, equation (1.28) could not be solved exactly. In view of the small parameter $\epsilon \ll 1$, it is possible to obtain an approximate solution.

Firstly, noting that $\epsilon \ll 1$, one may drop the second order term and immediately obtain the macro solution given above. This approximate solution should be a good estimate, except near the zero boundary, as it does not satisfy the boundary condition at $y = 0$[a]. An astute analyst will recognize that this requires a narrow boundary region adjacent to $y = 0$ in which $u(y)$ varies much more rapidly (alluding to the potential virtues of this technique in plasma physics). One may "zoom" in on this layer by appropriate change of independent variable and parameter space. Defining the new independent variable, $Y = y/\epsilon$, (1.28) becomes

$$\epsilon \frac{1}{\epsilon^2} \frac{d^2u}{dY^2} + \frac{1}{\epsilon} \frac{du}{dY} = 1 \tag{1.32}$$

Again, neglecting $\mathcal{O}(\epsilon)$ terms we may approximate (1.28) as

[a]Strictly speaking, this is due to the fact that our approximation to the solution is first order, and so it cannot be made to satisfy two boundary conditions.

$$\frac{d^2u}{dY^2} + \frac{du}{dY} = 0 \tag{1.33}$$

Now, satisfying the boundary condition at $y = 0$ gives

$$u_{BL} = A(1 - \exp(-Y)) \tag{1.34}$$

while the rhs boundary condition may be specified as

$$\lim_{Y \to \infty} u_{BL} = \lim_{y \to 0} y + 1 \tag{1.35}$$

giving $A = y + 1$. The two approximate solutions can now be combined into a single approximate solution with an error of $\mathcal{O}(\epsilon)$ and which is valid over the entire range $0 < y < 1$ by adding the two constituent solutions together and subtracting the common part

$$u \simeq y + 1 - \exp(-y/\epsilon) \tag{1.36}$$

This solution is also plotted in figure 1.1.

1.6 Double Layers

A double layer (DL) may be defined as a region in a plasma consisting of two equal but oppositely charged, essentially parallel but not necessarily plane, space charge layers [8]. The potential, electric field and space charge profiles must vary across such a layer, as shown in figure 1.2. The thickness of such structures are limited by Debye shielding to the order of a few Debye lengths (typically $\sim 10\lambda_D$ [9]). A steady-state/stationary[b] DL must, at a minimum,

[b]The existence criteria associate with transient/unstable DL's are less stringent and are discussed in [9].

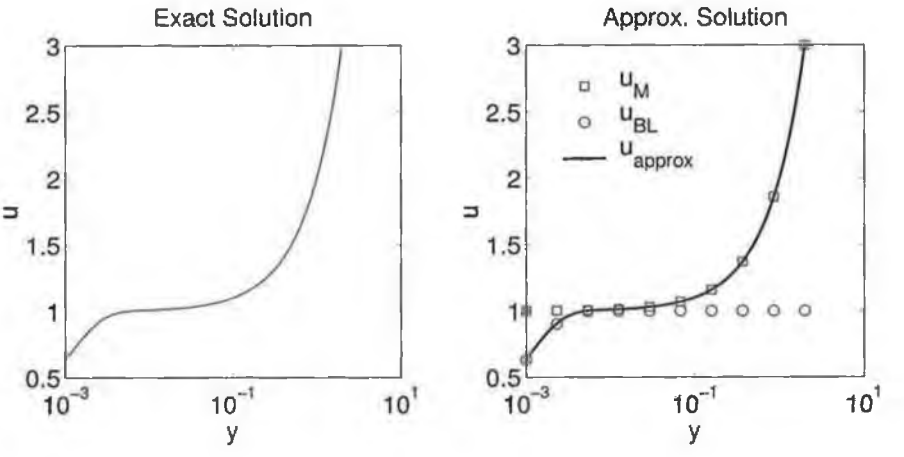

Figure 1.1: *Exact and approximate solutions to equation (1.28).*

fulfill the following three conditions [8]:

1. $|\phi_{\mathrm{DL}}| \gtrsim T$; where ϕ_0 is the potential drop across the layer and T is the temperature of the coldest plasma bordering the layer.

2. The electric field is much stronger inside the double layer than outside, so that $\int_{\mathrm{DL}} \rho(x)\mathrm{d}x \simeq 0$.

3. Quasi-neutrality is locally violated.

A fourth requirement which is typically observed, though not rigorously required, is that the charge species collisional mean free path is much greater than the DL thickness [8].

The existence of a space charge region is clearly required if there is to be a local potential gradient sandwiched between two quasi-neutral regions. A positive/negative space charge alone can easily be seen to be insufficient, if one considers the continuity of the potential. A positive/negative space charge effectively bends the potential field in its locality downward/upward from a point of zero gradient defining the first DL edge. After traversing

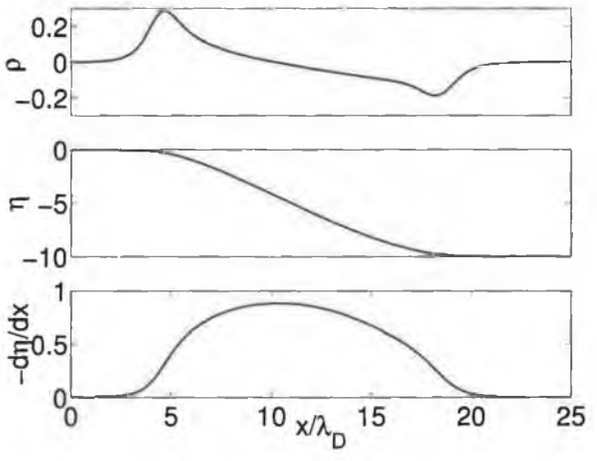

Figure 1.2: *Double layer profiles generated using the model described in [10]. ρ, η and $-d\eta/dx$ are normalized values of space charge, potential, and electric field.*

this uni-charge region, the gradient of the potential (or the electric field) must be non-zero. If one is to join this point to a quasi-neutral plasma having zero electric field, an additional space charge of equal magnitude but opposite charge is required to bend the potential profile back to a point of zero gradient.

1.6.1 Classification

There are several ways in which double layers may be classified:

- *Current-carrying/ Current-free*: Current-carrying double layers may be generated in current conducting plasmas where current related instabilities may produce localized potential gradients [11]. Current-free double layers are formed at transitions between plasmas of different characteristics[9]. We will be exclusively concerned with DL's of the later class in this work.

- *Strong/Weak*: Strong DL's are characterized by having a potential drop that is much larger than the equivalent thermal potentials of all the particle populations (free and reflected ions and electrons). In a weak DL at least one of the particle populations has an equivalent thermal potential that is of the same magnitude as, or larger than, the potential drop [12].

- *Monotonic/Oscillatory*: This classification is in reference to the potential profile across the layer. If the potential does not vary monotonically throughout the entire layer, but instead contains a number of points of inflection, it may still be referred to as a double layer (although, strictly speaking, such a structure constitutes a number of successive double layers) [8].

- *Relativistic/Non-Relativistic*: A relativistic DL is one in which the potential drop across the double layer is large enough so that both electrons and ions are accelerated to relativistic velocities in the DL [12].

It is interesting to note that the energy distribution functions of particles near a double layer are necessarily non-Maxwellian. Thus, fluid models constitute a significant simplification.

1.6.2 Double Layers and the Bohm Criterion

Of fundamental importance in understanding any space charge phenomena is, of course, Poisson's equation relating the potential and space charge spatial profiles

$$-\epsilon_0 \frac{d^2\phi}{dx^2} = \rho(x) \tag{1.37}$$

By defining the function

$$V(\phi) \equiv \int_{\phi} \rho(\chi) \mathrm{d}\chi \tag{1.38}$$

we may simply rewrite Poisson's equation, to get

$$-\epsilon_0 \frac{d^2\phi}{dx^2} = \frac{dV(\phi)}{d\phi} \tag{1.39}$$

where $V(\phi)$ is known as the classical/Sagdeev potential [9]. The analogy between equation (1.39) and the equation of motion for a damped particle moving in a potential well is often noted.

Integrating (1.39) with respect to ϕ gives [9]

$$\frac{1}{2}\epsilon_0 E^2 + V(\phi) = 0 \tag{1.40}$$

where the constant of integration is incorporated, without loss of generality, into the Sagdeev potential. Labeling the positions of the DL edges x_0 and x_{DL}, the requirement of vanishing space charge in the surrounding quasi-neutral plasma becomes

$$\left(\frac{dV}{d\phi}\right)_{\phi(x_0)} = \left(\frac{dV}{d\phi}\right)_{\phi(x_{\mathrm{DL}})} = 0 \tag{1.41}$$

while the requirement of vanishing electric field becomes

$$V(\phi(x_0)) = V(\phi(x_{\mathrm{DL}}) = 0 \tag{1.42}$$

Finally, in order to insure a non-trivial solution for $V(\phi)$, [9, 13]

$$\left(\frac{d^2V}{d\phi^2}\right)_{\phi(x_0)} = \left(\frac{d^2V}{d\phi^2}\right)_{\phi(x_{\mathrm{DL}})} = 0 \tag{1.43}$$

The physical requirement $E^2 \geq 0 \; \forall \; \phi \Rightarrow V(\phi) \leq 0 \; \forall \; \phi \Rightarrow V(\phi)$ has a local maximum at the DL edges.

Utilizing a simplified fluid description of the DL species, we may derive an expression for $V(\phi)$ and examine the physical significance of the above restrictions. The flux and momentum conservation equations for one dimensional, collisionless, generationless ion flow may be expressed as [14]

$$\frac{d}{dx} n_i u_i = \frac{du_i}{dx} + \frac{u_i}{n_i} \frac{dn_i}{dx} = 0 \tag{1.44}$$

$$m_i n_i u_i \frac{du_i}{dx} = -\frac{dp_i}{dx} + q_i n_i E \tag{1.45}$$

where $p_i = n_i k_B T_i$. This ion flow is coupled to a Boltzmann electron fluid

$$-\frac{dp_e}{dx} = e n_e E \tag{1.46}$$

via Poisson's equation. Substituting for en_e and $q_i n_i$ in Poisson's equation and rearranging gives

$$\sum_i (m_i n_i u_i^2 + p_i) + p_e - \frac{1}{2} \epsilon_0 E^2 = M_0 \tag{1.47}$$

$$\Rightarrow V(\phi) = M_0 - \left[\sum_i (m_i n_i u_i^2 + p_i) + p_e \right] \tag{1.48}$$

where M_0 is the aforementioned constant of integration and may be interpreted as the upstream momentum of the system [15]. Differentiating (1.48) once wrt ϕ gives

$$\begin{aligned}\frac{dV}{d\phi} &= -\frac{dp_e}{d\phi} - \sum_i \left(m_i n_i u_i \frac{du_i}{d\phi} + \frac{dp_i}{d\phi} \right) \\ &= -en_e + \sum_i q_i n_i\end{aligned} \tag{1.49}$$

where we have multiplied (1.45) by $dx/d\phi$ and applied the chain rule. This shows explicitly that BC (1.42) is simply a statement of quasi-neutrality at the DL edges. Substituting for $du_i/d\phi$, in (1.49), with (1.44) and differentiating wrt to ϕ gives

$$\begin{aligned}\frac{d^2V}{d\phi^2} &= -e\frac{dn_e}{d\phi} - \sum_i q_i \frac{dn_i}{d\phi} \\ &= -\frac{-e^2 n_e}{k_B T_e} + \sum_i \frac{q_i^2 n_i}{m_i u_i^2 - k_B T_i}\end{aligned} \tag{1.50}$$

Finally, applying BC (1.43) gives [15]

$$\frac{e^2 n_{e0}}{k_B T_e} \geq \sum_i \frac{q_i^2 n_i}{m_i u_i^2 - k_B T_i} \tag{1.51}$$

which is the Bohm criterion for a multicomponent plasma.

Thus, we see that the Bohm criterion must be satisfied at the edge of a quasi-neutrality violating DL. This should not be too surprising, as we have already established in section 1.4 that the Bohm criterion is a sufficient *and necessary* condition for space charge violation in simple electropositive and electronegative discharges.

1.6.3 Series Expansion for Weak Double Layers

Another approach often used analytically to investigate/predict small-amplitude (weak) DL structure/existence criteria, is to expand $V(\phi)$ for small ϕ as fol-

lows [9]

$$-V(\phi) = A_1\phi^2 + A2\phi^3 + A_3\phi^4 + \cdots \tag{1.52}$$

However, this method has in some cases been applied recklessly, erroneously predicted the existence of DL's in models containing only one thermal species (and one or more cold ion species of unspecified charge). Verheest and Hellberg [13] showed that the "forgotten" terms in the expansion *may* overwhelm the lower order terms, irrespective of the order of the expansion! Using more careful analysis they demonstrate that one needs at least two thermal species if a DL is to be formed. Physically, they note that these two thermal species are required to support the pressure differential across the DL.

CHAPTER

2

Literature Review

In this chapter, we will endeavor to review the sizable body of work published on the subject of low pressure electronegative discharges. In an effort to limit this critique to a sensible length, it is useful to separate this work into two categories; pre- and post- 1980's. This critical time is defined by the publication of a highly influential paper by Edgley and von Engel [16]. Their work signaled a notable advancement in the field of electronegative plasma simulation and was published at a time when industrial interest in plasmas (and more importantly, in electronegative plasmas) was on the cusp of a period of rapid growth. We will begin our review at this point in time, and proceed in a predominantly chronological fashion.

Earlier works by authors such as Boyd [17], Emeleus and Woolsey [18], and Thompson [19] will be referenced where appropriate. Many of the subtle, but significant, differences between electropositive and electronegative plasmas were identified by these pioneers. However, most of this work has been revised in the more recent publications.

In section 2.1 we will briefly discuss the origin of these differences,

before embarking on a more detailed review of the literature concerning its far-reaching implications in sections 2.2 and 2.3.

2.1 So "Why Are They So Different?"

This fundamental question was posed rhetorically, and subsequently addressed, in an ambitious paper by Franklin [20]. In this paper, Franklin rather loosely defines an electronegative plasma as one in which there is "such a density of negative ions that they must be taken into account". However, he subsequently concedes that ascertaining the critical density implicit in this definition is a not a trivial task. Instead, we will use a much broader definition and assume the term electronegative plasma corresponds to *any plasma formed in an electron attaching gas.* We acknowledge that this definition incorporates discharges with negligible negative ion densities, which are effectively electropositive in nature.

The principle disparity between a multi-ion electropositive plasma and a multi-ion electronegative plasma is the violation of the assumption of large mass difference between the positive and negative charge carriers (and the related assumptions of large differences in temperature and mobility). The loss of this simplifying assumption has significant implications on the transport of charge species within the plasma. In light of this, concepts such as Debye shielding, the Bohm criterion and sheath formation/structure must be re-examined (as seen in the previous chapter).

Boundary conditions and boundary transitions must also be re-examined. For example, the symmetric assumption that the flux of all charged particles increases monotonically from zero, at the discharge center, to a maximum, at the discharge edge, is lost. Lampe *et al.* [21] commented on this boundary condition, asserting that

> ...it is this boundary condition that most clearly accounts for the striking difference between electronegative and electropositive plasmas, by ruling out the self-similar essentially linear solutions that characterize electropositive plasma, and forcing the negative ions to a core/halo structure.

In addition, negative ions constitute a sink for positive ions, which are neutralized in positive-ion-negative-ion collisions. This invalidates the symmetric assumption that positive ions, created in the bulk, are destroyed exclusively at the walls, further contributing to the non-linearity of the transport equations.

2.2 Discharge Structure

2.2.1 Edgely and von Engel

In what was then regarded as one of the most comprehensive and self-consistent analysis of the positive column in electronegative gases [22], Edgley and von Engel [16] constructed a three species steady-state numerical model by coupling simplified continuity and momentum equations from fluid theory to Poisson's equation. The continuity equations had the following form

$$\nabla \cdot \Gamma_e = (\nu_{iz} - \nu_{att}) n_e + \nu_{det} n_n \tag{2.1}$$

$$\nabla \cdot \Gamma_p = \nu_{iz} n_e \tag{2.2}$$

$$\nabla \cdot \Gamma_n = \nu_{att} n_e - \nu_{det} n_n \tag{2.3}$$

where all symbols and indexing subscripts have their usual meaning (see the

nomenclature at the start of this thesis).

The momentum equations were equivalent to equation (1.2), in the previous chapter. However, due to their relatively minute mass, the inertial and collision terms were dropped from the electron momentum equation, leading to the reasonable assumption of Boltzmann equilibrium. The inertia term was also discarded from the negative ion momentum equation, due to their predicted small velocity, but the collision term was retained.

By coupling these six equations to Poisson's equation, the quasi-neutral approximation was abandoned, allowing physically realistic ion/electron boundary conditions. The resulting equation set was solved numerically leading to several important observations:

1. negative ions were completely confined to the volume, with a negligible density over an extended region adjacent to the wall.

2. the negative ion radial drift velocity was directed towards the center of the discharge under the action of the electron confining field.

3. due to the extended electropositive region close to the wall, the positive ion drift velocity approached the electropositive ion sound speed at the discharge edge.

4. n_n/n_e was a strong function of position.

2.2.2 Analytical Approach

Following on from the work of Edgley and von Engel, Ferreira *et al.* [22] attempted to formulate a more tractable model of the positive column in an electronegative discharge. In order to reduce the number of equations they made several simplifications over Edgley and von Engels' earlier work. Most notable of these was the assumption of Boltzmann equilibrium for the

negative ion species[a] and the re-introduction of the quasi-neutral assumption (physically corresponding to assumptions of low pressure and high density). In this way they reduced the number of independent parameters from seven to just two[b]. A number of physically obscure, but mathematically convenient, dimensionless parameters were introduced for the purpose of non-dimensionalising and solving the resulting pair of second order ODEs, which had the following dimensionless form:

$$\frac{1}{X}\frac{d}{dX}\left(X(1+\alpha)\frac{dG}{dX}\right)+\lambda G=0 \tag{2.4}$$

$$\frac{1}{X}\frac{d}{dX}\left(X\alpha\frac{dG}{dX}\right)-\lambda(P-Q\alpha)G=0 \tag{2.5}$$

where

$$X=\frac{r}{R} \qquad \lambda=\frac{e\nu_i R^2}{\mu_p k_B T_e} \tag{2.6}$$

$$G=\frac{n_e}{n_{e0}} \qquad P=\frac{\mu_p}{\mu_n}\frac{\nu_{att}}{\nu_{iz}} \qquad Q=\frac{\mu_p}{\mu_n}\frac{\nu_{det}}{\nu_{iz}} \tag{2.7}$$

This approach and formulation was soon after adopted by Daniels and Franklin [24, 25] in the body of their early work, yielding mathematically correct expressions which were sometimes difficult to interpret physically.

While the work of Ferreira *et al.* constituted a reduction in fidelity

[a]The velocity of the negative ions is typically assumed to be small (wrt their thermal velocities) in regions where n_n is finite, due to the increased shielding of $\boldsymbol{E}$. Low pressure $\Rightarrow m_n n_n \nu_{m,n} u_n \ll e n_n \boldsymbol{E}$, $k_B T_n \nabla n_n \Rightarrow$ Boltzmann equilibrium. Owed to the much smaller value of m_e and larger value of $T_e \Rightarrow$ electrons are typically in thermal equilibrium with the fields, even at relatively large pressures. Positive ions, on the other hand, are almost never in thermal equilibrium as they typically acquire large velocities as the approach the sheath [23].

[b]It is Ferreira *et al.* who make this striking claim. However, one should note that these two equations are both second order equations, while the equations of Edgley and von Engel are all first order.

and validity over the earlier numerical work of Edgley and von Engel, it made significant advances in the analytical treatment of the electronegative discharge. The radically different formulation and parameterization in their work, made it difficult to compare the two approaches. However, extrapolating Edgley and von Engels' results to the quasi-neutral limit ($\lambda_D/R \rightarrow 0$) illustrated convergence of the two models [22].

2.2.3 Plasma Surface Interaction

One may credibly argue that it is in the transition region separating a quasi-neutral plasma and a contacting surface that the most interesting and convoluted plasma phenomena are often observed. The need for an understanding of this interaction is compounded by its obvious relevance to probe theory. An early publication in this vain was that of Braithwaite and Allen [26], in which they considered the interaction between a cylindrical probe and a low pressure electronegative plasma. Discernibly influenced by the previous work of Boyd and Thompson [17], they showed that, in the limit of free fall ion motion, the addition of a cooler negatively charged species required that the Bohm velocity be modified.

By assuming that both the electrons and negative ions are in equilibrium with the potential field Braithwaite and Allen utilized this modified Bohm criterion to derive an expression for the potential at the plasma-sheath edge in terms of negative particle temperatures and densities [26]. At the expense of some of their rigor, we may readily re-derive their result.

In the free fall regime, the velocity of a positive ion at any point, is simply that obtained by falling through a potential ϕ. Thus, from equation (1.27), one may express the potential at the electronegative sheath edge as follows

$$\frac{1}{2}m_p u_s^2 = -e\phi_- = \frac{1}{2}k_B T_{Bn} = n_-/2(n_{es}/k_B T_e + n_{ns}/k_B T_n) \tag{2.8}$$

which may be written in terms of the normalized parameters to give

$$\eta_- = \frac{1}{2}\left(\frac{1+\alpha_-}{1+\gamma_n\alpha_-}\right) \tag{2.9}$$

Utilizing the Boltzmann relation for the negative species, one may express α_- in terms of the bulk parameter α_0. Solving for α_0 we get

$$\alpha_0 = \frac{(1-2\eta_-)}{(2\gamma_n\eta_- - 1)}\exp[\eta_-(\gamma_n - 1)] \tag{2.10}$$

For a given value of η_-, α_0 is uniquely determined. However, physically it is α_0 which determines η_-, and this relationship cannot be expressed explicitly. Figure 2.1 illustrates the relationship between η_- and α_0. We see that for some values of γ_n, equation (2.10) gives a multi-valued solution for $\eta_-(\alpha_0)$. Geometrically, the maximum and minimum points are defined by $\partial\alpha_0/\partial\eta_- = 0$ (or, equivalently, $\partial\eta_-/\partial\alpha_0 = \infty$). This was shown to lead to the following inequality being satisfied when $\eta_-(\alpha_0)$ becomes multi-valued

$$\gamma \geq 5 + \sqrt{24} \simeq 9.90 \tag{2.11}$$

It was argued that the correct interpretation of this result was that a space charge sheath will form at the lowest available value of η_- and that this corresponds to the boundary potential. It later transpired, however, that this argument had been oversimplified [27]. The occurrence of multiple values for η_- actually referred to the occurrence of multiple sheath edges when the ions acquired their local sound speed with the electronegative

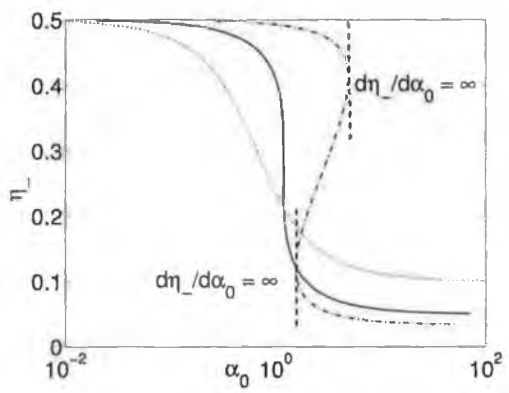

Figure 2.1: *The normalized sheath edge potential η_- as a function of α_0 according to equation (2.10).*

core. This possibility was over looked at the time [27]. We will return to this subject in section 2.3.

2.2.4 Recombination/Detachment

Of course, the earlier numerical work of Edgley and von Engel was itself a significant simplification of the dynamics underlying the electronegative discharge. Amongst other things, their model neglected temporal dynamics, the physical requirement of a power adsorption mechanism, and limited the negative ion destruction mechanisms to ion-gas detachment.

A significant improvement on their work was the spatio-temporal fluid dynamics simulations of Boeuf [28] (based on the continuum model of Graves and Jensen [29]), Oh *et al.* [30] and Meyyappan and Govindan [31]. In these works, ion-ion recombination was chosen as the method by which negative ions are destroyed, in comparison to the previous models discussed, which assumed ion-gas detachment. The choice of recombination over detachment makes the governing continuity equations non-linear [30], therefore, one may expect the dynamics in these two theoretical limits to be

fundamentally different. Catagerising discharges according to their dominant negative ion destruction mechanism (i.e. recombination-dominated or detachment-dominated[c]) had been conducive to the development of electronegative discharge theory.

2.2.5 Matched Asymptotic Analysis

Following rigidly from the work of Ferreira *et al.* Daniels and Franklin published the first in what would be a long series of papers (by Franklin at least) utilizing hydrodynamic boundary layer theory of matched asymptotic expansion (illustrated in section 1.5) to analyze the multi-scaled structure of a model electronegative gas [24]. With this powerful tool, Daniels and Franklin analytically constructed relationships between primary plasma parameters, such as α_0 and the discharge rate coefficients. As stated above, this paper utilized the same mathematically convenient, but physically obscure, dimensionless parameters as its predecessor.

In an effort to maintain cohesion, we will largely avoid the use of these parameters here. For convenience, however, exceptions to this rule are the parameters P, Q, and λ (defined in equation (2.6) and (2.7)) along with the parameter $J = K_{rec} n_{e0}/\nu_{iz}$.

Parameters P and Q acquire an obvious physical interpretation if one assumes $\mu_n/\mu_p \sim \mathcal{O}(1)$. λ may be interpreted as the ratio of the volume generated rate to the wall loss rate [33], and is typically an eigenvalue of the problem as defined by equations (2.4) and (2.5). Finally, J is the normalized ratio of ion-ion recombination loss rate to the positive-ion generation rate

[c]Here the term "recombination-dominated" is used to signify that negative ions are lost mostly/exclusively through negative-ion–positive-ion recombination. One should note, however, that some authors use the term recombination-dominated in reference to the situation where positive ion loss through recombination dominates the wall loss [32]. We will not be using the term in this context.

[34].

This initial work of Daniels and Franklin [24] elucidated the small scale boundary structure of a quasi-neutral plasma of the form treated by Ferreira et al. (i.e. detachment dominated with Boltzmann negative ions) for large values of P and Q. In this regime it was found that $\alpha \approx \alpha_0$ throughout the discharge (in agreement with [22]) and that the negative ion density was finite at the plasma edge. On the smaller sheath scale, rapid variation of the density profiles near the edge reduced the negative ion density to zero.

Soon after they extended this work to smaller values of P and Q ($1 \geq P, Q$), and identified a numerical oversight in Ferreira *et al.'s* earlier work [25]. Solving the revised system of equations numerically, they observed a diffuse top-hat like negative ion profile and an approximate Bessel function electron profile. The extent of the flat topped negative ion profile can be seen to increase with increasing P, while α_0 apparently decreases. In contrast the electron profile was found to vary very little with change in P.

Simply put, their findings equate to the statement that the core size increases with attachment. While the electronegativity, not surprisingly, decreases with increasing detachment. The "peakiness" (term used by Daniels and Franklin) of the negative ion density, along with the sensitivity of negative ion concentration on discharge parameters, indicates strongly that such discharges should be unstable, a property which had been well established in electronegative discharges [35]. Note that this analysis continues to use the quasi-neutral approximation throughout the discharge, indicating that space-charge effects are not a necessity for the formation of an abrupt negative ion profile transitions (at least in the cold ion approximation).

This work was extended to the low pressure ion free-fall regime in [36], where the effect of including a finite ion temperature could be more easily

explored. Smoother, parabolic negative ion profiles were obtained. It was found that at large γ_n and small α_0 the negative ions were again confined to a region in the discharge centre. In the limit of very large α_0 the electron density becomes exceedingly flat and, once again, the negative ions occupied the extent of the discharge. For $\alpha_0 < 1$ the negative ions continued to occupy the extent of the discharge for very low values of γ_n, but the electron profile resembled that of a simpler electron-ion plasma.

It was found that for critical values of α_0 and γ_n a discontinuity developed in the solution. When this occurred a multitude of solutions for the ion sound speed at the wall was recovered and the inequality $\gamma_n \geq 5 + \sqrt{24}$ was found to be satisfied.

Franklin *et al.* [34] also extended the analysis in [25] by replacing the linear detachment term for negative ion destruction with a quadratic positive-ion/negative-ion recombination term. They found that the accessible parameter space for such discharges was significantly restricted compared to the detachment-dominated case. Their findings were

1. $P < 1$ must be satisfied in recombination-dominated discharges (note, there is no equivalent restriction in detachment-dominated discharges).

2. the size of the core was, once again, found vary as $P^{1/2}$, but was also shown to have an inverse dependence on α_0.

3. electronegative discharges with negative ions and electron-positive ion recombination as the only loss mechanism cannot exist.

The restriction on P amounts to the requirement that the rate of creation of negative ions must be less than the rate of destruction. This is, of course, physically reasonable as negative ions are confined to the core, and so can only be destroyed there, but are created throughout the discharge.

Finally the abruptness of the transition was ascribed to the superior ability of an ion-ion plasma to shield electric fields.

Investigating the effect of finite ion temperature at higher pressures, Franklin [33] further extended [25] by including the ion temperature as an additional control parameter. The principle findings of their previous work the low pressure ion free-fall limit [36] were found to carry over. It was found that the particle fluxes were affected by inclusion of ion diffusion, but its effect on the spatial distributions was much more marked. The electric field was found to penetrate deeper into the ion-ion core as γ_i was decreased with the distinction between the two plasmas ceasing to be meaningful for $\gamma_i < 20$.

This work was later supported by results of detailed Monte-Carlo simulations compiled by Feokitistov *et al.* [37]. They found that in the non-local regime with finite ion temperature ($T_i = T_g(x)$) the discharge was stratified with a smooth diffusion broadened ion profile (in agreement with [33]). However, they also found that incorporating non-equilibrium ion diffusion[d] significantly altered the ion profiles at low pressure, essentially destroying the ion profile structure!

2.2.6 The Berkeley Group

In a departure from the mathematically rigorous, but largely qualitative, analysis of Franklin and his collaborators, an alternative approach to constructing analytically tractable solutions to the electronegative continuity equations was devised by a group of researchers, working predominantly from the University of California at Berkeley [38]. Their approach involved combining the mobility limited equations of flux for a simple three species

[d]The diffusion coefficient is modified by the non-local electric field such that $D_i(E) = \mu_i T_i + \xi m_{red} v_d^3 eE$, where $\xi = \frac{1}{3}(m+M)^3/[m(2m+M)]$ and $m_{red} = mM/(m+M)$.

electropositive plasma and rearranging in order to obtain the following, rather convoluted, expression for the positive ion flux

$$\Gamma_p = -\frac{(\mu_e + \mu_n\alpha)D_p + \mu_p(1+\alpha)D_e(\nabla ne/\nabla n_p) + \mu_p(1+\alpha)D_n(\nabla n_n/\nabla n_p)}{\mu_e + \mu_n\alpha + \mu_p(1+\alpha)}\nabla n_p \tag{2.12}$$

This expression is (by design) in the form of an ambipolar diffusion[e] expression

$$\Gamma_p = -D_{a+}\nabla n_p \tag{2.13}$$

Equation 2.12, however, offers no significant advantage over the original set of flux equations since, unlike the electropositive ambipolar coefficient, D_{a+} above is now a function of position through α and the density gradients. To overcome this, Lichtenberg *et al.* [38] assume that the negative ions were in Boltzmann equilibrium with the self-consistent fields and that μ_n/μ_e, $\mu_p/\mu_e \ll 1$, and $\gamma_n = \gamma_p = \gamma$. This yielded the more palpable expression

$$D_{a+} \simeq D_p\frac{1+\gamma+2\gamma\alpha}{1+\gamma\alpha} \tag{2.14}$$

In this form, D_{a+} is a function of position only through α. Three useful limiting cases were identified: $\alpha \gg 1 \Rightarrow D_{a+} \approx 2D_p$; $\alpha < 1$ but $\gamma\alpha$ remains $\gg 1 \Rightarrow D_{a+} \approx D_p/\alpha$; and $\gamma \ll 1$ such that $\gamma\alpha < 1 \Rightarrow D_{a+} \approx \gamma D_p$. Note that this last expression is equivalent to the electropositive approximation for D_{a+}.

By formulating an effective ambipolar diffusion equation for the posi-

[e]It has been argued, convincingly, by Franklin [39] that the term "ambipolar diffusion" is in fact a misnomer, and the term ambipolar flow is perhaps a better one. However, the former term has been widely adopted and we (as it appears the rest of the plasma physics community) shall continue to use it here.

tive ion flux, one could now patch the ion flux at the core edge to a simpler electropositive edge solution. This allowed Lichtenberg *et al.* [38] to develop approximations and and scaling laws for fundamental electronegative parameters such as l_-/l_p and α_0. To aid their analysis, these researchers presupposed electronegative-electropositive plasma segregation and inferred an approximate shape for the charged particle profiles. We will see in more detail how this is done in chapter 4.

The goal of these works was stated as [38]

> ... to develop the simplest analytical model that can predict the values of plasma quantities such as electron and negative ion densities and electron temperature ...

In this regard it was quite successful, but many of the additional assumptions required, often limited much of the observed scaling to questionably sized parameter space.

The original work of Lichtenberg *et al.* [38] was extended to lower pressures by Kouznetsov *et al.* [40] (assuming variable ion mobility), and high electronegativities by Lichtenberg *et al.* [32]. Kouznetsov *et al.* [40] allowed for the possibility that the positive ions could attain their (reduced) sound speed within the electronegative core region. Assuming the transition layer to be thin, this was modeled by a discontinuity in the ion profile at the point where $u_p = u_B$, with n_p dropping instantaneously to n_{e0}. It was, however, found that the predominant scaling laws were not significantly effected by this addition [40].

A summary of the scaling laws obtained in these works is presented in section 2.2.9.

2.2.7 Global Models

Ignoring the propensity of electronegative gases to stratify and form extremely non-uniform charged particle profiles, Lee *et al.* [41] produced one of the first spatially average investigations into the chemistry of the archetypical electronegative gas, molecular oxygen. This initial work was a relatively simple extension of the existing electropositive global model technique [42]. With this model a preliminary survey of the electronegative discharge chemistry as a function of discharge power and pressure was conducted. Ignoring ion losses to the walls, their findings were

- the total positive ion density ($O^+ + O_2^+$) increased with increase in power but was not a simple function of pressure.
- the electronegativity was observed to increase with increasing pressure and decreasing power.
- due to the dependence of fractional dissociation and electronegativity on power, T_e was no longer independent of adsorbed power.

This model was revisited and extended to Cl_2 and Ar/O_2 discharges in [43]. In this work, the one dimensional analysis of Lichtenberg *et al.* [38] was employed to generalize the simplified ion transport model of Godyak and Maximov [44] (in a heuristic manner) to include transitions from electropositive to electronegative regions and from low to high pressure. Kouznetsov [40], and later Kim [45, 46], derived similar expressions under different assumptions. These models are compared and assessed in Appendix C.

Incorporating results from finite dimensional analysis has become a feature of electronegative global models [45, 47, 48, 49], we will return to this subject in more detail in chapter 5.

2.2.8 Controversy

Prior to the first publication of Lichtenberg *et al.* [38] on the topic, attempts to extend the theory of ambipolar diffusion to the electronegative regime had existed for some time [19]. However, subsequent publications argued/demonstrated that such extensions were invalid (or at least not useful) [25, 50, 51] and should be abandoned. The authors of [38] were undoubtedly aware of this, however, their desire to reduce the charged particle transport equations to an analytically tractable form required that significant assumptions be made.

An important paper acknowledging the emergence of two distinct and seemingly irreconcilable approaches to electronegative discharge theory was published by Franklin and Snell in 1999 [52]. This paper had a commendable goal which was summarized as

> ...to relate [our previous work] to a parallel strand of activity, based essentially at Berkeley, treating essentially the same problem(s) ... Their emphasis has been on the physics and thus there are points of similarity and dissimilarity, but the basic equations are identical and therefore ultimately the different approaches must be brought into coincidence or their differences explained away in both a rational and satisfying manner.

While the bulk of this paper comprises a review of the authors previous publications, it is also largely concerned with voicing criticism of the work of the, so called, "Berkeley group" [23, 32, 38, 40]. Although it does not appear to have been noted elsewhere, much of this criticism (which is reiterated in several later publications [20, 53, 54]) appears to be unfounded.

Franklin drew attention to the fact that it was physically inconsistent

to simultaneously assume constant electronegativity and Boltzmann equilibrium for both negative species, unless $T_n = T_e$. While this is correct, his assertion that the authors affiliated to the Berkeley group made these assumptions is erroneous.

As discussed by Rogoff [50], the concept of ambipolar diffusion is, strictly speaking, broadly applicable and can be generally defined. However, in many cases it does not offer any simplification over the use of the full set of coupled transport equations, and essentially loses its meaning. In fact, somewhat contrary to their repeated assertions that the concept of ambipolar diffusion should be forsaken when more than one ion species is present, Franklin and Snell [52] themselves identify a region in parameter space which they deemed to be reasonably well modeled by an electronegative ambipolar flux equation (detachment dominated, collisional limit). Assuming constant electronegativity, but not assuming Boltzmann equilibrium for the negative ions, they derive the corresponding ambipolar diffusion coefficient

$$D_{a+} = D_p \frac{\mu_e(1+\gamma_p) + \alpha_0\mu_n(\frac{\gamma_p}{\gamma_n}+1)}{\mu_e + \mu_p + \alpha_0(\mu_n + \mu_p)} \tag{2.15}$$

In contrast, the Berkeley group derived their ambipolar diffusion coefficient assuming lower pressures so that both negative species were essentially in thermal equilibrium. This led to the expressions given for D_{a+} in section 2.2.6, where it was shown that, by assuming $\alpha \gg 1$, D_{a+} can be approximated by a constant ($= 2D_p$) in the electronegative core region. This is clearly not equivalent to assuming that α is constant.

Franklin and Snell tested equations (2.15) and (2.14) for physical consistency in several limiting regimes. They claimed that only their expression passes all these tests, while equation (2.14) only passed one. In Appendix A we shall show that this, surprisingly, appears to be incorrect.

2.2.9 Reviews

In the three years covering late 1998 to late 2001 Franklin and his collaborators published a significant number of papers directly relating to the dynamics of the electronegative discharge [52, 53, 55, 56, 57, 58, 59, 60, 61, 62]. The limited nature of the parameter space addressed in each of these works tended to obscure further the increasingly complex body of literature. However, two, quite similar, papers published in quick succession [54, 63] attempted to remedy this by collecting the findings of these, and previous, works and presenting a unified theory as to the behavior of these discharges. Their principle conclusions are presented below in bullet point form:

- the concept of ambipolar diffusion does not apply to plasmas with more than two charge species.
- the central ion-ion plasma is effective at shielding the electric field, reducing it to small values.
- $n_e = n_{e0} \exp(eV/k_B T_e)$ may be a good approximation, except when $\alpha_0 \gg 1$ (as previously noted in [32]).
- the assumption that $n_n = n_{n0} \exp(eV/k_B T_n)$ is a good approximation only at very low pressures ($L/\lambda_i < 0.1$).
- $\alpha_0 =$ const. is a good approximation for
    1. detachment-dominated plasmas at high pressure ($L/\lambda_i > 100$) having $P, Q \gg 1$.
    2. recombination-dominated[f] plasmas with a high pressure ($L/\lambda_i > 100$) with $\alpha_0 \gg 1$ and $P \to 1$.

[f] In general the approximation that $\alpha(x) = \alpha_0$ in the core is better in detachment dominated discharges [53].

- if $\alpha_0 \gg 1$ the entire plasma consists of an ion-ion plasma with sheath dimensions typically smaller than that of an electron ion plasma.

- there is no physical limit in which it is reasonable to make the following assumptions simultaneously: $T_e \neq T_n$, $n_e = n_{e0}\exp(eV/k_BT_e)$ and $n_n = n_{n0}\exp(eV/k_BT_n)$, and $\alpha = \text{const.}$

- a detachment-dominated plasma will be structured if $P < 1$. This structure will become well defined when $L/\lambda_i > 10$, $P/Q < \alpha_0$ and $Q(1+\alpha_0) > 1$.

- a recombination-dominated plasma requires $P < 1$ and are necessarily structured. However, this structure will become well defined when $\alpha_0 > 1$.

- the above requirement on P in the limit of recombination-dominated dynamics means there is a limiting value, T_{ec}, associated with such discharges (corresponding to $K_{iz}(T_e) = K_{att}(T_e)$). The corresponding temperature characteristics are such that $T_e \sim T_e(pL)$, and does not strongly depend on α_0, n_{e0}/n_g or n_{n0}/n_g (for a fixed chemistry).

- at medium and higher pressures in detachment-dominated discharges

$$P\alpha_0 + P + \alpha_0 = Q\alpha_0(1+\alpha_0) \tag{2.16}$$

and

$$X_c \approx \frac{1}{\alpha_0}\frac{P}{Q} \tag{2.17}$$

are good approximations only when $\alpha_0 > 1$.

- at medium and higher pressures in recombination-dominated discharges

$$P\alpha_0 + P + \alpha_0 = J\alpha_0(1+\alpha_0)(1+2\alpha_0) \tag{2.18}$$

and

$$X_c \approx \frac{1}{\alpha_0(\alpha_0+1)}\frac{P}{J} \tag{2.19}$$

are good approximations when $\alpha_0 > 1$.

- the transition from a recombination-dominated discharge to a detachment-dominated discharge is a smooth one and differences between the two limits are not great.

In addition to the above conclusions, there is some discussion given as to the nature and structure of the space charge region which may develop between the ion-ion core and the electron-ion edge [58, 63]. We will return to this subject in section 2.3.

Around the same time, the group in Berkeley also identified a need to bring together their work in a unified and accessible manner [64]. A number of distinct parameter space regimes, within which differing scaling laws apply, are identified. Some effort is made to formally define boundaries separating these parameter space regimes and to identify limitations of their theory. The work of Franklin and his collaborators is only referred to briefly and no comment is offered on their (then) recent criticism.

The control parameters used to segment the parameter space were pl_p and $n_{e0}l_p$[g]. The parameter regimes, and their approximate scaling laws are summarized in table 2.1.

[g]Normalized values for pl_p and $n_{e0}l_p$ were used to formally segment the parameter space. The normalized expressions for pl_p and $n_{e0}l_p$ were $n_g\sigma l_p$ and $K_{rec}n_{e0}l_p/v_{th}$.

When interpreting the works and findings discussed thus far, some subtle phraseological technicalities should be borne in mind:

- Quite often, the term low pressure refers to a regime where pressure is sufficiently low so that the negative ions may be considered to be in thermal equilibrium with the fields, but not so low so as to invalidate the constant- or variable- mobility models.
- high α_0 refers to α_0 being sufficiently high so that useful approximations may be made, but not so high so as to render the assumption of Boltzmann negative ions invalid [64].
- the parameter regime ascribed the label high pressure assumes that the discharge remains approximately non-local, limiting p to $\lesssim \mathcal{O}(1)$ Torr.

2.2.10 Core/Halo Edge As Hydrodynamic Shock

An interesting conceptual insight into the dynamics of electronegative plasma stratification was given by Kaganovich et al. [65, 66]. Assuming a quasi-neutral, three species discharge in which only the electrons must be in equilibrium with the fields, they combined the mass and momentum conservation equations in a similar manner as was done in [67, 68], to form a set of non-linear coupled partial differential equations (one space and one time dimension). It was then showed that the equation for the negative ion density (ignoring volume the source and sink terms) could be recast in the form of a non-linear advection-diffusion equation [65]

$$\frac{\partial n_n}{\partial t} + u_{\text{eff}} \frac{\partial n_n}{\partial x} - \frac{\partial}{\partial x} D_i \frac{\partial n_n}{\partial x} = 0 \tag{2.20}$$

where

$$u_{\text{eff}} = -\frac{n_p \Gamma_e}{(n_n + n_p)^2} \tag{2.21}$$

The importance of equations of this form in the field of hydrodynamics means their properties have been extensively studied, affording a great deal of insight into the behavior of its solution.

Immediately one can see that the effective advection velocity, u_{eff} is a function of n_n (hence the non-linearity), where smaller values of n_n correspond to larger values of u_{eff}. Thus, starting with smooth density profile, at time $t = 0$, ambipolar fields decrease the negative ion density profile close to the wall. This perturbation will propagate back into the plasma with velocity u_{eff}, in a manner similar to the formation of a hydrodynamic shock, as the lower points on the profile attempt to "overtake" the points above.

The natural presence of particle diffusion prevents the profile from becoming singular and ultimately defines a steady state solution where the diffusion flux at the steep shock front balances the inwardly directed advection flux. This happens at some point away from the plasma boundary, and corresponds to a continuous core-halo transition.

2.2.11 Multiple Ions

A major shortcoming of the models and analysis discussed so far is the assumption of only one positive ion and one negative ion. This is a reasonable assumption for oxygen discharges, where typically the negative ion O^- accounts for $> 95\%$ of the total negative ion density [69]. However, this may not be the case in more complex gases such as carbon tetrafluoride (CF_4) and sulphur hexafluoride (SF_6) [70]. This deficiency was addressed by Franklin, in yet another series of publications on electronegative discharge phenomena [70, 71, 72]. A heuristic extension of the Berkeley groups analysis to

discharges containing two positive ion species can be found in [73].

Assuming the discharge is sufficiently collisional, so that one may utilize the mobility-diffusion model for ion transport, Franklin was once again able to derive a set of coupled algebraic equations relating the primary discharge state variables to the discharge chemistry [70]. He then postulated a layered structure where each negative ion has a top hat distribution with discontinuities at differing radial positions [72]. Integrating the source term of the negative ion flux equations over this postulated distribution and utilizing the zero-negative-ion-flux boundary condition allowed him to estimate the position of these transition points. The resulting simultaneous equations are solved numerically, and fail largely to elucidate explicit relations or scaling laws.

2.2.12 The Physical And Mathematical Basis Of Stratification

In an effort to marry the goal of Lichtenberg, Lieberman and their collaborators with the more rigorous approach of Franklin and his confederates, Lampe *et al.* [21] published an ambitiously titled paper; "The physical and mathematical basis of stratification in electronegative plasmas". In this paper they analyzed a similar set of normalized second order differential equations, as those popularized by Franklin. Assuming quasi-neutral mobility limited ion flow, Boltzmann electrons, and cold ions of equal mass and mobility but opposite charge, they considered the non-linear recombination dominated limit only. Utilizing physical arguments, they were then able to transparently demonstrate the mathematical necessity for a transition. Furthermore they were able to obtain an approximate solution to the equations by solving for the core and the edge region separately and

then patching the two solutions at the transition point. The primary findings may be summarized as follows (note, Lampe *et al.* assume a different non-dimensionalization for X, $X = x/(T_e/m_i\nu_i K_{iz} n_g)^{1/2}$)

1. a strongly electronegative core (of variable extent) can be expected to form in any discharge containing cold negative ions, irrespective of the attachment rate or the fraction of attaching gas.

2. the abrupt nature of the core/halo transition has its origin in the non-linearity of the transport equation, not the non-linearity of recombination (and is therefore not a feature unique to the recombination dominated discharge).

3. an approximate solution for the core negative ion profile has the form

$$n_n(x) = \alpha\Big(1 - \frac{1}{2}IX^2\Big) - \Big(\frac{X}{X_c}\Big)^w \tag{2.22}$$

   where $I(P, J)$ and $w(P, J)$ are new non-dimensional parameters. Typically $w \approx \mathcal{O}(10^2) \Rightarrow$ negative ion profile is found to be parabolic until $X/X_c > 1$ when the second term rapidly becomes large and the density falls abruptly.

4. in the edge region, recombination can be neglected but attachment cannot. This gives a finite, but very different negative ion profile in the edge region.

5. the fraction of the discharge occupied by the core, X_c/L, can be shown to be an increasing function of P but is only weakly dependent on J.

6. α_0, on the other hand, depends strongly on J ($\propto J^{1/2}$) but is only weakly dependent on P.

It is interesting to note the derived negative ion profile has the form postulated by Kouznetsov *et al.* [40] and that scaling of α_0 with $J^{-1/2}$ may be interpreted as scaling with $(n_{e0}/n_g)^{-1/2}$ in agreement with [64, 74].

2.3 Transition Structure

It should, by now, be clear that the structured ion profiles observed in plasmas containing a significant density of negative ions emanates from the presence of the additional, significantly heavier (and, as a result, cooler/less-mobile), negatively charged species. These cooler negative charges are strongly confined to the discharge bulk by the self-consistent electric fields formed at the walls.

In this section, we will survey the literature concerning the abrupt transition between the central ion-ion plasma and the outer electron-ion plasma when the positive ions attain the local ion sound speed within the central core.

2.3.1 Two-Temperature Electropositive Plasma Transitions

As with many other electronegative discharge phenomena, some of the earliest relevant works were, in fact, concerned with two-temperature electropositive discharges. Bezzerides *et al.* [75] in Los Alamos National Laboratory, analyised the fluid equations of motion for an expanding plasma with a two-temperature electron population. They found that coupling of space charge effects to the self-consistent separation of the two electron species (owed to their different thermal velocities) led to the formation of a hydrodynamic shock separating a slowly expanding two-temperature plasma and a surrounding single temperature plasma composed of the hotter electrons only. They showed that this shock corresponded to a weak, current-free DL which

accelerated ions into the more rapidly expanding plasma characterized by the hotter electron population.

DL formation manifested itself in their analysis as a multi-valued potential profile when $T_{eh}/T_{ec} > 5 + \sqrt{24}$ and $n_{eh}/n_{ec} < (T_{eh}/T_{ec})^2/2$. Wickens and Allen [76] subsequently noted that the position of this shock corresponded to position at which the ions reach the local ion sound speed, which had become a function of space, due to the differing hot and cold electron profiles. Hairapetian and Stenzel [77] observed these DL's experimentally, and later observed similar, though stationary, DL structures in a confined two-temperature plasma [78].

Sato and Miyawaki [79] analytically examined the characteristics of the potential formed in a confined two-temperature electropositive plasma, assuming kinetic free-fall ion flow. They also found that, when below some critical ratio of T_{eh}/T_{ec}, the presheath structure was similar to that found in single-electron-temperature plasmas, and characterized by the colder electron temperature. As this ratio approaches the critical value of ~ 10.8[h] it was found that the presheath region may be characterized by either T_{eh} or T_{ec}, depending on the ratio of hot- to total- electron density, n_{eh}/n_e. For certain values of n_{eh}/n_e when the temperature ratio is close to the critical ratio, it was found that a simple solution to the potential profile joining the plasma center to the sheath edge did not exist. Instead two pre-sheath regions, each characterized by one of the electron temperatures and separated by a DL, was necessary.

[h]Note that this is the kinetic equivalent to the fluid model transition point defined by $\gamma \geq 5 + \sqrt{24}$ [80]

2.3.2 Extension to Electronegative Plasmas

This work was extended to weakly collisional electronegative plasmas by Kolobov and Economou [81]. Making the assumption that the negative ions simply constitute an additional species in thermal equilibrium, there is little difference between their results and those of Sato and Miyawaki [79]. They found that at very large electronegativities the potential drop across the double layer can be on the order of the electron temperature. These works are closely related, and bear-much resemblance, to that of Braithwaite and Allen [26] with multiple solutions for the edge potential being observed close to the critical values, and an identical critical value for the temperature ratio emerging.

Deutsch and Rauchle [82] attempted a similar study, focusing on the electric field, particle, motion and charge-density distribution in the vicinity a probe immersed in an electronegative plasma. They proposed yet another electronegative ion-transport peculiarity.

By including the most relevant terms in the momentum balance equation for negative ions, they found that, if the density of the negative ions is smaller than some critical value, n_n^*, the momentum transfer from the positive ions to the negative ions by coulomb collisions is larger than the momentum change due to the electrostatic force and the frictional force combined.

Thus, when $n_n < n_n^*$ they proposed that the negative ions move in the same direction as the positive ions. Rather than core-halo stratification, therefore, they propose that at sufficiently low negative ion densities, negative ions may still reach the sheath edge despite the large potential. These negative ions are assumed to enter the sheath edge with a finite velocity but are almost entirely reflected over a small distance.

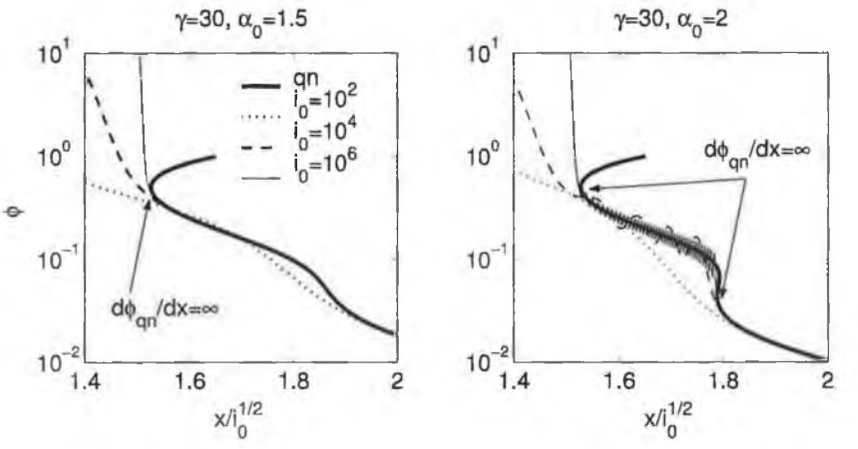

Figure 2.2: *Oscillating double layer structure obtained by Kono [83]. i_0 is the normalized current to the probe ($i_0 \propto 1/\lambda_D^2$). Left: $\alpha_0 = 1.5$, quasi-neutral (qn) approximation breaks down at one point only (conventional sheath edge). Right: $\alpha_0 = 2.0$, quasi-neutral approximation breaks down at two points separated by an extended region. Solving the equations numerically for finite ϵ, they found a non-monotonic potential profile over the region separating the two breakdown points.*

2.3.3 Potential Oscillations

Utilizing the assumption of Boltzmann equilibriums for both negative species, Kono [83] derived an expression for the electric potential profile in a collisionless electronegative discharge adopting the positive ion free-fall model. In keeping with common probe theory convention, he defined the plasma as semi-infinite with $\eta = 0$ at the point $r = \infty$.

Analytical ($\epsilon \equiv \lambda_D/L = 0$, i.e. quasi-neutrality) and numerical ($\epsilon > 0$) solutions for different values of α_0 and γ, are shown in figure 2.2, with the probe/wall placed at $x_D = 0$. As $x_D \to 0$, the assumption of quasi-neutrality must eventually breakdown. This point is generally regarded as corresponding to the sheath edge and is defined by $d\eta/d\xi \to \infty$. However, as found in many previous studies concerning electronegative plasmas, once γ exceeded the critical value of $\geq 5 + \sqrt{24}$, $\eta(x)$ became a multi-valued

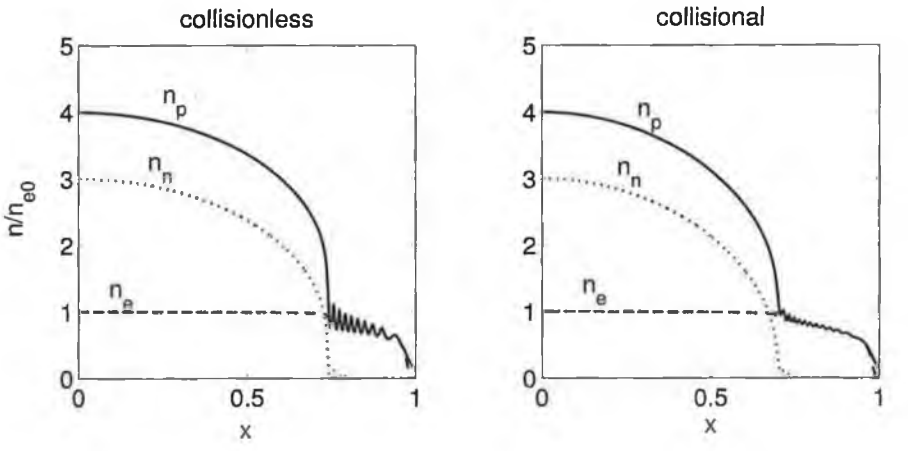

Figure 2.3: *Charge particle profiles recovered by Sheridan et al [84]. Oscillations are shown to persist as we move from the collisoinless regime to a moderately collisional regime.*

function, this time explicitly of position.

Kono argued that a double layer will only form when ϕ becomes multivalued *and* the closest discontinuity to the probe is the high potential discontinuity. η_- therefore jumps discontinuously from a high potential value (characterized by the electron temperature) to a low potential as the location of the discontinuity associated with the low potential location "overtakes" the equivalent high potential point.

The curious "double layer" structures uncovered by Kono are shown in figure 2.2. Kono asserted that these, somewhat unphysical looking oscillations, were not manifestations of an underlying numerical inconsistency, but are valid solutions to the problem as defined. Thus, the obvious question — are they manifestations of an underlying physical inconsistency — incited yet more controversy!

2.3.4 Oscillations: Real or Artifact?

Similar oscillating potential structures were subsequently observed by other authors investigating the potential distribution in electronegative plasmas in both the collisionless [4, 84, 85, 86] and moderately collisional [84, 85] regimes, and were also observed by Schott [87] in his collisionless fluid model of an electropositive plasma containing an additional, mono-energetic, fast electron population. However, such structures were not observed in the kinetic treatments of [52, 80, 85, 88] leading many to conclude that they were, in fact, artifacts associated with the fluid equations applied at low pressure.

Franklin [56] argued that the origin of the potential oscillations observed by Schott was physically inconsistent model assumptions, and so this work may be dismissed. However, this criticism did not extend to the electronegative works cited above. In reference to these works, Franklin agreed with the conclusion of Sheridan *et al.* [4] that these oscillations are the result of quasi-neutrality being violation at a point where the Bohm criterion is not satisfied[i].

At the time it was generally agreed that replacing the fluid ions with kinetic ions, having finite temperature and source term would considerably alter, and likely destroy, these potential (and associated space-charge) oscillations. Thus, it seemed clear that these oscillations had no direct physical significance. Sheridan [80] noted that

> ...the kinetic model is not allowed the luxury of oscillations – it is clear from [equation (1.8)] that the potential must increase monotonically as a function of position ...If this were not the

[i]It would appear as though these authors are implying an analogy between these oscillations, and those observed by Riemann under certain conditions in which the Bohm criterion is violated when ϵ is finite [89].

> case, then the radical[j] in the denominator of the integral would be negative, and a real solution would not exist.

He goes on to note that, in the limit of collisionless ion flow, ions created in the vicinity of an oscillation minima, being born at rest, are trapped there, leading to a singularity in the steady-state density profile. In fluid models however, ions are born with the local ion velocity and so non-monotonic potential profiles are possible.

Kono [74, 90] highlights the 'chicken-and-egg' nature of the first of these arguments noting that, while ion trapping may forbid a non-monotonic profile, plasmas with monotonic profiles necessarily forbid ion trapping! Franklin [58] argued against the second of these points, highlighting the fact that the ion source term in the momentum balance fluid equation could be trivially modified to allow for ions born at rest. The additional term takes the form of a frictional term, and would not necessarily destroy the oscillating structure.

Franklin [58] observed a subtle trend emerging from the existing body of work concerning these oscillations. He noted that the previous works [4, 55, 79, 80, 83, 84, 85, 86, 87] constitute a hierarchy of geometries where positive ion flow at the boundary ranges from strongly converging (e.g. probe tip [83]) to strongly diverging (e.g. cylindrical chamber wall [55]). He concluded that oscillations are strongest for convergent flow and essentially do not exist in diverging flows.

In response to, and in light of [58], Kono [91] attempted to establish definitively the physical significance of these oscillations. Combining the most relevant features from previous kinetic treatments [85, 88] with the insight into the fluid treatment offered by Franklin [58], he constructed a

[j] In mathematics, the term radical is used to refer to the symbol $\sqrt{}$.

kinetic simulation of divergent plasma flow to a cylindrical probe of finite width. This simulation could be qualitatively varied from collisionless to collisional with a specified bulk positive ion temperature. He also modified the fluid treatment to incorporate collisions (as was done previously in [84]) and finite positive ion temperature.

With these two models Kono demonstrated that relaxing the cold positive ion assumption led to a narrowing of the oscillation parameter space, but, even in the limit of $T_p \rightarrow T_e$, this space remained finite. He then compared the output of his collisionless fluid model, in an oscillating parameter regime, with that of the PIC simulation. Somewhat surprisingly, he found excellent agreement between the model and simulation spatial profiles. Introducing weak collisionality into the model was found to alter the PIC profiles dramatically. However, a time-averaged non-monotonic potential profile remained. This demonstrated that such structures could be supported in a kinetic-/collisional- ion discharge.

Examining the temporal behavior of the potential profile observed in the kinetic simulation, revealed a spatio-temporal dynamics which effectively 'pumped' trapped ions out of the time-averaged potential well. This work appears to offer the final word on these oscillations. Though they are readily found in collisionless fluid models, realistic plasma kinetics tend to act to suppress such structures in all but the most specific of imaginable cases [91]. However, that they have some physical basis above that of a numerical/physical artifact appears to be true.

2.4 Summary

Rather than attempt to recapitulate the multitude of conclusions and observations, of which this chapter is itself intended to be a summary, we have

simply chosen to conclude with the following incisive, and broadly applicable, quotation [84]

> For small negative ion concentrations or high collisionality, the discharge is 'stratified', with an electronegative core and an electropositive edge. For the opposite conditions, the discharge is 'uniform' with the negative ion density remaining significant at the edge of the plasma. Between these cases lies the special case of a double-layer-stratified discharge, where quasi-neutrality is violated at the edge of the electronegative core.

ID #	Regime	Assumptions	Scaling
(1)	low pressure mod. high n_{e0} (mod. α_0)	en-ep segregation Boltzmann negative ions $D_{a+}(x), D'_{a+}(x') \approx$ const. $\alpha(x) = \alpha_0\left(1 - \frac{x^2}{l_-^2}\right)$ $n_e(x) = n_{e0}$ $(0 \leq x \leq l_p)$ $u(l_-) < c_s$	$\{a \gg (u(l)/u_{B0})^3\}$ $\alpha_0 \propto (pl_p)^{1/2}(n_{e0}l_p)^{-2/5}$ $l/l_p \propto (n_{e0}l_p)^{-1/5}$ $\Gamma^n_{+w} \propto (pl_p)^{-1/2}$ $\{a \ll (u(l)/u_{B0})\}$ $\alpha_0 \propto (pl_p)^{1/2}(n_{e0}l_p)^{-1/2}$ $l/l_p \sim 1$ $\Gamma^n_{+w} \propto (pl_p)^{-1/2}(n_{e0}l_p)^{-1/2}$
(2)	low pressure mod. low n_{e0} (mod. high α_0)	en-ep segregation Boltzmann negative ions $D_{a+}(x), D'_{a+}(x') \approx$ const. $\alpha(x) = \alpha_0\left(1 - \frac{x^2}{l^2}\right)$ $n_e(x) = n_{e0}$ $(0 \leq x \leq l_p)$ $u(l_-) = c_s$	$\alpha_0 \propto (pl_p)^{1/2}(n_{e0}l_p)^{-1/2}$ $l/l_p \sim 1$ $\Gamma^n_{+w} \propto (pl_p)^{-1/2}(n_{e0}l_p)^{-1/2}$
(3)	high pressure mod. high n_{e0} (mod. high α_0)	en-en segregation $\alpha(x) = \alpha_0$ $\alpha(x') = \alpha_0\left(1 - \frac{(x'+d-l_-)^2}{d^2}\right)$ $n_e(x) = n_{e0}$ $(0 \leq x \leq l_p)$ $u(l_- \simeq l_p) < c_s$	$\alpha_0 \propto (pl_p)^{1/2}(n_{e0}l_p)^{-1/2}$ $l/l_p \propto (pl_p)^{3/4}(n_{e0}l_p)^{-1/4}$ $\Gamma^n_{+w} \propto (pl_p)^{1/4}(n_{e0}l_p)^{-1/4}$
(4) & (6)	high pressure mod. / low n_{e0} (high α_0)	en-en(-ep) segregation $\alpha(x) = \alpha_0$ $\alpha(x') = \alpha_0\left(1 + \frac{(x'+d-l_-)^2}{l^2}\right)$ $u(l_-) = c_s$	Equations become complicated Scaling similar to (3)
(5)	low pressure low n_{e0} (high α_0)	single en region Boltzmann negative ions $\alpha(x) = \alpha_0(1 - x^2/l_p^2)0$ $n_e(x) = n_{e0}$ $(0 \leq x < l_p)$ $u(l_- = l_p) = u_B(\alpha_-)$	Equations become complicated Generally Unimportant

Table 2.1: *Tabulated summary of the of the scaling laws and parameter regimes identified in [64]. a is a nondimensional parameter given by $a = 2\nu_{iz}\lambda/\pi u_{B0}$ (see Appendix C). The parameters x and x' referred to the space within and outside the core. In other contexts it is indicated by the accompanying range. Mod. $\Rightarrow$ moderate/moderately. Note, scaling with low α_0 does not strictly extend to $\alpha_0 < 1$.*

CHAPTER

3 Simulations

The need for computer simulations in the field of plasma physics spawns from the fact that as plasma applications become more advanced the accompanying theory pushes ever further beyond tractable mathematics. Often accurate reproduction of experimentally observed phenomenon requires a model which incorporates a range of physical features including electromagnetics, particle kinetics, fluid mechanics, statistics, chemistry, radiation, ionization and surface physics. Incorporation of even a small number of these phenomena, quickly leads to extremely complex models which are analytically unappealing.

This situation is compounded by the fact that much theoretically important data is often difficult to attain experimentally with any reasonable accuracy/apparatus. As a result computer simulations are often called upon in place of physical experiment, and therefore must often retain a great deal of the known system complexity.

The pros and cons of creating a computer experiment have been summarized by Eastwood in [92] as follows

> Its limitations are that it can handle only a small range of scale lengths, it uses only known physical laws and is subject to numerical errors and finite computer resources ...
> Its strengths are that it aids theory where nonlinearity, many degrees of freedom and lack of symmetry are of importance, and it aids experiment where devices are expensive, data are inaccessible, phenomena are complex and interpretation is ambiguous.

In this work we have used a Particle-in-Cell (PIC) simulation to examine in detail the dynamics of a typical electronegative discharge. We have attempted to construct a benchmark set of reference data over a relatively wide, and industrially significant, parameter space.

3.1 Plasma Abstraction

3.1.1 Kinetic Description

Consider a set of N identical particles each having a position $\boldsymbol{x}_j$ $(= (x_1, x_2, x_3)_j)$ and a velocity $\boldsymbol{v}_j$ $(= (v_1, v_2, v_3)_j)$, $j = 0, 1, \cdots N$. The state of this system at time t_0 is fully prescribed by a single point in $6N$ dimensional phase space, while its evolution in time corresponds to the motion of this point. Thus, if we are to model this system we require a mathematical relation which describes the motion of this point from some initial state. We may formally derive such a relation by considering the exact "microscopic" phase-space density function, $F(\boldsymbol{x}, \boldsymbol{v}, t)$, of the species s. Normalizing this distribution such that its velocity integral is the ordinary (coordinate-space) particle density, gives [93]

$$\int d^3v F_s(\boldsymbol{x}, \boldsymbol{v}, t) \equiv n_s(\boldsymbol{x}, t) \tag{3.1}$$

Simple phase space conservation considerations are used to obtain the equation for the evolution of F_s

$$\frac{\partial F_s}{\partial t} + \boldsymbol{v} \cdot \boldsymbol{\nabla} F_s + \boldsymbol{a}_s \cdot \frac{\partial F_s}{\partial \boldsymbol{v}} = 0 \tag{3.2}$$

where $\boldsymbol{a}_s(\boldsymbol{x}, \boldsymbol{v}, t)$ is the s-species particle acceleration (given by the Lorentz force $\boldsymbol{a}_s = (q_s/m_s)(\boldsymbol{E} + \boldsymbol{v} \times \boldsymbol{B})$ when dealing with charged particles).

Thus, we find that the evolution of the distribution function, which completely describes the plasma state, is determined by a single first-order partial differential equation. However, the apparent simplicity of equation (3.2) is misleading. In practice, the form of the microscopic distribution function (essentially a collection of Dirac delta-functions) is such that it makes numerical solution of this equation an immense task.

The first (of often many) simplification generally introduced to reduce equation (3.2) to a more tractable form is the use of an ensemble-averaged distribution function, $f_s \equiv \langle F \rangle_{\text{ensemble}}$ [93]. This new distribution function, and its associated electric and magnetic fields, are sufficiently smooth so as to allow a reasonable numerical treatment. However, the extraction of an ensemble-averaged equation from (3.2) often requires several assumptions and is not a trivial task. The problem is that the nonlinear acceleration term in (3.2) involves correlations between the individual particle trajectories and the self-consistent fields. This correlation must be considered separatelyby introducing an additional, generally complicated, operator known as the *collision operator*, $C(f)$. Subsequent simplifications and assumptions eventually lead to the ensemble-averaged kinetic equation [93]

$$\frac{\partial f_s}{\partial t} + \boldsymbol{\nabla} \cdot (\boldsymbol{v} f_s) + \frac{\partial}{\partial \boldsymbol{v}} \cdot (\boldsymbol{a}_s f_s) = C_s(f) + I_s \tag{3.3}$$

where the second term on the rhs accounts for particle creation/destruction.

In practice, it is usually equation (3.3), and not (3.2), which is taken as the starting point for mathematical analysis in plasma physics.

3.2 Particle-in-Cell Simulation

For plasma phenomena where collisions are not negligible, and yet the plasma is not near-Maxwellian, a kinetic model is required. These may be regarded as brute force techniques which resort to fully solving the kinetic equation, (3.3), using a minimal number of assumptions. They are extremely computationally expensive when compared to more basic models but have found wide scale application in plasma physics due to their reliability. The typical numerical technique employed in these simulations is the Particle in Cell (PIC) technique, and it is this technique that will be described here.

The PIC technique discretizes the problem by replacing the continuum with a set of sample points (particles), the derivatives with an appropriate numerical method, and the hyperbolic equations with ODE's for particle trajectories. According to [92]

> The PIC method provides an alternative route to achieving the advantages of both Lagrangian and Eulerian methods. To achieve this, they exploit the real characteristics of hyperbolic systems. The hyperbolic terms in the differential equations are treated in a Lagrangian fashion, while the parabolic and elliptic terms are dealt with using Eulerian meshes. To advance the hyperbolic terms, the continuum is replaced by a set of randomly located sample points (particles), each carrying conserved at-

tributes such as mass, position, and charge. Time advancement of the kinetic model PDE's then consists simply of moving the particles.

For illustrative purposes a grossly simplified PIC scheme is portrayed here. More details concerning the specifics of the PIC-MCC simulation used in this work is presented in the next section.

The plasma medium is first deconstructed into a set of N particles. Each simulation particle (or super[a] particle) can be thought of as representing many physical particles. These particles are distributed such that statistically averaged quantities obtained from the distributions correspond to desired macroscopic plasma parameters.

For a point particle at position $\boldsymbol{x}_i$ the potential, ϕ, and electric, $\boldsymbol{E}$, fields are obtained from Poisson's equation [94]

$$\nabla^2\phi = -\frac{1}{\epsilon_0} q\delta(\boldsymbol{x} - \boldsymbol{x}_i) \tag{3.4}$$

$$\boldsymbol{E} = -\boldsymbol{\nabla}\phi \tag{3.5}$$

The force on a particle i due to all other particles in an electrostatic plasma is

$$\boldsymbol{F_i} = q_i \sum_{j, j\neq i} \boldsymbol{E}_{ij} \tag{3.6}$$

from which the new position of particle i can be found using simple Newtonian mechanics

$$m_i \frac{d\boldsymbol{v}_i}{dt} = \boldsymbol{F}_i \tag{3.7}$$

[a] As in superimposed.

$$\frac{d\boldsymbol{x}_i}{dt} = \boldsymbol{v}_i \tag{3.8}$$

If one was to proceed directly with this algorithm, simulating a large number of particles, it would quickly become apparent that such an approach is extremely impractical. Firstly, wrt computational efficiency, each step would require that equation (3.6) be evaluated N times, where the summation in (3.6) would itself contains N terms [94]. That order N^2 operations per step is undesirable is clear once one considers that a typical simulation require a minimum of several thousand particles and tens of thousands of time steps.

In addition, as each particle is a superposition of a large number of physical particles, the forces between simulation particles are much larger then those between real particles and the associated collisional effects are much greater (especially close range collisions, where the force becomes infinite at zero separation in the case of point particles) [94]. In order to reduce these collisional effects the so-called *finite-size-particles* method is used. This method essentially replaces the coulombic force between particles by one which is Coulombic at large distances but goes to zero for short distances, retaining the collective behavior while reducing the collision rate [94].

With the point particles being replaced by finite size particles, the charges become smeared out over a finite region of space, and density variations over regions smaller than the size of a particle cannot be resolved. This implies that in making calculations one may divide the space into cells which are about the size of a particle $\Rightarrow$ the spatial grid. Now to solve Poisson's equation one does not use the exact charge density as indicated above, but instead employs an approximate one obtained by some form of

low-order weighting of the charge densities about the grid points. For finite sized particles, multi-pole expansions converge quite rapidly, and it is rarely necessary to carry it beyond the dipole order [95].

Having charges distributed on a regular grid allows rapid numerical solutions of Poisson's equation. Once this is done a standard 'leap frog' finite difference explicit scheme [b] can be used to advance the particle position and velocity in time:

$$\boldsymbol{v}_i^{n+1/2} = \boldsymbol{v}_i^{n-1/2} + \frac{\boldsymbol{F}_i}{m_i}\Delta t \tag{3.9}$$

$$\boldsymbol{x}_i^{n+1} = x_i^n + v_i^{n+1/2}\Delta t \tag{3.10}$$

with the following minimum step-size restrictions [97]

$$\omega_{pe}\Delta t < 2 \tag{3.11}$$

$$\frac{\Delta x}{\lambda_D} < 2 \tag{3.12}$$

along with the well known CFL (Courant-Fredrichs-Lewy) condition

$$\frac{u\Delta t}{\Delta x} < 1 \tag{3.13}$$

Equation (3.11) and (3.12) are essentially physical restrictions, and simply amount to the requirement that steps size in space and time must be smaller than the smallest space/time length scales associated with the problem (in this case, defined by the Debye length and the inverse of the plasma

[b] The leap-frog algorithm is commonly used for the propagation of waves, where a low numerical damping is required with a relatively high accuracy [96].

frequency, respectively). Equation (3.13) is a generic numerical restriction which states that the simulated medium's velocity must not exceed the characteristic propagation speed of the numerical mesh, $\Delta x/\Delta t$ [98]. In a PIC scheme, this acquires the relatively simple interpretation that particles may not generally traverse a distance greater than one cell length in a single time-step.

Conditions (3.11) and (3.12) may be relaxed by changing from an explicit scheme, as outlined, to an implicit scheme. Such schemes are generally more difficult to implement and computationally more expensive per step, but they may improve overall algorithm performance if a sufficiently large step size differential is achievable. However, one should be cautious when interpreting the results of such schemes. While implicit evaluation may insure numerical stability to very large time steps, there is no guarantee that the stable solution retains the physical integrity of the underlying algorithm [97].

There are several additional physical and numerical issues which must be addressed before a practical PIC simulation may be implemented. However, the essential idea of reducing the problem to near first principles by using Maxwell's equations and Newtonian mechanics to *push* individual particles through phase space, as illustrated above, remains in even the most advanced variants of this technique.

3.3 EN: A 1d3v PIC-MCC Simulation

The PIC simulation used in this work is a 1d3v PIC-MCC electrostatic simulation which has been developed by Prof. Miles Turner. As this code was not developed as part of this project, it will only be discussed briefly here. A comparison between this simulation and several other similar codes

may be found in [99]. A similar simulation is discussed at length in [100].

The simulated discharge is formed between two charge-absorbing floating walls separated by a gap of 5 cm and sustained by a uniform rf current (13.56 MHz) along the direction perpendicular to the simulated dimension. In this way the electrons are heated in a manner similar to that observed in an inductive discharge, with a notable exception. In real inductively coupled discharges, the skin effect confines the heating field to a typically narrow region close to the coil.

The amplitude of the transverse electric field, E_0, is not a valid simulation input. Instead one must specify the amplitude of the transverse electron current density, J_0. The electric field amplitude is then varied in time by the simulation, so as to maintain this current density. In this way one avoids the unphysical instability associated with a constant electric field amplitude[c].

As discussed in the previous section, the PIC simulation technique becomes cumbersome at high densities. Thus, we have restricted ourselves to relatively low plasma densities in our simulations and, as a result, neglected coulomb collisions. This assumption is examined in figure 3.1.

The appended MCC tag denotes that collisions between charged particles and the background gas have been modeled using a *Monte-Carlo collision* technique [95]. It has recently been shown that handling collision chemistry in this way can adversely influence the integrity of the PIC kinetics [101]. However, the parameter regime investigated in this study should not be influenced greatly by these effects.

The background gas composition, density and temperature are modeled as being uniform in space and constant in time. The gas chemistry

[c]Constant transverse electric field amplitude, leads to an unstable positive feedback regime where power absorbed by the electrons is proportional to the electron density [85].

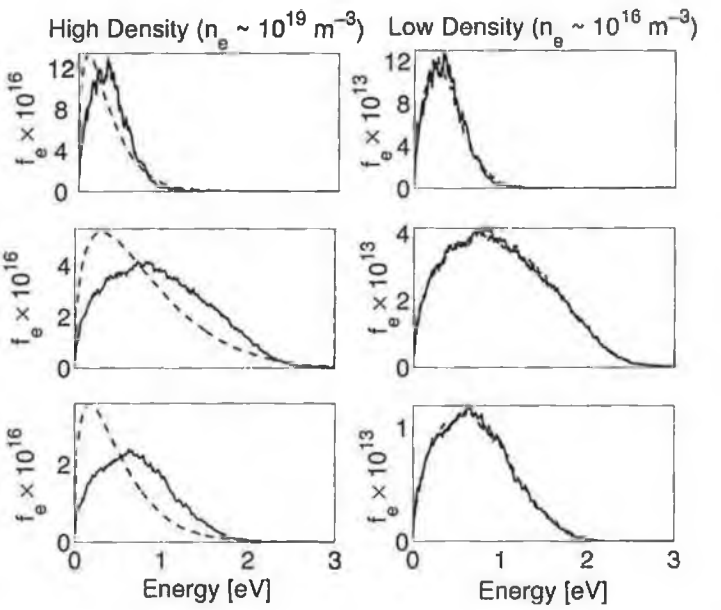

Figure 3.1: *EEDF's calculated using a zero-dimensional kinetic simulation of an argon plasma. Pressure is varied from top to bottom: 1 mT, 10 mT, and 100 mT. We see that at plasma densities below $10^{16}m^{-3}$ the Maxwellianizing effect of electron-electron collisions becomes negligible.*

is therefore independent of the discharge chemistry and conditions. This approximation, which is commonly employed in PIC simulations, is analogous to the physical limit of infinitesimal gas residence time. Additional background particles generated in chemical reactions are simply discarded. Surface reactions have also been neglected, with the exception of self consistent charged particle pair losses.

3.4 Benchmark Simulations

The benchmark study conducted as part of this work, follows the evolution to steady state of four charged species – e, Ar^+, O_2^+, O^- – in an $Ar/O_2(/O_2(a^1\Delta_g))$ background gas using the PIC-MCC simulation discussed in the previous section.

A rich chemistry set containing additional excited, dissociated, and charged species has been used. This chemistry data is summarized in tables 3.1, 3.2 and 3.3. The supplementary species, such as Ar^*, O_3, and O^+, are produced in chemical reactions, forming channels through which simulated species may be created/destroyed, but are subsequently discarded.

This survey covers a particularly large parameter space (electropositive to electronegative, atomic and molecular, approximately collisionless to collisional, recombination-dominated to detachment-dominated). In all, this study consists of just over 50 simulations[d] (figure 3.2).

In real discharges the dominant negative ion loss mechanism may be inextricably linked to the background gas composition, which itself is a function of the discharge parameters. Most notably, oxygen is characteristically recombination-dominated at low pressures and high electron densities, while it becomes detachment-dominated at high pressures. In between these lim-

[d]Including the additional Ar and O_2 simulations, discussed later.

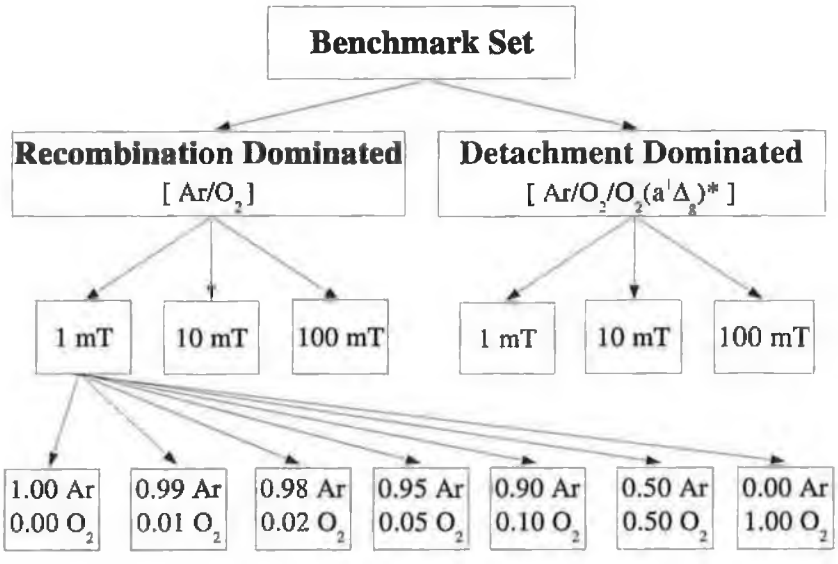

Figure 3.2: *Tree structure illustration of the benchmark simulation set. Neutral pressures of 1 mT, 10 mT, and 100 mT correspond approximately to the collisionless, transitional and collisional regimes, respectively. Gas composition is varied from pure Ar to pure O_2, as shown.*

its, both process are important [62].

In our simulation, the assumption of infinitesimal residence time effectively decouples the gas composition from the discharge parameters and so we are free to impose the dominant negative ion loss mechanism independent of the parameter space in which we chose to operate. As illustrated in figure 3.2, at the highest level we therefore split our simulations into two categories - recombination- and detachment- dominated.

Adding a large amount of $O_2(a^1\Delta_g)$ to the Ar/O_2 background gas, shifts the dominant loss mechanism from ion-ion recombination ($O^- + O_2^+ \rightarrow O + O_2$ and $O^- + Ar^+ \rightarrow O + Ar$) to ion-metastable detachment ($O^- + O_2(a^1\Delta_g) \rightarrow O_3 + e$). The $O_2(a^1\Delta_g)$ density chosen ($n_{O_2(a^1\Delta_g)} = 0.5 n_{O_2}$), is not intended to correspond to any physically significant, or even attainable, value but has simply been chosen to be sufficiently large so as to insure the dominance of detachment over recombination (note, for large Ar concentrations, $Ar^+ + O^-$ recombination remains significant).

Each simulation was run for several thousand rf cycles, so as to achieve a high level of convergence. The associated computational cost in real time ranged from a number of weeks, to a number of months, per simulation. To facilitate this computation a condor distributed computing network, composed of approximately 20 nodes, was utilized.

3.5 Effective/Reduced Chemistry

As stated in the previous section, the chemistry data specified in tables 3.1, 3.2 and 3.3 was used in our simulations. While we make no assertions as to the physical definitiveness or comprehensiveness of this chemistry, we note that it, at the very least, constitutes a closed set. However, the simplified manner in which the simulation models this chemistry renders a significant

portion of these reactions redundant. Collisions involving particles other than the four simulated charge species and the three background gas species make no contribution to the simulations, since the density of these species is invariably zero. As a result, we have effectively simulated the discharge chemistry specified in table 3.4.

While it is important to acknowledge the deceptiveness of the chemical complexity alluded to in tables 3.1, 3.2 and 3.3, explicit identification of this reduced chemistry has an additional benefit. The transparency of this smaller set allows us to define an analytically desirable set of effective reaction rate constants. However, it should be born in mind that this reduced chemistry is only applicable when utilizing the simulation assumption of fixed background gas density. These effective reaction rate constants are listed in table 3.4.

Utilizing table 3.5, the effective simulation continuity equation may be expressed as follows:

$$\nabla \cdot \Gamma_e = K_{iz1} n_e n_g + K_{iz2} n_e n_g - K_{att} n_e n_g - K_{rece} n_e n_{O_2^+} + K_{det} n_{O^-} n_g + K_{dete} n_e n_{O^-} - \frac{A}{V}(h_{l1} n_{Ar^+} u_{B1} + h_{l2} n_{O_2^+} u_{B2}) \tag{3.14}$$

$$\nabla \cdot \Gamma_{Ar^+} = K_{iz1} n_e n_g - K_{rec1} n_{Ar^+} n_{O^-} - \frac{A}{V} h_{l1} n_{Ar^+} u_{B1} \tag{3.15}$$

$$\nabla \cdot \Gamma_{O_2^+} = K_{iz2} n_e n_g - K_{rec2} n_{O_2^+} n_{O^-} - K_{rece} n_e n_{O_2^+} - \frac{A}{V} h_{l2} n_{O_2^+} u_{B2} \tag{3.16}$$

$$\begin{aligned}\nabla \cdot \Gamma_{O^-} = & K_{att} n_e n_g - K_{rec1} n_{Ar^+} n_{O^-} - K_{rec2} n_{O_2^+} n_{O^-} \\ & - K_{det} n_{O^-} n_g - K_{dete} n_e n_{O^-}\end{aligned} \tag{3.17}$$

#	Reaction	$\mathcal{E}_{th}$ (eV)	Rate Coefficient ($m^3\ s^{-1}$)	Ref
1	$e + Ar \rightarrow e + Ar$	0	c	[102]
2	$e + Ar \rightarrow e + Ar^*$	11.6	c	[103]
3	$e + Ar \rightarrow e + Ar^{**}$	13.1	c	[103]
4	$e + Ar \rightarrow e + e + Ar^+$	16	c	[104]
5	$e + Ar^* \rightarrow e + Ar$	-11.6	c	[103]
6	$e + Ar^* \rightarrow Ar^{**} + e$	1.58	c	[105]
7	$e + Ar^* \rightarrow e + e + Ar^+$	4.425	c	[106]
8	$e + Ar^{**} \rightarrow e + Ar$	-13.1	c	[103]
9	$e + Ar^{**} \rightarrow e + Ar^*$	-1.58	c	[105]
10	$e + Ar^{**} \rightarrow e + e + Ar^+$	2.9	c	[107]
11	$Ar^+ + Ar \rightarrow Ar + Ar^+$	0	c	[108]
12	$Ar^+ + Ar \rightarrow Ar + Ar^+$	0	c	[108]
13	$Ar^+ + Ar \rightarrow Ar^* + Ar^+$	23.6	c	[109]
14	$Ar^+ + Ar \rightarrow Ar^+ + Ar^+ + e$	31.6	c	[109]
15	$Ar^* + Ar^* \rightarrow Ar^+ + Ar + e$	-14.4	c	[110]
16	$Ar^* + Ar \rightarrow Ar^* + Ar$	0	c	[110]
17	$Ar^{**} + Ar \rightarrow Ar^{**} + Ar$	0	c	[110]
18	$Ar^{**} + Ar \rightarrow Ar^* + Ar$	0	c	[110]

Table 3.1: *Table of Ar chemical reactions and associated rate constants. Note: Ar^* and Ar^{**} correspond to the excited states $Ar(4s)$ and $Ar(4p)$, respectively. $c \Rightarrow$ tabulated values of $\sigma(\mathcal{E})$ obtained from reference.*

#	Reaction	$\mathcal{E}_{\text{th}}$ (eV)	Rate Coefficient ($m^3\ s^{-1}$)	Ref
1	$e + O_2 \rightarrow e + O_2$	0	c	[110]
2	$e + O_2 \rightarrow O + O^-$	0	c	[110]
3	$e + O_2 \rightarrow e + O_2$	0.02	c	[111]
4	$e + O_2 \rightarrow e + O_2$	0.19	c	[110]
5	$e + O_2 \rightarrow e + O_2$	0.38	c	[110]
6	$e + O_2 \rightarrow e + O_2$	0.57	c	[110]
7	$e + O_2 \rightarrow e + O_2$	0.75	c	[110]
8	$e + O_2 \rightarrow e + O_2(a^1\Delta_g)^*$	0.977	c	[110]
9	$e + O_2(a^1\Delta_g)^* \rightarrow e + e + O_2^+$	11	c	[110]
10	$e + O_2(a^1\Delta_g)^* \rightarrow e + O + O$	6	c	[110]
11	$e + O_2 \rightarrow e + O_2(b^1\Sigma_g^+)^*$	1.627	c	[110]
12	$e + O_2 \rightarrow e + O_2$	0.19	c	[112]
13	$e + O_2 \rightarrow e + O_2$	0.38	c	[112]
14	$e + O_2 \rightarrow e + O + O$	4.5	c	[110]
15	$e + O_2 \rightarrow e + O + O$	6	c	[110]
16	$e + O_2 \rightarrow e + O + O$	8.4	c	[102]
17	$e + O_2 \rightarrow e + O + O$	10	c	[112]
18	$e + O_2 \rightarrow e + e + O_2^+$	12.06	c	[110]
19	$e + O_2 \rightarrow e + O + O(_1S)^*$	14.7	c	[113]
20	$e + O_2^+ \rightarrow O + O$	0	c	[114]
21	$O^- + O_2 \rightarrow O^- + O_2$	0	c	[110]
22	$e + O^- \rightarrow O + e + e$	1.465	c	[115]
23	$O^- + O_2^+ \rightarrow O + O_2$	0	$1.5 \times 10^{-13} \left(\frac{T_g}{300}\right)^{0.5}$	[69]
24	$O + O_2 \rightarrow O + O_2$	0	c	[110]

Continued on next page

Table 3.2 – continued from previous page

#	Reaction	$\mathcal{E}_{\text{th}}$ (eV)	Rate Coefficient (m^3 s^{-1})	Ref
25	$O_2^+ + O_2 \rightarrow O_2^+ + O_2$	0	c	[110]
26	$O^- + O \rightarrow O_2 + e$	0	$0.5 \times 10^{-15} \left(\frac{T_g}{300}\right)^{0.5}$	[111]
27	$O^- + O_2 \rightarrow O_3 + e$	0	$0.5 \times 10^{-20} \left(\frac{T_g}{300}\right)^{0.5}$	[111]
28	$O^- + O_2(a^1\Delta_g)^* \rightarrow O_3 + e$	0	$3 \times 10^{-16} \left(\frac{T_g}{300}\right)^{0.5}$	[111]
29	$O^- + O_3 \rightarrow O_2 + O_2 + e$	0	$0.53 \times 10^{-15} \left(\frac{T_g}{300}\right)^{0.5}$	[111]
30	$O^- + O_3 \rightarrow O_3^- + O$	0	$0.55 \times 10^{-15} \left(\frac{T_g}{300}\right)^{0.5}$	[111]
31	$O^- + O_3 \rightarrow O_2^- + O_2$	0	$10^{-17} \left(\frac{T_g}{300}\right)^{0.5}$	[111]
32	$O^+ + O_2 \rightarrow O_2^+ + O$	0	$2 \times 10^{-17} \left(\frac{T_g}{300}\right)^{0.5}$	[69]
33	$O + O_3 \rightarrow O_2 + O_2$	0	$1.529 \times 10^{-17} \left(\frac{T_g}{300}\right)^{0.5}$	[111]
34	$e + O_3 \rightarrow O_2 + O + e$	0	2.24×10^{-14}	[111]
35	$e + O_3 \rightarrow O^- + O_2$	0	10^{-17}	[111]
36	$O_3^+ + O_2 \rightarrow O_2^+ + O_3$	0	$10^{-17} \left(\frac{T_g}{300}\right)^{0.5}$	[111]
37	$O_4^+ + O_2(a^1\Delta_g)^* \rightarrow O_2^+ + O_2 + O_2$	0	$10^{-16} \left(\frac{T_g}{300}\right)^{0.5}$	[111]
38	$O_4^+ + O_2(b^1\Sigma_g^+)^* \rightarrow O_2^+ + O_2 + O_2$	0	$10^{-16} \left(\frac{T_g}{300}\right)^{0.5}$	[111]
39	$O_4^+ + O \rightarrow O_3 + O_2^+$	0	$3 \times 10^{-16} \left(\frac{T_g}{300}\right)^{0.5}$	[111]
40	$O_4^+ + O \rightarrow O_3^+ + O_2$	0	$3 \times 10^{-16} \left(\frac{T_g}{300}\right)^{0.5}$	[111]
41	$O_4^+ + O_2 \rightarrow O_2^+ + O_2 + O_2$	0	$2 \times 10^{-19} \left(\frac{T_g}{300}\right)^{0.5}$	[111]
42	$O_2(b^1\Sigma_g^+)^* + O_3 \rightarrow O_2(a^1\Delta_g)^* + O_2(a^1\Delta_g)^* + O$	0	$1.8 \times 10^{-17} \left(\frac{T_g}{300}\right)^{0.5}$	[111]
43	$O_2(b^1\Sigma_g^+)^* + O \rightarrow O_2 + O$	0	$0.8 \times 10^{-19} \left(\frac{T_g}{300}\right)^{0.5}$	[111]
44	$O_2(a^1\Delta_g)^* + O \rightarrow O + O_2$	0	$0.7 \times 10^{-21} \left(\frac{T_g}{300}\right)^{0.5}$	[111]

Continued on next page

Table 3.2 – continued from previous page

#	Reaction	$\mathcal{E}_{\text{th}}$ (eV)	Rate Coefficient ($m^3\ s^{-1}$)	Ref
45	$O_2^- + O \rightarrow O^- + O_2$	0	$0.3319 \times 10^{-15} \left(\frac{T_g}{300}\right)^{0.5}$	[111]
46	$O_2^- + O \rightarrow O_3 + e$	0	$1.5 \times 10^{-16} \left(\frac{T_g}{300}\right)^{0.5}$	[111]
47	$O_2^- + O_2(a^1\Delta_g)^* \rightarrow O_2 + O_2 + e$	0	$2 \times 10^{-16} \left(\frac{T_g}{300}\right)^{0.5}$	[111]
48	$O_2^- + O_2(b^1\Sigma_g^+)^* \rightarrow O_2 + O_2 + e$	0	$0.36 \times 10^{-15} \left(\frac{T_g}{300}\right)^{0.5}$	[111]
49	$O_2^- + O_3 \rightarrow O_3^- + O_2$	0	$0.4 \times 10^{-15} \left(\frac{T_g}{300}\right)^{0.5}$	[111]
50	$O_3^- + O \rightarrow O_2^- + O_2$	0	$1.1 \times 10^{-17} \left(\frac{T_g}{300}\right)^{0.5}$	[111]
51	$O_3^- + O \rightarrow O_2 + O_2 + e$	0	$1.5 \times 10^{-16} \left(\frac{T_g}{300}\right)^{0.5}$	[111]
52	$O^- + O^+ \rightarrow O + O$	0	$2.7 \times 10^{-13} \left(\frac{T_g}{300}\right)^{0.5}$	[69]
53	$O_2^- + O_2^+ \rightarrow O_2 + O_2$	0	$2 \times 10^{-13} \left(\frac{T_g}{300}\right)^{0.5}$	[69]
54	$O_3^- + O^+ \rightarrow O_3 + O$	0	$2 \times 10^{-13} \left(\frac{T_g}{300}\right)^{0.5}$	[111]
55	$O_3^- + O_2^+ \rightarrow O_3 + O_2$	0	$2 \times 10^{-13} \left(\frac{T_g}{300}\right)^{0.5}$	[111]
56	$O_3^- + O_2^+ \rightarrow O_3 + O + O$	0	$10^{-13} \left(\frac{T_g}{300}\right)^{0.5}$	[111]
57	$e + O \rightarrow e + O$	0	c	[110]
58	$e + O \rightarrow e + O(_1D)^*$	1.968	c	[110]
59	$e + O(_1D)^* \rightarrow e + O$	-1.968	c	[110]
60	$e + O \rightarrow e + O(_1S)^*$	4.192	c	[110]
61	$e + O(_1S)^* \rightarrow e + O$	-4.192	c	[110]
62	$e + O \rightarrow e + e + O^+$	13.6181	c	[110]
63	$O(_1D)^* + O_2 \rightarrow O + O_2(a^1\Delta_g)^*$	0	$10^{-18} \left(\frac{T_g}{300}\right)^{0.5}$	[111]
64	$O(_1D)^* + O_3 \rightarrow O + O + O_2$	0	$1.2 \times 10^{-16} \left(\frac{T_g}{300}\right)^{0.5}$	[111]
65	$O(_1D)^* + O_3 \rightarrow O_2 + O_2$	0	$2.4 \times 10^{-16} \left(\frac{T_g}{300}\right)^{0.5}$	[111]
66	$O(_1D)^* + O_3 \rightarrow O + O_3$	0	$2.4 \times 10^{-16} \left(\frac{T_g}{300}\right)^{0.5}$	[111]

Continued on next page

Table 3.2 – continued from previous page

#	Reaction	$\mathcal{E}_{\text{th}}$ (eV)	Rate Coefficient ($m^3\ s^{-1}$)	Ref
67	$O(_1S)^* + O_3 \rightarrow O_2 + O + O(_1D)^*$	0	$2.9 \times 10^{-16} \left(\frac{T_g}{300}\right)^{0.5}$	[111]
68	$O(_1S)^* + O_3 \rightarrow O_2 + O_2$	0	$2.9 \times 10^{-16} \left(\frac{T_g}{300}\right)^{0.5}$	[111]
69	$O(_1S)^* + O_2(a^1\Delta_g)^* \rightarrow O + O + O$	0	$0.34 \times 10^{-16} \left(\frac{T_g}{300}\right)^{0.5}$	[111]
70	$O(_1S)^* + O_2(a^1\Delta_g)^* \rightarrow O_2 + O(_1D)^*$	0	$0.36 \times 10^{-16} \left(\frac{T_g}{300}\right)^{0.5}$	[111]
71	$O(_1S)^* + O_2(a^1\Delta_g)^* \rightarrow O + O_2(b^1\Sigma_g^+)^*$	0	$1.3 \times 10^{-16} \left(\frac{T_g}{300}\right)^{0.5}$	[111]

Table 3.2: *Table of O_2 chemical reactions and associated rate constants. $c \Rightarrow$ tabulated values of $\sigma(\mathcal{E})$ obtained from reference.*

#	Reaction	$\mathcal{E}_{th}$ (eV)	Rate Coefficient (m^3 s^{-1})	Ref
1	$Ar^+ + O_2 \rightarrow Ar + O_2^+$	0	$0.51 \times 10^{-16} \left(\frac{T_g}{300}\right)^{0.5}$	[111]
2	$Ar^+ + O \rightarrow Ar + O^+$	0	$0.64 \times 10^{-17} \left(\frac{T_g}{300}\right)^{0.5}$	[111]
3	$Ar^* + O_2 \rightarrow O + O + Ar$	0	$2.1 \times 10^{-16} \left(\frac{T_g}{300}\right)^{0.5}$	[111]
4	$Ar^{**} + O_2 \rightarrow O + O + Ar$	0	$2.1 \times 10^{-16} \left(\frac{T_g}{300}\right)^{0.5}$	[111]
5	$O^- + Ar^+ \rightarrow Ar + O$	0	$3 \times 10^{-13} \left(\frac{T_g}{300}\right)^{0.5}$	[111]
6	$O^- + Ar \rightarrow O^- + Ar$	0	$0.87 \times 10^{-15} \left(\frac{T_g}{300}\right)^{0.5}$	[116]
7	$O_2^+ + Ar \rightarrow O_2^+ + Ar$	0	$0.697 \times 10^{-15} \left(\frac{T_g}{300}\right)^{0.5}$	[116]
8	$Ar^+ + O_2 \rightarrow Ar^+ + O_2$	0	$0.741 \times 10^{-15} \left(\frac{T_g}{300}\right)^{0.5}$	[116]

Table 3.3: *Table of Ar/O_2 chemical reactions and associated rate constants.*

#	Reaction	$\mathcal{E}_{th}$ (eV)	Rate Coefficient ($m^3\ s^{-1}$)	Ref
1	$e + Ar \rightarrow e + Ar$	0	c	[102]
2	$e + Ar \rightarrow e + Ar^*$	11.6	c	[103]
3	$e + Ar \rightarrow e + Ar^{**}$	13.1	c	[103]
4	$e + Ar \rightarrow e + e + Ar^+$	16	c	[104]
5	$Ar^+ + Ar \rightarrow Ar + Ar^+$	0	c	[108]
6	$Ar^+ + Ar \rightarrow Ar + Ar^+$	0	c	[108]
7	$e + O_2 \rightarrow e + O_2$	0	c	[110]
8	$e + O_2 \rightarrow O + O^-$	0	c	[110]
9	$e + O_2 \rightarrow e + O_2$	0.02	c	[111]
10	$e + O_2 \rightarrow e + O_2$	0.19	c	[110]
11	$e + O_2 \rightarrow e + O_2$	0.38	c	[110]
12	$e + O_2 \rightarrow e + O_2$	0.57	c	[110]
13	$e + O_2 \rightarrow e + O_2$	0.75	c	[110]
14	$e + O_2 \rightarrow e + O_2(a^1\Delta_g)^*$	0.977	c	[110]
15	$e + O_2(a^1\Delta_g)^* \rightarrow e + e + O_2^+$	11	c	[110]
16	$e + O_2(a^1\Delta_g)^* \rightarrow e + O + O$	6	c	[110]
17	$e + O_2 \rightarrow e + O_2(b_1\Sigma_g^+)^*$	1.627	c	[110]
18	$e + O_2 \rightarrow e + O_2$	0.19	c	[112]
19	$e + O_2 \rightarrow e + O_2$	0.38	c	[112]
20	$e + O_2 \rightarrow e + O + O$	4.5	c	[110]
21	$e + O_2 \rightarrow e + O + O$	6	c	[110]
22	$e + O_2 \rightarrow e + O + O$	8.4	c	[102]
23	$e + O_2 \rightarrow e + O + O$	10	c	[112]
24	$e + O_2 \rightarrow e + e + O_2^+$	12.06	c	[110]
25	$e + O_2 \rightarrow e + O + O(^1S)^*$	14.7	c	[113]

Continued on next page

Table 3.4 – continued from previous page

#	Reaction	$\mathcal{E}_{th}$ (eV)	Rate Coefficient (m^3 s^{-1})	Ref
26	$e + O_2^+ \rightarrow O + O$	0	c	[114]
27	$O^- + O_2 \rightarrow O^- + O_2$	0	c	[110]
28	$e + O^- \rightarrow O + e + e$	1.465	c	[115]
29	$O^- + O_2^+ \rightarrow O + O_2$	0	$1.5 \times 10^{-13} \left(\frac{T_g}{300}\right)^{0.5}$	[69]
30	$O_2^+ + O_2 \rightarrow O_2^+ + O_2$	0	c	[110]
31	$O^- + O_2 \rightarrow O_3 + e$	0	$0.5 \times 10^{-20} \left(\frac{T_g}{300}\right)^{0.5}$	[111]
32	$O^- + O_2(a^1\Delta_g)^* \rightarrow O_3 + e$	0	$3 \times 10^{-16} \left(\frac{T_g}{300}\right)^{0.5}$	[111]
33	$Ar^+ + O_2 \rightarrow Ar + O_2^+$	0	$0.51 \times 10^{-16} \left(\frac{T_g}{300}\right)^{0.5}$	[111]
34	$O^- + Ar^+ \rightarrow Ar + O$	0	$3 \times 10^{-13} \left(\frac{T_g}{300}\right)^{0.5}$	[111]
35	$O^- + Ar \rightarrow O^- + Ar$	0	$0.87 \times 10^{-15} \left(\frac{T_g}{300}\right)^{0.5}$	[116]
36	$O_2^+ + Ar \rightarrow O_2^+ + Ar$	0	$0.697 \times 10^{-15} \left(\frac{T_g}{300}\right)^{0.5}$	[116]
37	$Ar^+ + O_2 \rightarrow Ar^+ + O_2$	0	$0.741 \times 10^{-15} \left(\frac{T_g}{300}\right)^{0.5}$	[116]

Table 3.4: *Reduced/effective chemistry. Self consistent in the limit of infinitesimal gas residence time.*

Rate Constant	Components
K_{att}	$\vartheta_2 K_8$
K_{iz1}	$\vartheta_1 K_4$
K_{iz2}	$\vartheta_2 K_{24} + \vartheta_3 K_{15}$
K_{rece}	K_{26}
K_{rec1}	K_{34}
K_{rec2}	K_{29}
K_{det}	$\vartheta_2 K_{31} + \vartheta_3 K_{32}$
K_{dete}	K_{28}
K_{eg}	$\vartheta_1(K_1 + K_2 + K_3) + \vartheta_2(K_7 + K_9 + K_{10} + K_{11} + K_{12} + K_{13} + K_{14} + K_{17} + K_{18} + K_{19} + K_{20} + K_{21} + K_{22} + K_{23} + K_{25}) + \vartheta_3 K_{16}$
K_{ng}	$\vartheta_2 K_{27} + \vartheta_1 K_{35}$

Table 3.5: *Effective rate constants constructed from table 3.4. ϑ_1, ϑ_2, and ϑ_3 correspond to the gas fraction of the Ar, O_2, and $O_2(a^1\Delta_g)$, respectively.*

CHAPTER

4

Benchmark Analysis

In this chapter we will disclose the results of our simulations, focusing primarily on characteristics specific to electronegative discharges. Some effort will be made to relate our observations to the literature. Where the literature is deficient, we will attempt to offer some original insight.

4.1 Primary Discharge Parameters

4.1.1 Electronegativity

Possibly the most fundamental property characterizing an electronegative discharges is the central electronegativity, α_0. Figure 4.1 illustrates how this quality varies with gas composition and pressure. Following the approach of Kono [74], we may account for this behavior using a simplified chemistry balance approach, in which negative ions do not reach the walls. In the recombination-dominated limit, this leads to the following simplified balance relation

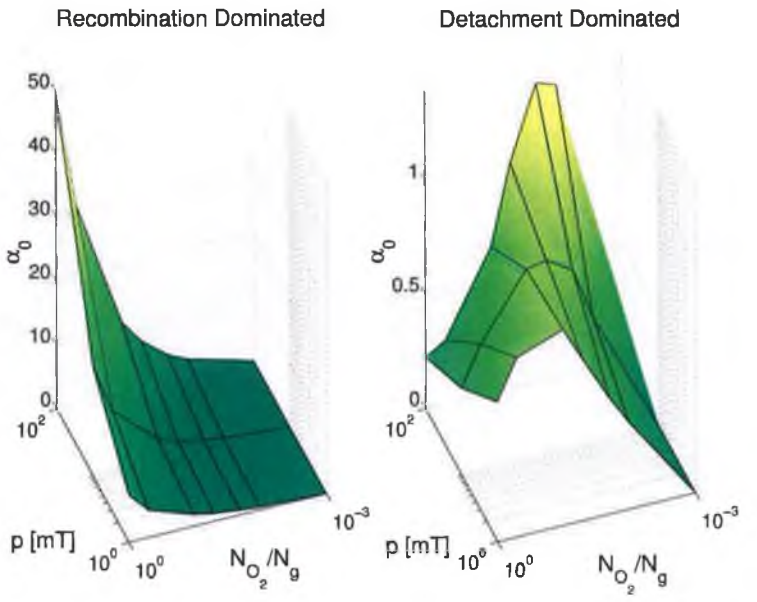

Figure 4.1: *Centre electronegativity extracted from the simulations, shown as a function of gas composition and pressure.*

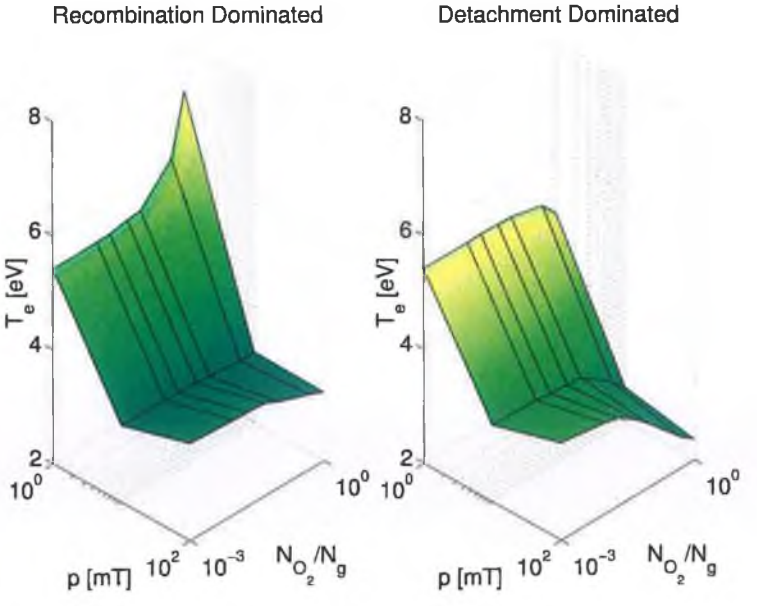

Figure 4.2: *Homogeneous effective electron temperature extracted from the simulations, shown as a function of gas composition and pressure.* **Note:** *axis orientation chosen for optimal viewing and differs from figure 4.1 above.*

$$\vartheta_2 K_{att} n_e n_g \approx \bar{K}_{rec} n_p n_n \tag{4.1}$$

where $\bar{K}_{rec}$ is the density-weighted average recombination rate coefficient, n_p is the net positive ion density, and the O_2 gas fraction is no longer implicit in K_{att} (i.e. K_{att} does not correspond to the definition given in table 3.5). For simplicity we may regard $\bar{K}_{rec}$ as being a constant. Substituting for n_p in this equation by assuming quasi-neutrality and solving for n_n/n_e, we obtain the following expression for α

$$\alpha = \left(\vartheta_2 \frac{K_{att}/K_{rec}}{n_e/n_g} + \frac{1}{4}\right)^{1/2} - \frac{1}{2} \tag{4.2}$$

Thus, assuming K_{att} does not vary considerably over the electron temperature range observed, we find that $\alpha \propto \vartheta^{1/2}(n_g/n_e)^{1/2}$.

It was found that n_e never increases by more than a factor of 2 when pressure was increased by an order of magnitude and always decreases as ϑ_2 is increased. Thus, it is clear why α increases in recombination-dominated simulations as both pressure and O_2 concentration are increased.

For a detachment-dominated plasma, we can write the simple negative ion balance equation as

$$\vartheta_2 K_{att} n_e n_g = \vartheta_3 K_{det} n_g n_n \tag{4.3}$$

Again, assuming quasi neutrality and solving for n_-/n_e we obtain

$$\alpha = \frac{K_{att}/K_{det}}{\vartheta_3/\vartheta_2} \tag{4.4}$$

which, in our detachment-dominated simulations, becomes $\alpha = 2K_{att}/K_{det}$. Therefore α should be independent of pressure and O_2 fraction. Clearly,

this is not the case.

The reasons for this discrepancy are two fold. As there are no longer any parameters which may vary more rapidly, the change in K_{att} with $k_B T_e$ can no longer be ignored. Secondly, as we dilute the initial $O_2/O_2(a^1\Delta_g)$ gas with Ar, n_{Ar^+} increases and $n_{O_2(a^1\Delta_g)}$ decreases. Therefore, the approximation of detachment-dominated chemistry breaks down at large Ar concentration.

One could also argue that neglecting both the ion profile structure and the change in K_{det} with $k_B T_n$ is too crude an approximation — even for qualitative analysis. However, we shall see in the next chapter that this is incorrect.

4.1.2 Electron Temperature

Figure 4.2 shows the electron temperature as a function gas composition and pressure. We see that T_e decreases with increasing pressure in the limit of high oxygen gas fraction. In the opposite limit of high argon gas fraction, we see that T_e decreases initially with pressure, but begins to increase slowly with increasing pressure above 10 mT. In the next chapter, we shall see that this non-intuitive behavior can be attributed to the significant depletion of the EEDF's high energy tail as pressure and argon gas fraction are increased (see Appendix D).

In the recombination-dominated limit, we see that T_e increases as oxygen is added to the background gas. In the detachment-dominated limit, however, the opposite trend is observed. This may be explained utilizing simple particle balance arguments: Although the effective ionization threshold-energy decreases slightly as the oxygen gas fraction increases, the introduction of electron attachment constitutes a significant additional elec-

tron sink. As a result the electron temperature must increase so as to preserve particle balance. In the detachment-dominated limit, however, the large density of easily ionized oxygen metastables ($n_{O_2(a^1\Delta_g)} = \frac{1}{2}n_{O_2}$) reduces the effective ionization threshold-energy considerably and detachment constitutes an additional electron source. Thus, the electron temperature falls with increasing oxygen gas fraction.

4.1.3 Structured Parameter Profiles

A great deal of the theory reviewed in chapter 2 relates to the occurrence of spatial structure in discharges containing a sufficient density of negative ions. Not surprisingly, our kinetic simulations reproduce this structure, as can be seen in figures 4.3 and 4.4.

Recombination-Dominated Profiles

Figure 4.3 shows the density, temperature, velocity and space charge profiles obtained from the O_2 recombination-dominated simulations at 1 mT, 10 mT and 100 mT. We see that, at the lower pressures/electronegativities, the ion densities acquire a parabolic profile. As the electronegativity increases with pressure, these profiles become more flat-topped, as anticipated by the theory. The electron temperature appears to be quite uniform, consistent with non-local electron kinetics over the entire pressure range. The ion temperatures also appear to be relatively uniform in the low-field core region, but are seen to increase sharply at the core-halo transition points. This spatial segregation of both positive and negative ions into a hot edge population and a cooler core population may be easily understood if one considers what, physically, the property termed temperature corresponds to in our simulations.

Due to the prevalence of non-Maxwellian energy distributions in plasma physics, the term 'temperature' (or, more correctly, 'effective temperature') is often used in reference to the mean energy of a specific population of particles, irrespective of the shape of the underlying energy distribution function. This definition becomes somewhat ambiguous when applied to beams of cold particles which, though defined as cold, may clearly possess an arbitrary amount of kinetic energy. Thus, the term is often more specifically understood to refer to the mean energy associated with the random motion of a collection of particles. The anisotropic nature of the self consistent fields generated within a plasma (most notable in a one dimensional abstraction) implies, therefore, that one should not incorporate the energy associated with a populations drift velocity into the term temperature. Our simulation diagnostics do not, however, make this distinction.

With this in mind, it becomes clear why the temperature of the positive ions increases rapidly as they are accelerated across the double layer and toward the discharge walls. The similar spatio-thermal separation of negative ions is the result of a related, though fundamentally different (since the negative ions are not swept out to the walls, or accelerated out of the core), process. Instead, negative ions which are created in the core remain there (until destroyed), while those created in the electropositive edge region are accelerated inwards by the electron confining fields, and therefore appear much hotter. We will return to the topic of the negative ion temperature in section 4.2.4.

A second feature worthy of comment is the behavior of the normalized ion velocity, $u_{O_2^+}/u_{B\alpha}$, where $u_{B\alpha}$ is the local ion sound speed. At all three pressures we see that this velocity increases to a local maximum at a point where quasi-neutrality is locally violated (in contrast with the actual ion

velocity, which increases monotonically). Given the conclusions of section 1.4 and 1.6.2, it is perhaps surprising to find that the value of $u_{O_2^+}/u_{B\alpha}$ does not approach one at this point.

It is likely that this apparent discrepancy reflects the finite value of the plasma parameter, $\epsilon = \lambda_D/L$, in our simulations. Valentini [117], and later Kono [7], examined the ion sound speed away from the quasi-neutral limit of zero finite plasma parameter. Valentini found that the Bohm criterion remained valid but the ion sound speed must be modified according to the relation $u_B = (n_+/n_e)^{1/2}c_s$. Riemann criticized such modification of the Bohm criterion, stating that there is no need and no justification for a modification of the Bohm criterion for finite ϵ [118]. Instead he noted that, for finite values of ϵ, the point at which quasi-neutrality is violated ceases to be well defined and the Bohm criterion loses its significance.

This assertion by Riemann, though correct, is not helpful. Clearly some significance can still be attributed to the normalized ion velocity as defined above, since breakdown consistently occurs in the locality of a maximum in this quantity. However, the correction proposed by Valentini is approximately of order one and does little to account for the discrepancy noted here.

It is perhaps worth noting that one may derive an expression for the electronegative Bohm criterion from kinetic theory. Assuming both negative species are in thermal equilibrium, we find [89, 119]

$$\begin{aligned}\int_0^\infty \frac{1}{mu^2} f(u)du &= -\frac{d}{de\phi}(n_e + n_n) \\ &= n_{sp}\frac{1}{k_B T_e}\left(\frac{1+\alpha_-\gamma}{1+\alpha_-}\right)\end{aligned} \tag{4.5}$$

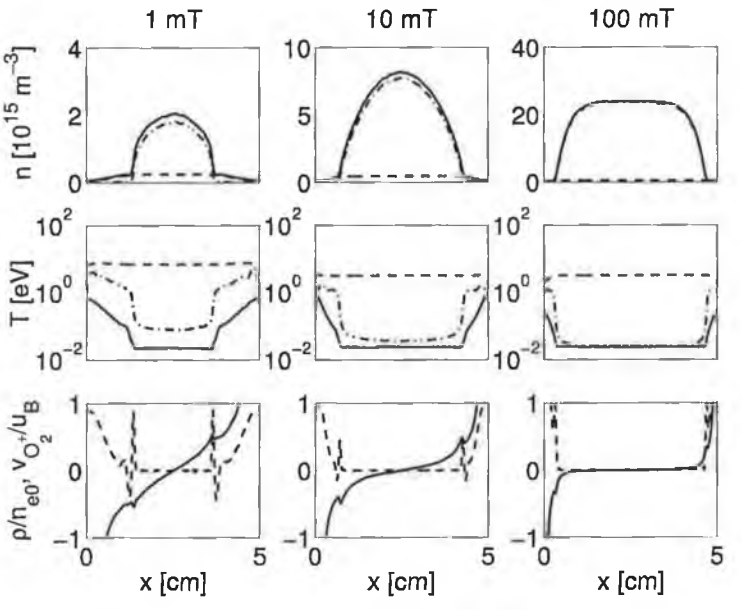

Figure 4.3: *Primary state-variable profiles as a function of pressure extracted from the O_2 recombination-dominated simulations. Top (number density) / Middle (temperature): — O_2^+; $-\cdot-\cdot$ O^-; $---$ e. Bottom (normalized space charge / velocity): $---$ $(5 \times \rho/n_{e0})$; — $v_{O_2^+}/u_B$.*

This may be reduced to equation (1.25) by assuming cold positive ions and replacing the speed distribution function with a $\delta-$function in the integral. However, when α_- and γ are sufficiently large, the velocity at which the above relation is satisfied may be close to the ion thermal speed (as is the case in our simulations), and the assumption of a δ-function replacing $f(u)$ may need revision.

Finally, while collisions are known to encourage sheath formation at ion velocities lower than the Bohm speed [117], one would assume that such effects may be neglected at the lowest values of pl_p examined here.

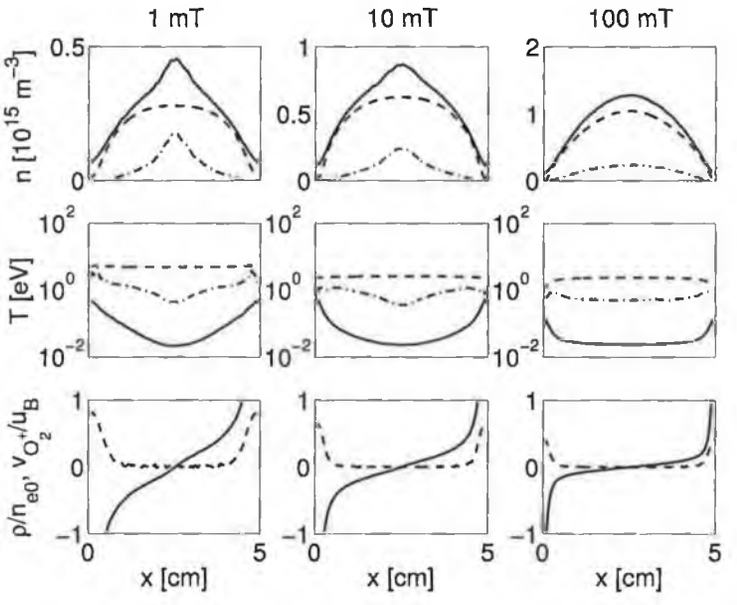

Figure 4.4: *Primary state-variable profiles as a function of pressure extracted from the $O_2/O_2(a^1\Delta_g)$ ($n_{O_2}/n_{O_2(a^1\Delta_g)} = 2$) detachment-dominated simulations. Variable identities given in figure 4.3.*

Detachment-Dominated Profiles

Figure 4.4 shows the equivalent profiles for the detachment dominated simulations ($O_2/O_2(a^1\Delta_g)$). As explained in section 3.4, we have not simply substituted detachment for recombination. Instead, we have introduced a sufficiently large particle density ($n_{O_2(a^1\Delta_g)} = 0.5n_{O_2}$) of the negative ion destroying metastable $O_2(a^1\Delta_g)$, so as to insure ion-metastable detachment-dominates over ion-ion recombination. Therefore, it is not surprising that the negative ion densities have decreased markedly[a].

What is perhaps surprising, however, is the pronounced increase in the

[a]Note that this is not a significant departure from real discharge physics. As ion-ion recombination is proportional to the ion densities (and cannot be prevented), detachment-dominated discharges *must* contain a sufficiently large density of detaching species so as to have electron-gas detachment dominate ion-ion recombination. Therefore, real detachment-dominated discharges necessarily have a relatively large density of detaching species and, as a consequence, a lower electronegativity than a recombination-dominated equivalent.

negative ion temperature and the (related) loss of a distinct core-halo structure. As noted in section 4.1.1, the electronegativity now decreases with increasing pressure and is in all cases less then unity. In the case of the low pressure simulations with higher electronegativities, a partial core-halo structure is still evident, but the large negative ion temperature and absence of an internal point of sonic positive ion flux, means the negative ion profile is considerably more diffusive than that observed in the recombination-dominated discharges.

$Ar/O_2(/O_2(a^1\Delta_g))$ Profiles

Similar profiles obtained from the two-ion simulations are shown in figures 4.5 and 4.6. In these figures the pressure is once again indicated above the profiles while the background gas is now composed of both argon and oxygen, with $n_{Ar}/n_{O_2} = 1$. The trends observed in these discharges are direct extensions of those discussed in the single ion electronegative discharges and most do not warrant further comment.

One noteworthy feature, however, is the behavior of the normalized ion velocity, indicated by the solid (O_2^+) and the dotted (Ar^+) lines in the bottom row of figures 4.5 and 4.6. At 1 mT, we cannot distinguish these lines from one and other. We may account for this observation by considering the ion dynamics in a collisionless discharge. In this limit, the ion velocity is given by equation (1.5). Normalizing this velocity to the local electropositive ion sound speed gives

$$u_i'(x) = \frac{u_i(x)}{u_B(x)} = \sqrt{\frac{2q\phi(x)}{k_B T_e(x)}} \tag{4.6}$$

where $x = 0$ corresponds to the center of the discharge and the potential is defined by $\phi(0) \equiv 0$. As the rhs of 4.6 is independent of i, $u'_{Ar^+}(x) = u'_{O_2^+}(x)$

and both approach 1 simultaneously. Giving the collisionless solution the multiple-ion Bohm criterion, $u'_{is} = 1 \ \forall i$.

At 10 mT and 100 mT, however, the normalized Ar ion velocity begins to exceed the normalized oxygen ion velocity as they approach the edge of the discharge. Assuming negligible negative ion density at the plasma-sheath edge we may write the multiple-ion Bohm criterion, equation (1.51), in terms of normalized velocities, as follows

$$\frac{n_{Ar^+,s}}{u'^2_{Ar^+,s}} + \frac{n_{O_2^+,s}}{u'^2_{O_2^+,s}} = n_{O_2^+,s} + n_{Ar^+,s} \tag{4.7}$$

In this form it is easy to see that the collisionless solution ($u'^2_{Ar^+,s} = u'_{O_2^+,s} = 1$) is a valid one. However, this cannot be a valid solution at finite collisionalities, as we have noted that $u'_{Ar^+}(x)$ and $u'_{O_2^+}(x)$ are no longer equal. Instead, the Bohm criterion must be satisfied at a point where one ion has a super-sonic velocity, and one ion has a sub-sonic velocity.

Substituting the expression for the mobility-limited ion velocity, $u_i \approx \mu_i E$ into equation (4.7) gives

$$u'^2_{Ar^+,s} = \frac{\left[n_{Ar^+,s} + n_{O_2^+,s}\dfrac{m_{Ar^+}}{m_{O_2^+}}\dfrac{\mu^2_{Ar^+}}{\mu^2_{O_2^+}}\right]}{n_{Ar^+,s} + n_{O_2^+,s}} \tag{4.8}$$

$$u'^2_{O_2^+,s} = \frac{\left[n_{Ar^+,s}\dfrac{m_{O_2^+}}{m_{Ar^+}}\dfrac{\mu^2_{O_2^+}}{\mu^2_{Ar^+}} + n_{O_2^+,s}\right]}{n_{Ar^+,s} + n_{O_2^+,s}} \tag{4.9}$$

Thus, the ion with the greater mobility attains the super-sonic velocity at the point where the two ion Bohm criterion is satisfied, while the second ions' velocity must be sub-sonic at this point. This behavior is examined in more detail in Appendix E, where the following electropositive, mobility-

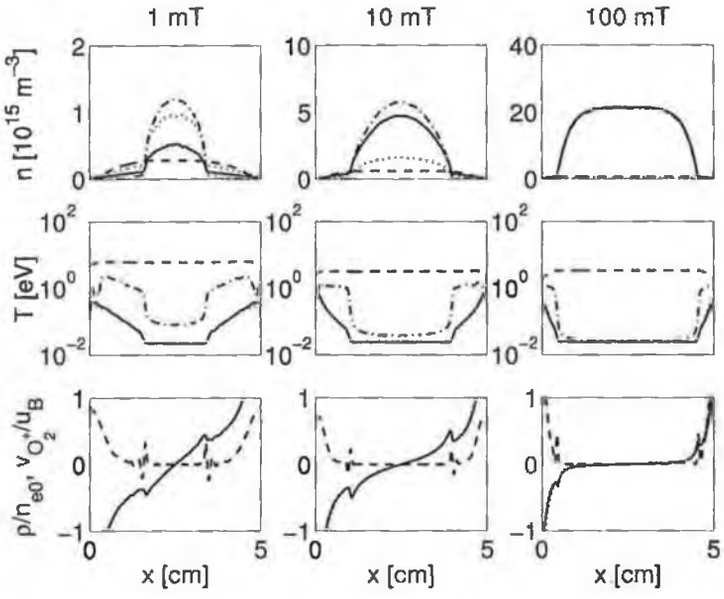

Figure 4.5: *Primary state-variable profiles as a function of pressure extracted from the Ar/O_2 ($n_{Ar}/n_{O_2} = 1$) recombination-dominated simulations. Top (number density) / Middle (temperature): $\cdots$ Ar^+; — O_2^+; $-\cdot-$ O^-; $-\,-\,-$ e. Bottom (normalized space charge / velocity): $-\,-\,-$ $(5 \times \rho/n_{e0})$; — $v_{O_2^+}/u_B$.*

limited, multiple-ion Bohm criterion is derived

$$u_{is}^{\prime 2} = \frac{Z_i n_{is} + \sum_{j,j\neq i}^{N_+} Z_j n_{js} \frac{m_i}{m_j} \frac{\mu_i^2}{\mu_j^2}}{\sum_{j}^{N_+} n_{js}}. \tag{4.10}$$

4.1.4 Double Layers

The recombination-dominated profiles presented in figures 4.3 and 4.5 show that, in the limit of low-pressure / moderate-electronegativity, a narrow internal region in which quasi-neutrality is violated separates the electronegative core from the electropositive halo. This is consistent with the formation of a double layer between the two plasmas, as discussed in detail in chapters

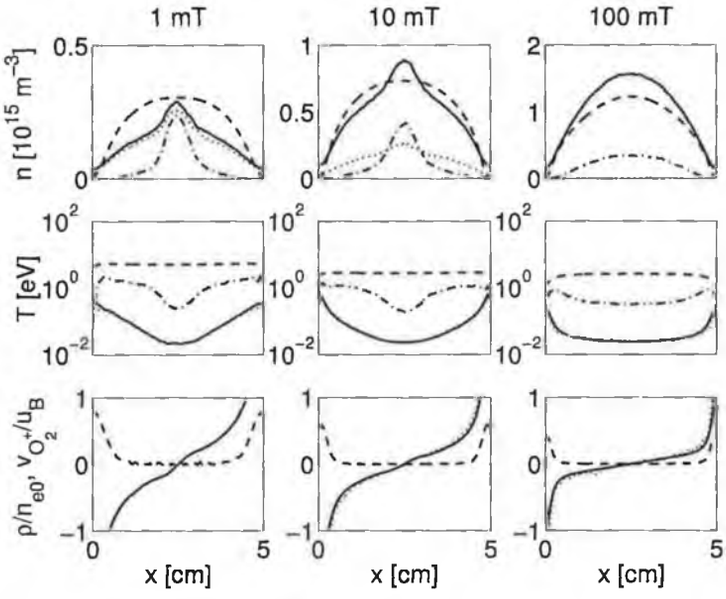

Figure 4.6: *Primary state-variable profiles as a function of pressure extracted from the $Ar/O_2/O_2(a^1\Delta_g)$ ($n_{Ar}/n_{O_2} = 1$; $n_{O_2}/n_{O_2(a^1\Delta_g)} = 2$) detachment-dominated simulations. Variable identities given in figure 4.5.*

1 and 2.

Zooming in on this region (figure 4.7), we see that the potential drop across this space charge layer is on the order of ten times the negative ion temperature, in rough agreement with [88]. We also observe that the region of positive space charge is followed immediately by a region of negative charge, bending the potential back towards zero gradient, as discussed in section 1.6. However, the area under the initial positive space charge portion of the profile exceeds that of the negative portion, resulting in a finite positive space charge at the electropositive edge. In comparison to the core region, the edge plasma is characterized by a higher electrical potential and a larger Debye length. Therefore, it is not surprising that the finite space charge is comparatively large in this region.

In the case of the highest-pressure / highest-electronegativity, no ad-

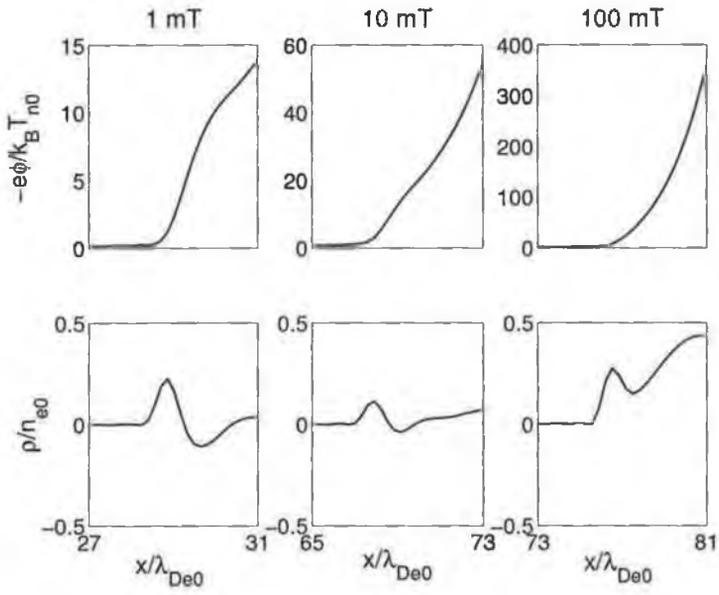

Figure 4.7: *Potential and space charge profiles formed at the core-halo transition of the recombination dominated simulations. Note: potential normalized to the centre negative ion temperature.*

joining region of negative space charge is observed after the initial formation of a region of positive space-charge. Instead the location of the core-edge breakdown corresponds to the conventional sheath-edge, as already noted to occur in discharges of sufficiently high electronegativity.

No indications of space-charge / potential oscillations were evident in our simulations.

4.2 Comparison with Theory

4.2.1 PQJ Analysis

One of the motivating factors behind the explicit reduction of the chemistry specified in tables 3.1, 3.2 and 3.3, to the form given in table 3.4, is that it affords us an opportunity to utilize and test, at least some of the existing

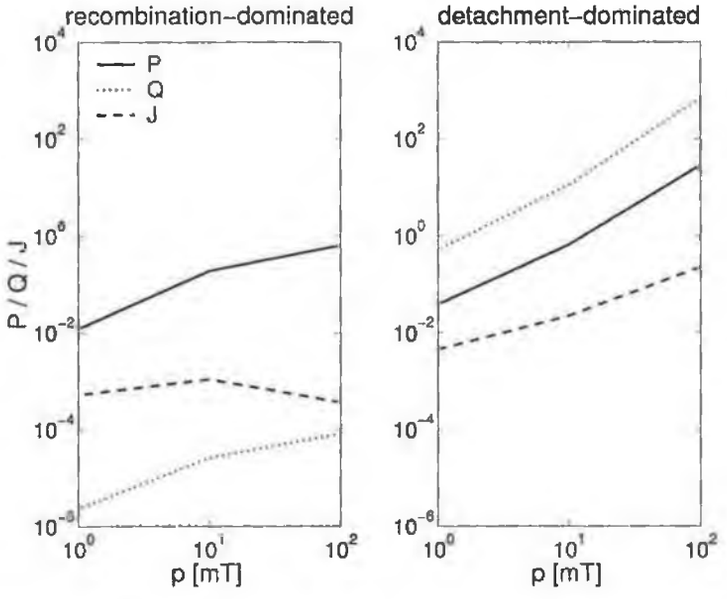

Figure 4.8: *Normalized parameters P, Q, J as a function of gas composition and pressure.*

theoretical treatments.

As an example, we may now define the normalized chemistry parameters P, Q and J, at least in the limit of zero Ar concentration. Figure 4.8 displays the value of these parameters in the case of recombination and detachment-dominated O_2.

We may now use equations (2.16), (2.17), (2.18), and (2.19), to estimate the discharge parameters α_0 and X_c. We concede that these relationships are not intended for low pressure, but in the absence of a collisionless ion free-fall equivalent we evaluate their applicability to our simulation in figure 4.9. In an effort to ascertain the correctness of either expression, the correct value of α_0 was used in equations (2.17) and (2.19) in place of the poor estimates obtained from equations (2.16) and (2.18). A modest, to poor, level of agreement is evident.

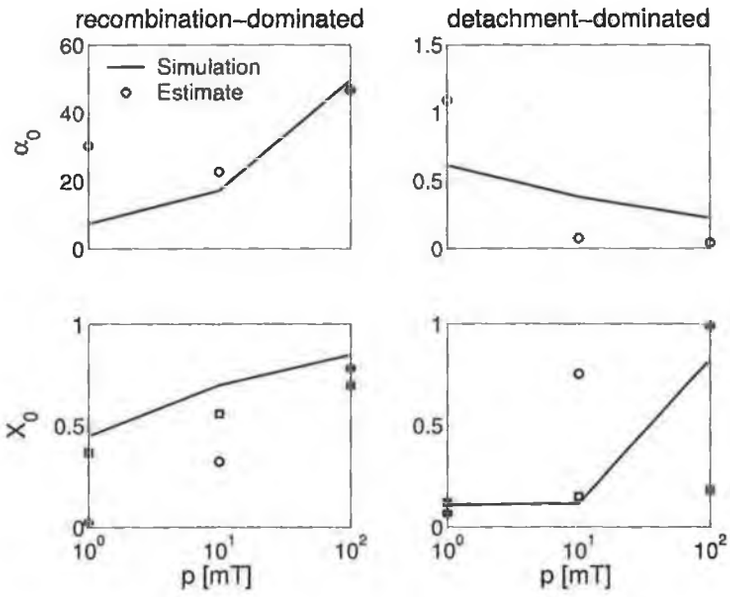

Figure 4.9: *Electronegativity and normalized electronegative core size extracted from the simulations and estimated using equations (2.16), (2.17), (2.18) and (2.19).* — *simulation.* ∘ *calculated;* □ *calculated using* $\alpha_{0,sim}$.

4.2.2 Ion Flux

Assuming a parabolic negative ion profile in the core region, gives [40]

$$\alpha(x) = \alpha_0\left(1 - \frac{x^2}{l^2}\right) \qquad 0 \le x \le l_- \tag{4.11}$$

where l_- is the core half width and l is the scale length of the parameter. Differentiating (4.11) wrt x leads to the following expression for the flux at the core-halo transition

$$\Gamma_{\text{in}} = \frac{2\bar{D}_{a+}\alpha_0 n_{e0} l_-}{l^2} \tag{4.12}$$

where $\bar{D}_{a+}$ is given by equation (2.14), with $\bar{\alpha} = (2/3)\alpha_0$.

If ions do not reach the local sound speed at any point in the core,

but instead decrease gradually to zero, $l \approx l_-$ and equation (4.12) is fully determined. If, on the other hand, ions do attain the local ion sound speed at l_-, l is determined by assuming a discontinuous negative ion profile. α then drops instantaneously from α_- to 0, and continuity of flux gives

$$\frac{2\bar{D}_{a+}\alpha_0 n_{e0} l_-}{l^2} = (\alpha_- + 1) n_{e0} u_B(\alpha_-) \tag{4.13}$$

where $\alpha_- = \alpha(l_-)$.

An assumption implicit in the above formulation is $\gamma = T_g/T_e \simeq \gamma_p \simeq \gamma_n$ (see equation (2.14)). We have seen in section 4.1.3, that this is not a good approximation. Instead, a more general approximation for D_{a+}, which does not make this assumption, was given in [85], and may be expressed as

$$\bar{D}_{a+} \simeq D_{a+} \frac{1 + \gamma_p + (\gamma_p + \gamma_n)\bar{\alpha}}{1 + \gamma_n \bar{\alpha}} \tag{4.14}$$

Figures 4.10 and 4.11 compare the positive ion flux obtained from the simulations with the flux estimated by equation (4.12), where both equation (2.14) and (4.14) are used for comparison. All parameters are extracted from the simulations with the exception of l, which is estimated using equation (4.13).

Examining figure (4.10), it would appear as though the assumption that ions have thermalised to the gas temperature generates better agreement between theory and simulation. This conclusion is compounded by the low pressure simulations in figure (4.11), with significant disparity evident between the two approximated fluxes. This might suggest that the equations used to estimate the ion flux are dependent on the isotropic temperature component only, however this is unlikely. Instead we conclude that, at the very low pressures, the drift diffusion expression breaks down and the

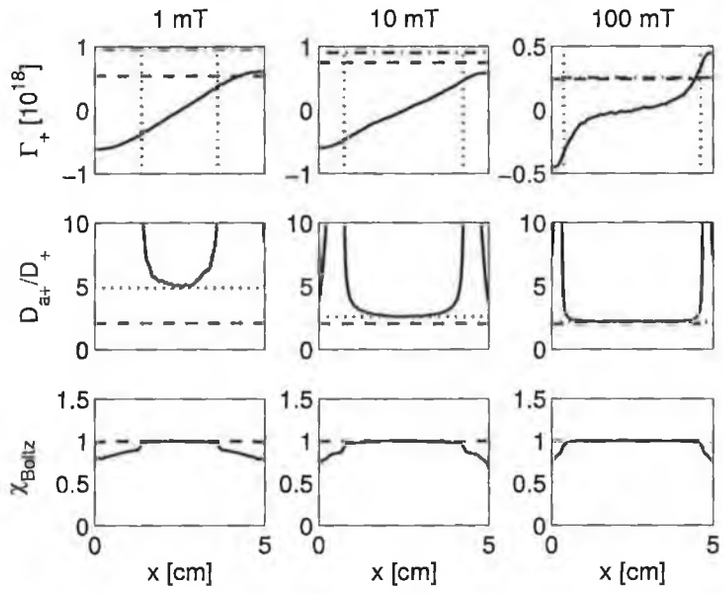

Figure 4.10: *Positive ion flux and the assumption of electronegative ambipolar diffusion. Top (positive ion flux): — simulation; – – – estimated core edge flux using equations (4.12) and (2.14); – · – · estimated core edge flux using equations (4.12) and (4.14). Middle: — $D_{a+}(x)$ given by equation(4.14); – – – equation (2.14) with $\alpha = \alpha_0$; – · – · equation (4.14) with $\alpha = \alpha_0$. Bottom (Boltzmann distribution test): — O^-; – – – e.*

positive ion flux is over estimated. The seemingly more accurate prediction when one assumes $\gamma_n = \gamma_p = \gamma_g$, is therefore a mere consequence of the fact that D_{a+} has been underestimated. The higher pressure simulation in figure (4.11) supports this, though only marginally.

We also examine the behavior of the equation (4.14) over the core region, as well as the assumption of Boltzmann equilibrium. We see that the conclusions $D_{a+} \approx$ const. and $n_n(x) \approx n_{n0} \exp(\eta(x))$ at low pressure appear to be well satisfied. These figures affirm the hypothesis that D_{a+} can be approximated by a constant in the core, even with considerable variation in $\alpha(x)$. However, we note that the value of D_{a+} is sensitive to the approximations used for γ, with the common approximation $\gamma_n \simeq \gamma_p \simeq T_g/T_e$ leading

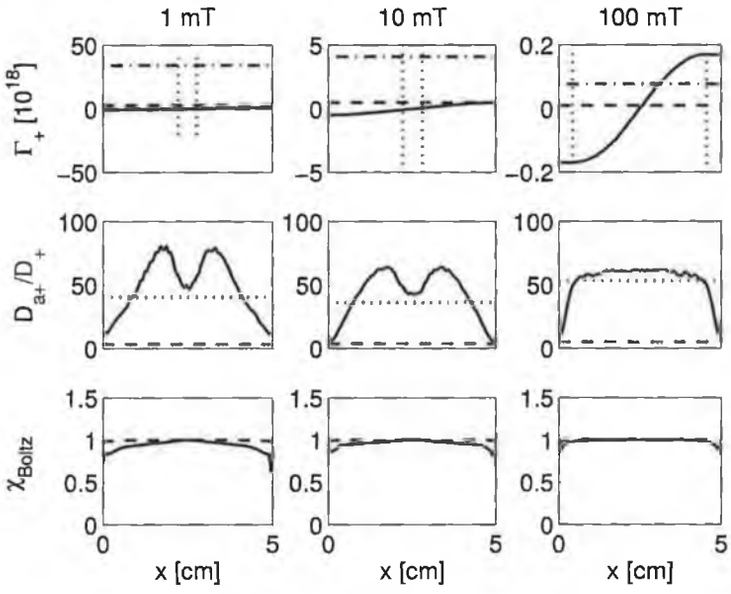

Figure 4.11: *Positive ion flux and the assumption of electronegative ambipolar diffusion. State-variable identification given in figure 4.10*

to a poor estimate of the actual value.

4.2.3 Core Size

Despite the somewhat inconsistent levels of agreement obtained thus far between the low pressure simulations and the principal electronegative theories, one may remain optimistic when estimating the extent of the ion-ion core. This is due to the fact that this property may be derived with only secondary reference to the specifics of the ion dynamics.

Franklin [20] suggests that one may easily estimate the core size using the continuity integrals of [38, 40]. In the original work, these integrals were used as part of a set of simultaneous equations which were solved simultaneously for T_e, α_0, l_- and l. Here, we are simply interested in our ability to estimate the core size, given the primary discharge parameters.

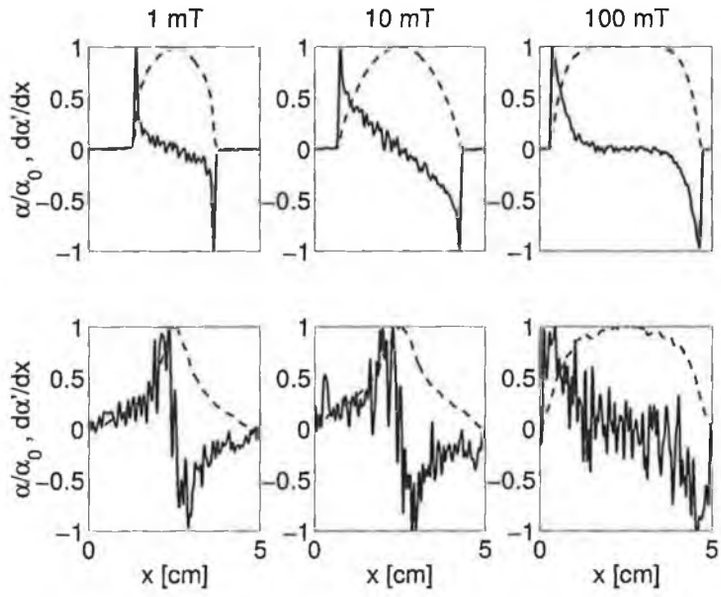

Figure 4.12: *Profiles of $\alpha(x)$ (– – –) and $d\alpha_0/dx$ (—). Note, $d\alpha(x)/dx$ peaks at approximate core edge transition point. This trend was used to extract the values plotted in figure 4.13.*

To do this, we first assume a shape for the ion profile, determined by the parameter space in which we are interested. Using this approximate profile shape, we integrate the negative ion continuity equation from the center of the discharge to the wall, with the boundary conditions of vanishing negative ion flux allowing us to equate the resulting expression to zero. We show in detail how this is done below.

From the reduced chemistry reactions given in table 3.5, one may construct the following expression for the integral of the negative ion continuity equation in one-dimension

$$\int_0^{l_p} \nabla \cdot \Gamma_n \mathrm{d}x = \Gamma_n(l_p) = 0 \tag{4.15}$$

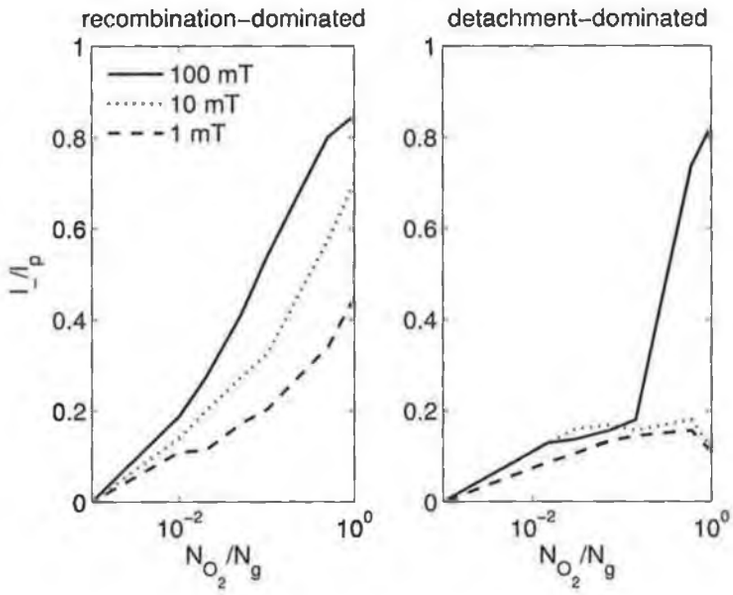

Figure 4.13: *Electronegative core fraction extracted from the simulations as a function of gas composition and pressure.*

$$\Rightarrow \int_0^{l_p} K_{att} n_e n_g \mathrm{d}x = \int_0^{l_-} K_{rec,1} n_{O^-} n_{Ar^+} \mathrm{d}x + \int_0^{l_-} K_{rec,2} n_{O^-} n_{O_2^+} \mathrm{d}x + \int_0^{l_-} K_{del} n_{O^-} n_g \mathrm{d}x + \int_0^{l_-} K_{dete} n_{O^-} n_e \mathrm{d}x = 0 \tag{4.16}$$

Note, the key to this procedure is the fact that integrals containing negative ions must vanish at the location of the core-halo boundary (x = l_-). This allows us to set their upper limit of integration to this, as yet undetermined, value. Assuming $n_e(x)$ to be well approximated by a constant in the core and a parabola in the edge region, and making the additional crude assumption that $n_{Ar^+}/n_{O_2^+} \approx$ const., (4.16) may be rewritten as

$$K_{att}n_{e0}n_g\int_0^{l_-}\alpha\mathrm{d}x+\frac{2}{3}K_{att}n_gn_{e0}(l_p-l_-)=K_{rec,1}n_{e0}^2\zeta_1\int_0^{l_-}\alpha(\alpha+1)\mathrm{d}x$$
$$-K_{rec,2}n_{e0}^2\zeta_2\int_0^{l_-}\alpha(\alpha+1)\mathrm{d}x-K_{det}n_{e0}n_g\int_0^{l_-}\alpha\mathrm{d}x-K_{dete}n_{e0}^2\int_0^{l_-}\alpha\mathrm{d}x \tag{4.17}$$

which may be rearranged, giving the following simplified form

$$\frac{l_-}{l_p}=\frac{2}{3}K_{att}n_g\Big[(K_{rec,1}\zeta_1+K_{rec,2}\zeta_2)n_{e0}\Upsilon_1 + (K_{det}n_g+K_{dete}n_{e0})\Upsilon_2-\frac{1}{3}K_{att}n_g\Big]^{-1} \tag{4.18}$$

where

$$\Upsilon_1=\frac{1}{l_-}\int_0^{l_-}\alpha(\alpha+1)\mathrm{d}x \tag{4.19}$$

$$\Upsilon_2=\frac{1}{l_-}\int_0^{l_-}\alpha\mathrm{d}x \tag{4.20}$$

One may obtain algebraic expressions for Υ_1 and Υ_2 by assuming a profile shape for the $\alpha(x)$ in the core. Some popular approximations are listed.

1. A top-hat profile [20]

$$\Upsilon_1=\alpha_0(\alpha_0+1) \tag{4.21}$$

$$\Upsilon_2=\alpha_0 \tag{4.22}$$

2. A parabolic profile decreasing to zero at the core edge [38]

$$\Upsilon_1 = \left(\frac{8}{15}\alpha_0^2 + \frac{2}{3}\alpha_0\right) \tag{4.23}$$

$$\Upsilon_2 = \frac{2}{3}\alpha_0 \tag{4.24}$$

3. A parabolic profile in which the negative ion density decreases abruptly from some value, α_-, to zero at $x = l_-$ (due to to local violation of the Bohm criterion) [40]

$$\Upsilon_1 = \alpha_0^2\left(1 - \frac{2}{3}\frac{l_-^2}{l^2} + \frac{1}{5}\frac{l_-^4}{l^4}\right) + \alpha_0\left(1 - \frac{1}{3}\frac{l_-^2}{l^2}\right) \tag{4.25}$$

$$\Upsilon_2 = \alpha_0\left(1 - \frac{1}{3}\frac{l_-^2}{l^2}\right) \tag{4.26}$$

When ions do attain the local ion sound speed within the core, we may, once again, use equation (4.13) to estimate l. However, we show in Appendix B that this method is not robust and affords only moderate agreement with our simulations. As we are interested in very low pressures (1-10 mT), we instead estimated l using the low pressure estimate for α_- [1]

$$\alpha_0 \approx \alpha_- \exp\left[\frac{(1+\alpha_-)(\gamma_n - 1)}{2(1+\gamma_n\alpha_-)}\right] \tag{4.27}$$

which has been be derived by combining the electronegative Bohm criterion and the Boltzmann relation for negative ions. The scale length l may then be obtained from (4.11), with $x = l_-$.

Figure 4.14 shows the core-size estimated using conventional assumed $\gamma_n = \gamma = T_e/T_g$. In the recombination dominated limit we have assumed

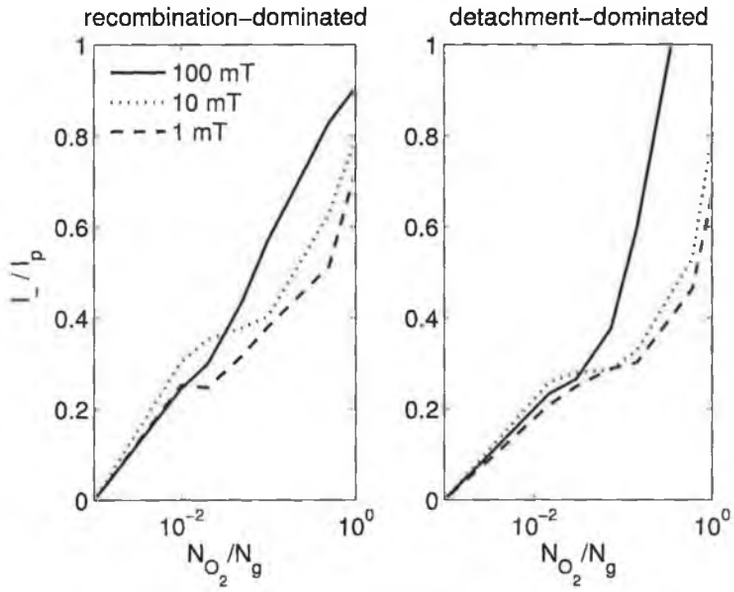

Figure 4.14: *Core size estimated using equations (4.18) with* $\gamma_n = \gamma_p = \gamma_g$. *Recombination-dominated estimated assuming a truncated parabola with the length-scale* l *estimated using (4.27). Detachment-dominated estimated assuming a parabolic profile with* $l = l_-$.

truncated parabolic negative ion profile while, in the detachment-dominated limit, the a single scale-length parabolic profile was assumed.

While we observe a modest level of agreement between this figure and figure 4.13 in the recombination-dominated limit, very poor agreement is uncovered in the detachment-dominated limit. A reasonable conjecture is that this appreciable disparity may be attributed to the fact that the core structure is no longer well defined in this limit (see figure 4.12). However, we see in figure 4.15 that replacing γ with γ_p and γ_n as appropriate, and using the ion temperatures to estimate the reaction rates, leads to a considerable improvement in correspondence between the simulation and the theory.

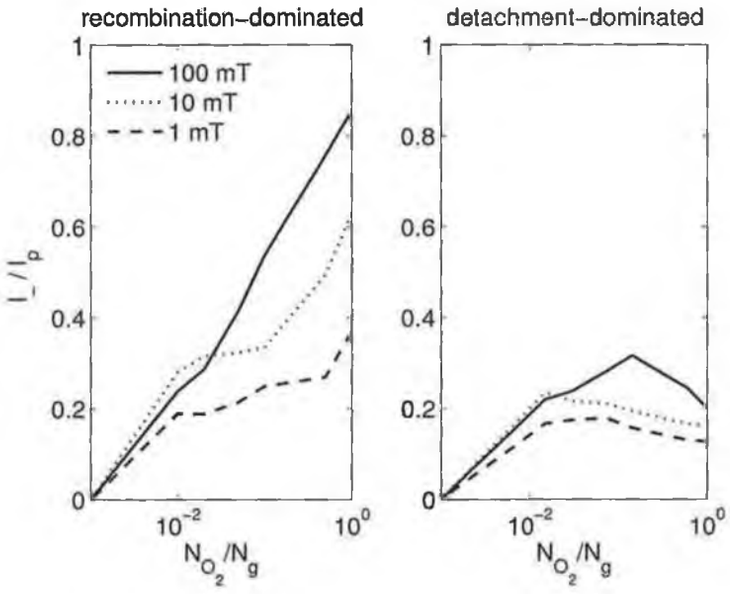

Figure 4.15: *Same as figure 4.14 with* $\gamma_n \neq \gamma_p \neq \gamma_g$.

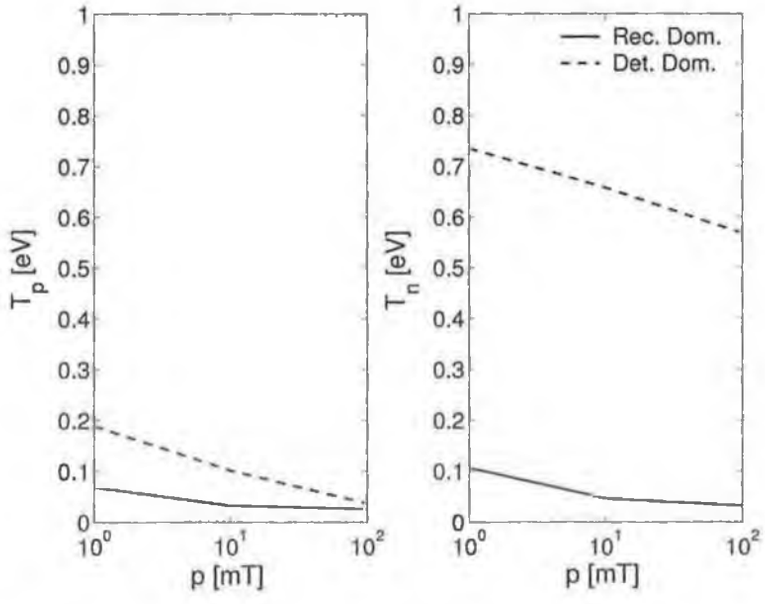

Figure 4.16: *Homogeneous (density weighted) positive (left) and negative (right) ion temperatures as a function gas composition and pressure.*

4.2.4 Ion Temperatures

Keeping in mind the interpretation put forward in section 4.1.3 for the simulation parameter termed temperature, figure 4.16 shows the homogeneous ion temperatures[b] obtained from the O_2 simulations.

As noted previously, the negative ion temperature is considerably larger than that of the positive ions and the background gas, approaching $\mathcal{O}(1)$ eV in the low pressure detachment dominated simulations. The tendency for negative ions to be heated disproportionately has been observed experimentally [120, 121, 122, 123, 124], as well as in in other kinetic simulations [64, 125]. However, no useful model, or appreciation for its significance in typical electronegative discharges, has been developed. One of the most extensive commentary's on the subject is given by Chabert [125] who notes that

> ...the temperature of the hot [negative ions] is a 'kinetic' temperature arising because negative ions are created at different locations in the potential well, rather than a true 'thermodynamic' temperature.

However, some of the unphysical assumptions made in their hybrid-kinetic model renders their findings vague. Using a physically more consistent, fully-kinetic simulation, Kouznetsov [64] also observed negative ion temperatures which were approximately three times the positive ion temperature.

We account for this apparent negative ion heating as follows: The negative ions are created throughout the discharge. Those created in, or near, the sheath regions are accelerated into the plasma by the electron

[b]The term 'homogeneous' is used here to denote the temperature estimated using the mean energy of all such particles in the discharge, regardless of location.

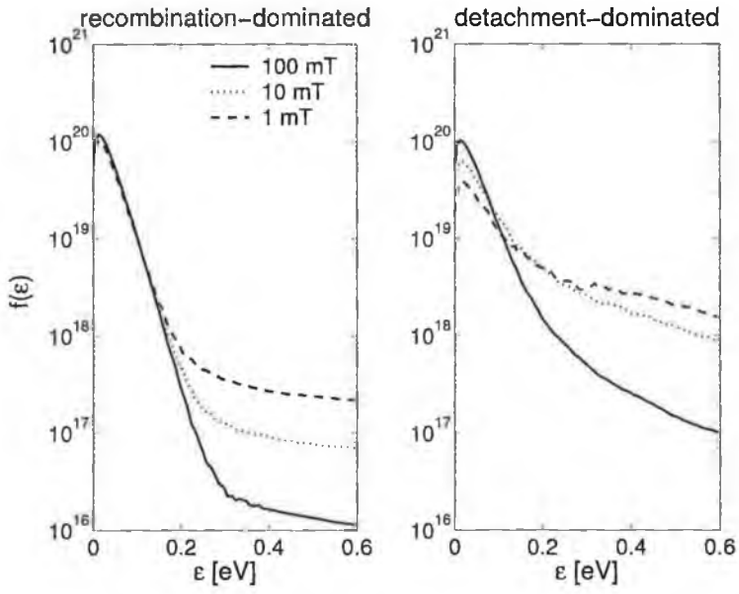

Figure 4.17: *Positive ion energy distribution functions as a function of negative ion destruction mechanism and pressure.*

confining field, gaining a large amount of kinetic energy. Collisions, which scatter a small fraction of this energy into the ions true thermal energy, cool the ions effectively due to the comparable mass of the negative ions and the surrounding heavy particles. A proportion of the negative ions are rapidly heated once formed but equilibrate to the gas temperature soon after. At very low pressures the probability of a negative ion experiencing an elastic collision can be relatively low, and is reduced even further at high energies. Therefore, in a highly destructive environment these ions are often destroyed before being significantly cooled, raising the mean negative ion energy substantially.

Thus, the remarkably high negative ion temperatures generated in our detachment-dominated discharge simulations, can be attributed to reasonably physical arguments.

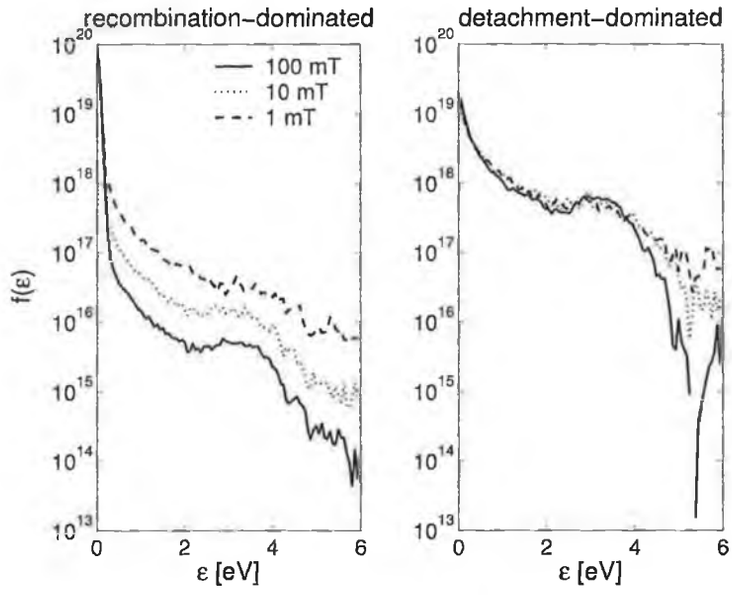

Figure 4.18: *Negative ion energy distribution functions as a function of negative ion destruction mechanism and pressure. Note the 'hump' around 3 eV.*

The homogeneous ion energy distributions are shown in figures 4.18 and 4.17. The positive ion EDF's are essentially Maxwellian, with a high energy tail composed of ions near or in the accelerating space-charge sheath. The negative ion EDF is more interesting with three distinct populations manifested by a two-temperature-type distribution and a high energy 'hump'. The high temperature component of the two-temperature distribution is composed of ions created in medium field regions that have yet to lose their kinetic energy in collisions with the background gas. This population also possibly contains some ions which were originally very hot but have experienced a very small number of collisions. The low temperature component of this distribution, which is by far the most densely populated is composed of ions created in the low-field core region and hot ions which have been cooled by collisions with the background gas. The high energy hump, corresponds

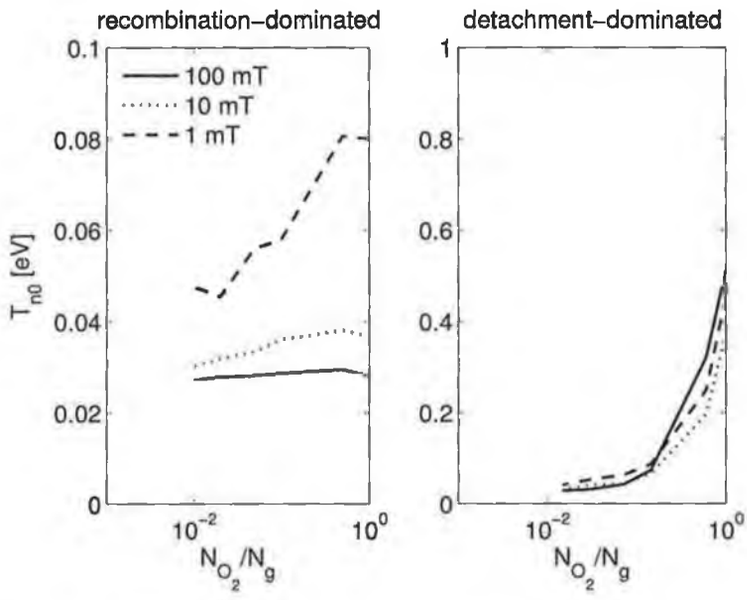

Figure 4.19: *Negative ion temperature as a function of gas composition and pressure.*

to ions born in or near the sheath edge. These ions are born with a very large energy and are less likely to experience an elastic collision before being destroyed by attachment.

Assuming our account of the negative ion 'heating' mechanism is correct, we may construct a crude energy balance equation containing the processes specified above. Ignoring the very obvious departure of the negative ion EDF's from a Maxwellian distribution, a volume averaged energy balance equation may take the following form

$$\begin{aligned}\int_V e\phi(V)K_{att}n_e n_g dV = \frac{3}{2}k_B T_n\Big[\int_V K_{rec,1}n_{O^-}n_{Ar^+}dV \\ + \int_V K_{rec,2}n_{O^-}n_{O_2^+}dV + \int_V K_{det}n_{O^-}n_g dV + \int_V K_{dete}n_e n_n dV\Big] \\ + \frac{3}{2}\delta_n(k_B T_n - k_B T_g)\int_V K_{ng}n_{O^-}n_g dV\end{aligned} \tag{4.28}$$

Making the same assumptions as those in section 4.1.4, we may similarly simplify this expression, yielding

$$\Big[\bar{\mathcal{E}}_c l_- + \frac{2}{3}\bar{\mathcal{E}}_h(l_p - l_-)\Big] K_{att} n_{e0} n_g = \frac{3}{2} k_B T_n \Big[(K_{rec,1}\zeta_1 + K_{rec,2}\zeta_2) n_{e0}^2 \Upsilon_1 l_- + \Big(K_{dete} n_{e0}^2 + K_{det} n_{e0} n_g\Big)\Upsilon_2 l_-\Big] + \frac{3}{2}\delta_n (k_B T_n - k_B T_g) K_{ng} n_{e0} n_g \Upsilon_2 l_- \tag{4.29}$$

where $\bar{\mathcal{E}}_c$ and $\bar{\mathcal{E}}_h$ are the mean energies with which ions in the core and edge regions are created, respectively, and δ_n is the kinetic energy exchange fraction characterizing collisions between the negative ions and the background gas.

Accurately accounting for the potential profile in the edge region is an arduous task. Instead, we crudely assume that ions born outside the core obtain, on average, an amount of energy corresponding to the presheath potential. Negative ions in the core are simply assumed to be created with the thermal energy of the background gas. Thus,

$$\bar{\mathcal{E}}_h \approx \frac{3}{2} k_B T_e/2 \qquad \bar{\mathcal{E}}_c \approx \frac{3}{2} k_B T_g \tag{4.30}$$

For simplicity, we also assume $\delta_n \approx 1$. This gives the following implicit approximation for $k_B T_n$

$$\begin{aligned} &\tfrac{3}{2} k_B T_n \Big[(K_{rec,1}(T_n)\zeta_1 + K_{rec,2}(T_n)\zeta_2) n_{e0}^2 \Upsilon_1 + (K_{det}(T_n) n_{e0} n_g + \\ &\qquad K_{dete}(T_e) n_{e0}^2 + K_{ng}(T_n) n_{e0} n_g)\Upsilon_2\Big] = \\ &\Big[\tfrac{3}{2} k_B T_g + \tfrac{k_B T_e}{2}(l_p/l_- - 1)\Big] K_{att} n_{e0} n_g + \tfrac{3}{2} k_B T_g K_{ng}(T_n) n_{e0} n_g \Upsilon_2 \end{aligned} \tag{4.31}$$

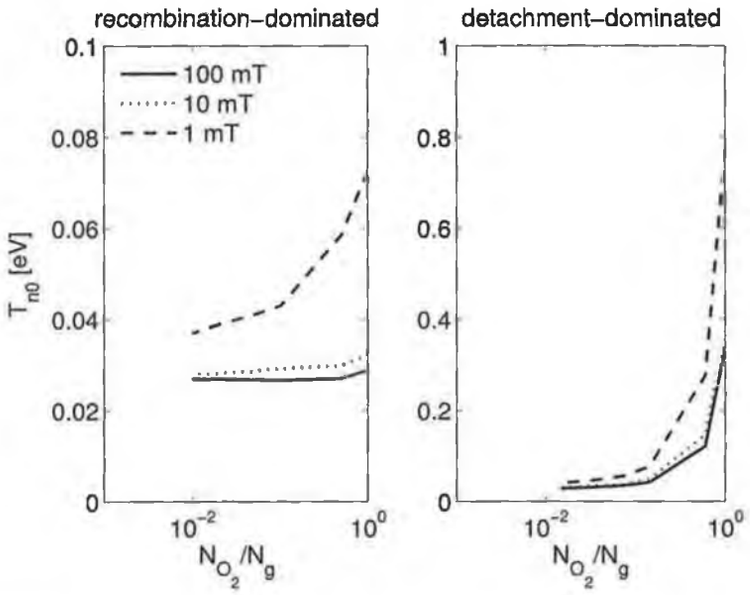

Figure 4.20: *Negative ion temperature calculated using equation (4.31) with the values of l_-/l_p plotted in figure 4.15 used.*

Equation (4.31) may be solved simultaneously with equation (4.18), for given values of α_0, n_{e0}, and k_BT_e, to obtain a volume averaged estimation of k_BT_n. For simplicity, we have used the value for k_BT_n obtained from the simulations to estimate the reaction rates, calculated l_-/l_p (i.e. values plotted in figure 4.15), and subsequently k_BT_n directly. The results of this calculation are shown in figure 4.20.

CHAPTER

5

Global Model

Despite remarkable advances in numerical techniques and computing power over the past 20 years, efficient multi-dimensional modelling/simulation of low temperature plasma discharges has remained a considerable challenge. As a result, global plasma models have found extensive use when modelling discharges with large, convoluted chemistries. These models make many assumptions [1, 126] which, strictly speaking, severely limit the parameter space over which they may be considered valid. However, due to their exceptional computational efficiency, they are routinely applied to model discharges outside this space. Most notable, is the extension of these models to high pressure, multi-component, low-density, and electronegative discharges.

In most cases, model validity is established by comparison with experiment [43, 127, 128, 129, 130]. Model parameters and chemistry are sometimes "*tuned*" until a satisfactory level of agreement is established [131]. Exact correspondence is, of course, never achieved but reasonable qualitative agreement can generally be expected. An obvious problem with this approach is that it is often difficult for one to determine unequivocally the

extent to which discrepancies reflect model limitations. They may (and typically will) also reflect errors and omissions in the chemistry data, as well as experimental error.

In this chapter we will attempt to address this issue. The validity of the most general, and frequently used, global model assumptions will be assessed by comparing a generic global model with our benchmark PIC-MCC simulations. In this way, we shall eliminate discrepancies associated with uncertain chemistry data and minimize experimental error (as the PIC technique uses statistical diagnostics, there remains a finite error component).

It is not our aim to examine the performance of the many discharge-specific / special-case models found in the literature [41, 43, 46, 132]. Instead, a simple, and quite general, model was developed for this work. It may be assumed that more elaborate, case specific (or empirically tuned) models will show greater efficacy.

5.1 The Model

A global model assumes a discharge is fully characterized by its volume (V), surface area (A), mass-flow, absorbed power (P), and gas composition [126]. All spatial derivatives are omitted to facilitate efficient computation. The governing equations are derived from mass and energy conservation arguments, and may be expressed as a set of nonlinear ordinary differential equations. A general particle (mass) balance equation may be expressed as follows:

$$\frac{dn_k}{dt} = \frac{F_k}{V} - \frac{S_p}{V} n_k + \sum_{i=1}^{N_p^k} a_i^k K_i^k \prod_{j=1}^{N_i^k} n_{ij}^k \tag{5.1}$$

where the index k identifies the chemical species, F_k is the mass rate of

flow of species k into the chamber, S_p is the pump speed ($V/S_p = \tau_{res}$), N_p^k is the total number of chemical processes involving species k, a_i^k is an integer specifying the number of k-particles lost/gained per collision in the i^{th} process, K_i^k is the rate constant associated with the i^{th} chemical process, and N_i^k is the number of reactants involved in the i^{th} chemical process.

The first two terms on the rhs of equation (5.1) represent the flow of particles into and out of the chamber, respectively. The last term accounts for particle production and loss within the chamber due to volume and surface chemical processes. It is this term that couples the set of equations to each other.

In addition to the N_k particle balance equations, an energy balance equation for the electrons is also solved. We have assumed that all ion and neutral species are thermalized to the background gas temperature, and that all power transfered to the discharge is absorbed by the more mobile electrons[a]. A general energy balance equation may be expressed as:

$$\begin{aligned}\frac{d}{dt}\left(\frac{3}{2}n_e k_B T_e\right) = \frac{P}{V} - \frac{A_{\text{eff}}}{V}\mathcal{E}_{ei}\sum_{j=1}^{N_B}\Gamma_{B,j} \\ - \sum_{i=1}^{N^e_{\text{p,Vol}}}\left([\mathcal{E}^e_{\text{th},i} - \frac{3}{2}\delta_i^e(k_B T_e - k_B T_g)]a_i^e K_i^e \prod_{j=1}^{N_i^e} n_{ij}^e\right)\end{aligned} \tag{5.2}$$

where A_{eff} is the effective surface area defined by $n_{i,s}A = n_{i,0}A_{\text{eff}}$, N_B is the number of positive ion species, Γ_B is the ion Bohm flux, $N^e_{p,\text{Vol}}$ is the number of volume reactions involving electrons, $\mathcal{E}_{ei}$ is the kinetic energy lost per electron-positive ion pair crossing the sheath, $\mathcal{E}^e_{\text{th},i}$ is the threshold energy for process i, and δ_i^e ($= 2m_e/m_{\text{eff}}$) is the electron energy exchange fraction.

[a]Typically, in our simulations, power absorbed by the electrons $> 0.999P$.

Equation (5.2) has three terms on the right hand side. These correspond to the rate of change of the electron energy density due to power absorption, electron-ion pair loss to the walls, and electron-gas collisions, respectively.

Due to the low electron density and the relatively large pressure range in our simulations, it would be imprudent to make the common assumption of a Maxwellian electron energy distribution function (EEDF). Therefore, we use the expressions derived in [133] to allow for a more general distribution of the form

$$f(\mathcal{E}) = c_1 \mathcal{E}^{1/2} \exp(-c_2 \mathcal{E}^{\mathrm{x}}) \tag{5.3}$$

where $c_1(\mathrm{x})$ and $c_2(\mathrm{x})$ are constants determined by normalization and x is a parameter controlling the shape of the distribution ($\mathrm{x} = 1$ corresponding to a Maxwellian). As in [133], we may write the expressions for c_1 and c_2 in terms of the gamma function, $\Gamma(\xi)$

$$c_1 = \frac{\mathrm{x}}{(\frac{3}{2}k_B T_e)^{3/2}} \frac{\Gamma(\xi_5)^{3/2}}{\Gamma(\xi_3)^{5/2}} \tag{5.4}$$

$$c_2 = \frac{1}{(\frac{3}{2}k_B T_e)^{\mathrm{x}}} \left[\frac{\Gamma(\xi_5)}{\Gamma(\xi_3)}\right]^{\mathrm{x}} \tag{5.5}$$

where

$$\Gamma(\xi) = \int_0^\infty t^{\xi-1} \exp(-t) dt \qquad \xi > 0 \tag{5.6}$$

and we have defined $\xi_p \equiv p/2\mathrm{x}$.

Accurate determination of the sheath edge ion densities is one of the more difficult challenges facing the particle balance scheme. Several methods have been developed to address this issue by formulating a simplified expres-

sion relating the ion density in the center of the discharge to the density at the sheath edge. These models are reviewed in Appendix C. A general form of Godyak and Maksimov's h parameter [44], which aims to approximately capture the transitions from low to high pressure and from electropositive to electronegative regimes[43], is used here:

$$h_{l,i} = \frac{1+3\bar{\alpha}/\gamma}{1+\bar{\alpha}}\left\{\frac{0.86}{[3+L/2\lambda_i+(0.86Lu_{B,i}/2\pi\gamma D_i)^2]^{1/2}}\right\} \tag{5.7}$$

where λ_i and D_i are the ion mean free path and the ion diffusion coefficient, respectively, L is the planar plasma length, $u_{B,i}$ is the ion Bohm speed, and $\bar{\alpha}$ is the volume averaged electronegativity.

The negative ion density is assumed to have been reduced to zero at the sheath edge (consistent with our simulations) and so the simpler electropositive Bohm criterion is used to estimate the ion flux to the walls [133]

$$\frac{1}{2}m_i u_{B,i}^2 = k_B T_e \frac{3\Gamma(\xi_3)^2}{\Gamma(\xi_5)\Gamma(\xi_1)} \tag{5.8}$$

When more than one positive ion is present, we assume that each ion species leaves the discharge with its own Bohm speed. We have not used the mobility-limited multi-ion Bohm criterion derived in Appendix E.

The sheath potential is estimated using the expression derived in [133, 134] (modified for multiple positive ions):

$$\left[m_e\frac{\Gamma(\xi_3)^2}{\Gamma(\xi_1)\Gamma(\xi_4)^2}\right]^{1/2}\frac{4}{n_{es}}\sum_i\frac{h_i n_{i0}}{\sqrt{m_i}} = \int_{eV_s}^{\infty} c_1(\mathrm{x})(\mathcal{E}-eV_s)^{1/2}\exp(-c_2(\mathrm{x})\mathcal{E}^{\mathrm{x}})d\mathcal{E} \tag{5.9}$$

Finally, the energy lost per electron-ion pair crossing the sheath is given by [133]:

$$\mathcal{E}_{ie} = \left[\frac{\Gamma(\xi_3)\Gamma_(\xi_6)}{\Gamma(\xi_5)\Gamma(\xi_4)} + \frac{\Gamma(\xi_3)^2}{\Gamma(\xi_5)\Gamma(\xi_1)}\right]\frac{3}{2}k_B T_e + eV_s \tag{5.10}$$

Using these generic equation templates, user specified chemistry files, and input parameters P and $\mathbf{x}$, the model generates and solves $N_s + 1$ coupled balance equations. The values for P and $\mathbf{x}$ are extracted from the simulations, where P is the mean power absorbed per radio-frequency (*rf*) period, and $\mathbf{x}$ is obtained from the time-averaged homogeneous EEDF using an automated procedure similar to that described in [135].

5.2 Results

5.2.1 *Ar*

Figure 5.1 compares the output of the global model to that of the simulation for a simple electropositive argon discharge over the pressure range 1 mT - 100 mT. Even in this rudimentary case, there is a discernible quantitative difference between the model and the simulation. While reasonable qualitative agreement is recovered by assuming a variable EEDF, the assumption of a Maxwellian EEDF at such low electron densities is shown to be detrimental to model performance. In all cases, the model consistently underestimates the electron temperature and overestimate the electron density. The ion flux to the walls is similarly overestimated at higher pressures, as shown in figure 5.2.

Of course, it is well known that even in low pressure, collisionless discharges the assumption of a Maxwellian EEDF can be a poor one. Non-local electron kinetics can result in preferential heating of high energy electrons, producing a distinct, high temperature, electron population [136]. Figure 5.3 shows the variation in the electron energy probability functions (EEPF's)

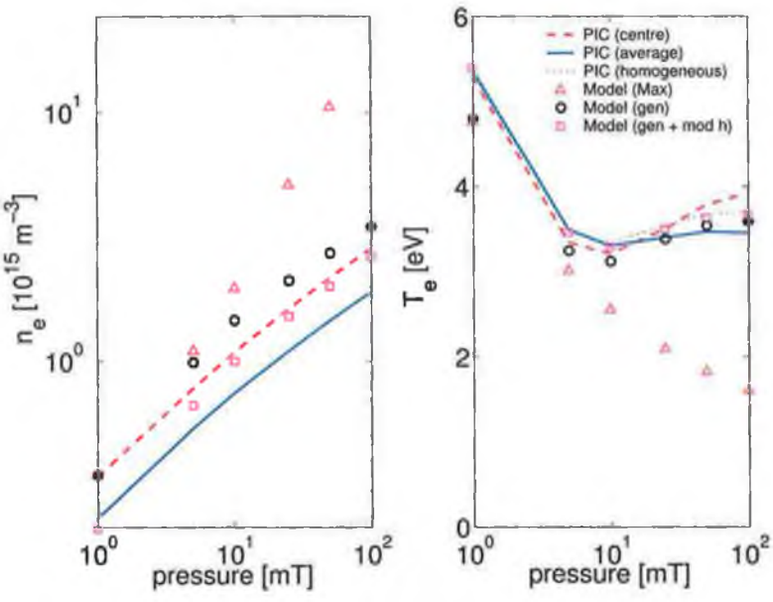

Figure 5.1: *Ar discharge parameters as a function of pressure – model versus simulation. Simulation data: — volume-averaged value; - - centre value; (··· homogeneous EEDF). Model data: △ Maxwellian EEDF; ○ variable EEDF ; □ variable EEDF with modified ion transport parameter, h'.*

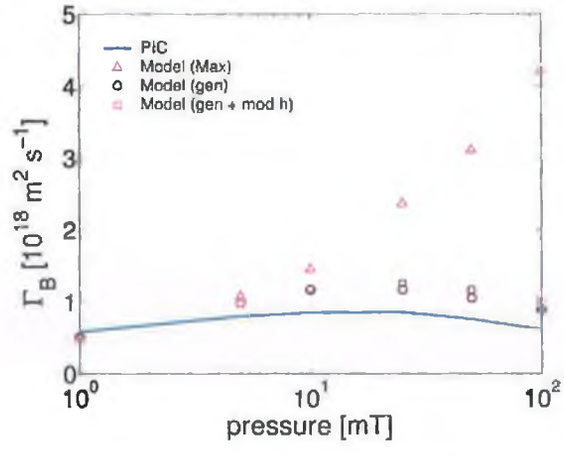

Figure 5.2: *Ar^+ ion wall flux as a function of pressure. Data: — simulation; △ model (Maxwellian EEDF); ○ model (variable EEDF) ; □ model ($h \rightarrow h'$).*

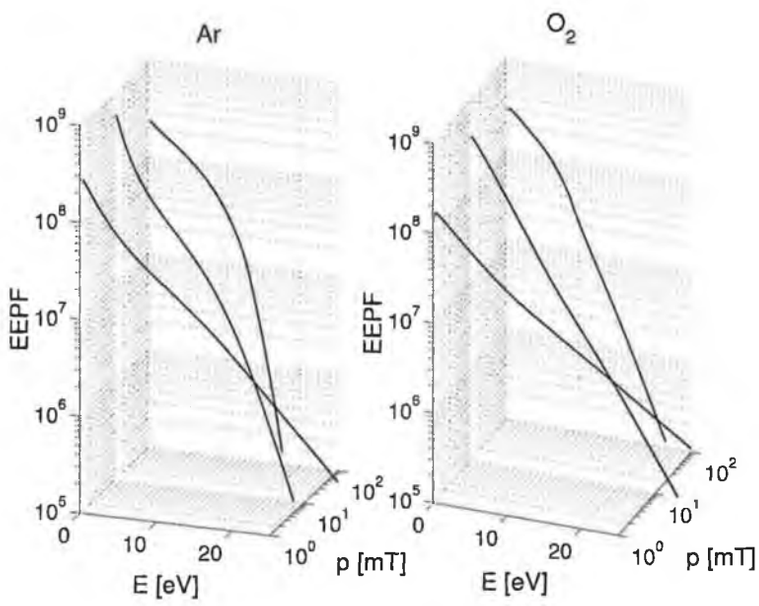

Figure 5.3: *EEPF's obtained from the simulation. Shown as a function of pressure for both the electropositive, atomic Ar discharge (left) and the electronegative, molecular O_2 discharge (left).*

generated by the simulations as pressure is increased. From this figure we see that the EEPF generated by the low pressure Ar simulations is best described by a three-temperature distribution, which is in agreement with experimental observations [137]. This tri-Maxwellian shape is not well modeled by equation (5.3). The smoother EEPF's, associated with the O_2 containing gases, also appear to be poorly modeled by this equation at low pressures. The slightly convex shape seen in this limit, gives values for the parameter x which are less than unity. As these values do not correspond to any reasonable physical limit, all such values are set equal to 1.0. As pressure is increased both distributions assume a more Druyvesteyn-like, single temperature form.

5.2.2 Ar/O_2

Before one can compare the output of a global model with that of a finite dimensional simulation one must, of course, first define a method by which the simulation state variables can be reduced to single valued functions of time. The most obvious means of achieving this is to use either volume averaged or discharge centre values in place of the spatially varying profiles. Unfortunately, in formulating our model, the parameter termed density is used in both of these contexts. It is not clear, therefore, how best to interpret the output. Figure 5.1 indicates that the values for density which have been estimated by the model compare best with those measured in the centre of the discharge. However, as it is reasonable to expect little difference in qualitative behavior between the centre values and volume-averaged values in a single-ion, electropositive discharge, the data in this figure is potentially misleading. Further investigation has shown that the reduced significance of ion loss at the walls as the discharge becomes electronegative favors model comparison with volume-averaged densities (see figure 5.13). Thus, we have exclusively used the volume-averaged values for density in the remainder of this section.

It may be argued that, given the approximate nature of the global model, this distinction is reasonably arbitrary. However, in strongly stratified, electronegative discharges, the difference between the volume averaged density and the centre density can become appreciable. In addition, variation in core size leads to values which differ qualitatively as well as quantitatively.

While, at low pressures, the assumption of uniform charged particle densities is typically a poor one, the assumption of a uniform electron temperature has already been seen in section 4.2.4, to be a much better ap-

proximation[b]. As a result, the volume averaged, and centre values for T_e are quite similar in figure 5.1. However, as we wish to use the temperature which best reflects the overall discharge chemistry, we have not chosen to use either of these values. Instead we have opted to use the electron temperature extracted from the homogeneous EEDF for our comparisons.

As discussed in the preceding chapters, the addition of O_2 to the parent gas adds greatly to the complexity of the charged species dynamics. The discharge becomes structured with an electronegative core region and a surrounding electropositive region. However, as we are not interested in testing the validity of gas-specific/author-specific models, we will temporarily ignore the occurrence of these structures here.

Figure 5.4, compares the electron properties estimated by the global model, assuming a Maxwellian EEDF, with those obtained from the simulations. As expected, both qualitative and quantitative agreement becomes extremely poor as pressure is increased. In contrast, figure 5.5 compares the simulation data with that of the model, where a variable EEDF has now been assumed. Once again, changing to a variable EEDF is shown to improve model-simulation agreement significantly.

This amiable level of qualitative agreement extends to the ion properties, shown in figures 5.6, 5.7, 5.8 and 5.9. Qualitatively all features produced by the simulations are reproduced by the model, despite the occurrence of spatial structure in the limit of high O_2 concentration.

Quantitative agreement appears to be marginally worse in the detachment-dominated electronegative limit. We do not believe this to be a reflection/indication of fundamentally different detachment-dominated dynamics,

[b]Uniform density and uniform temperature profiles are contradictory properties. A flat density profile suggests a spatially varying temperature profile [138], which would be detrimental to any zero dimensional chemistry model.

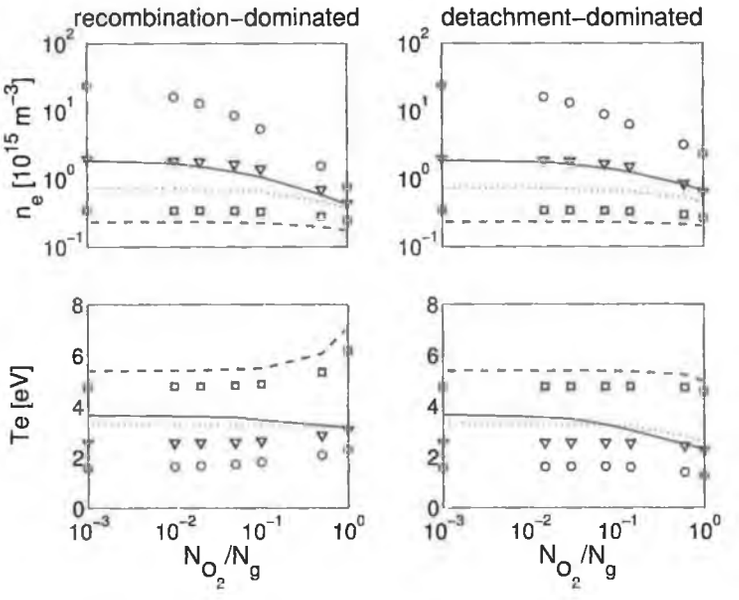

Figure 5.4: *Electron parameters as a function of gas composition and pressure. Model assumes a Maxwellian EEDF. Simulation: — 100 mT; ··· 10 mT; –– 1 mT. Model: ○ 100 mT; △ 10 mT; □ 1 mT.*

but rather an artifact of the considerably elevated negative ion temperature.

Figure 5.10 appears to suggest that the, thus far, creditable level of model efficacy extends to the ion Bohm flux, which one would expect to be a strong function of both the shape of the EEDF and the ion transport parameter, h. However, figure 5.11 contravenes this. In the limit of high O_2 density, qualitative differences between the model and the simulation emerge in the recombination-dominated regime. This qualitative discrepancy most likely reflects the limitations of the ion transport model, which does not account for discharge structure or, indeed, the non-Maxwellian nature of the EEDF. In the detachment-dominated limit, however, the high negative ion temperature, and low negative ion density, suppress the formation of well defined ion-profile structures. Therefore, the qualitative agreement in this limit appears to be significantly improved.

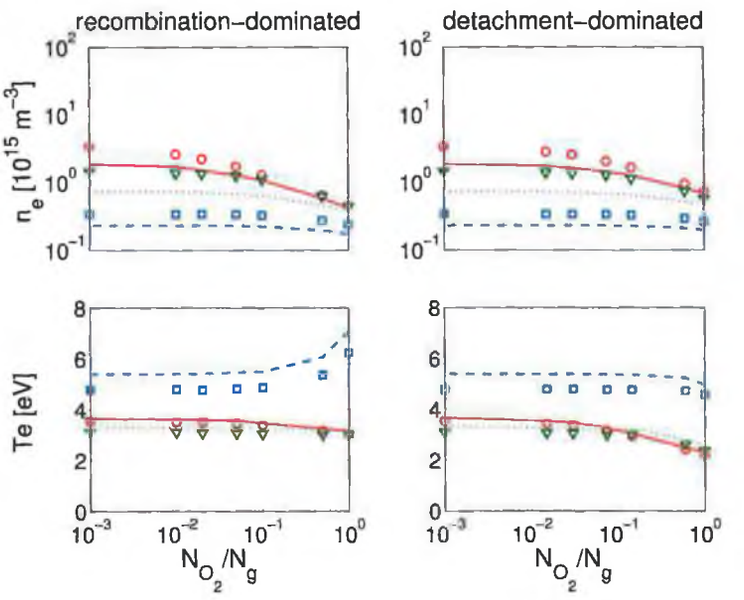

Figure 5.5: *Electron parameters as a function of gas composition and pressure. Model assumes a variable a EEDF having the form of equation (5.3). Symbols/lines retain the identities listed under figure 5.4.*

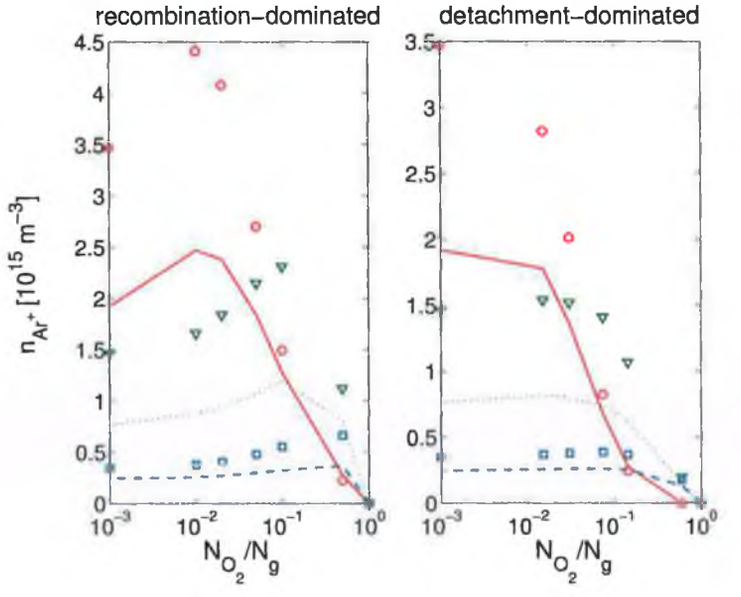

Figure 5.6: *Ar^+ ion densities as a function of gas composition and pressure. Symbols/lines retain the identities listed under figure 5.4.*

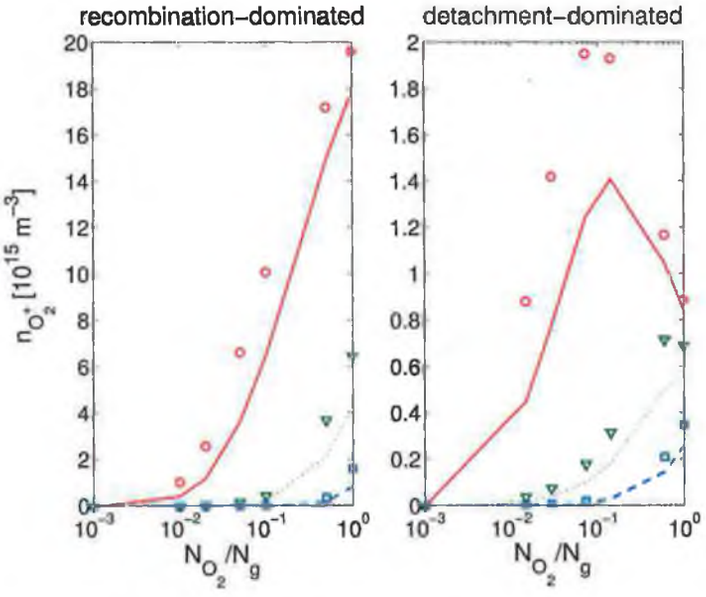

Figure 5.7: *O_2^+ ion densities as a function of gas composition and pressure. Symbols/lines retain the identities listed under figure 5.4.*

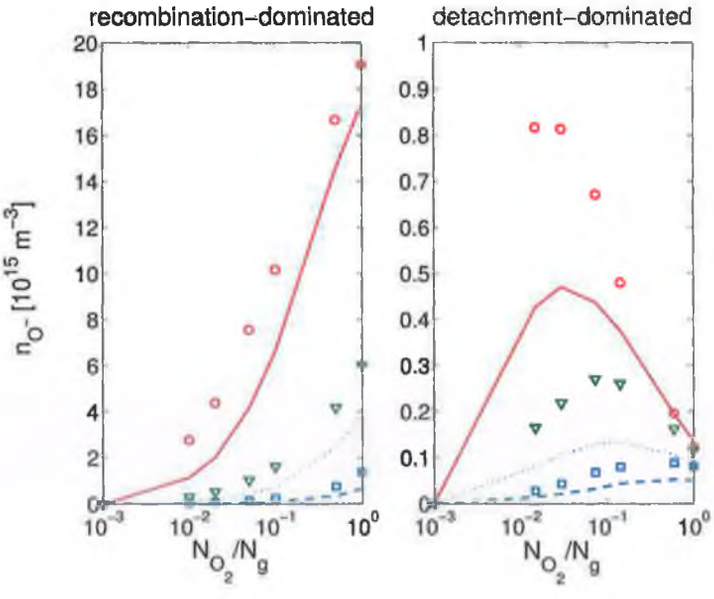

Figure 5.8: *O^- densities as a function of gas composition and pressure. Symbols/lines retain the identities listed under figure 5.4.*

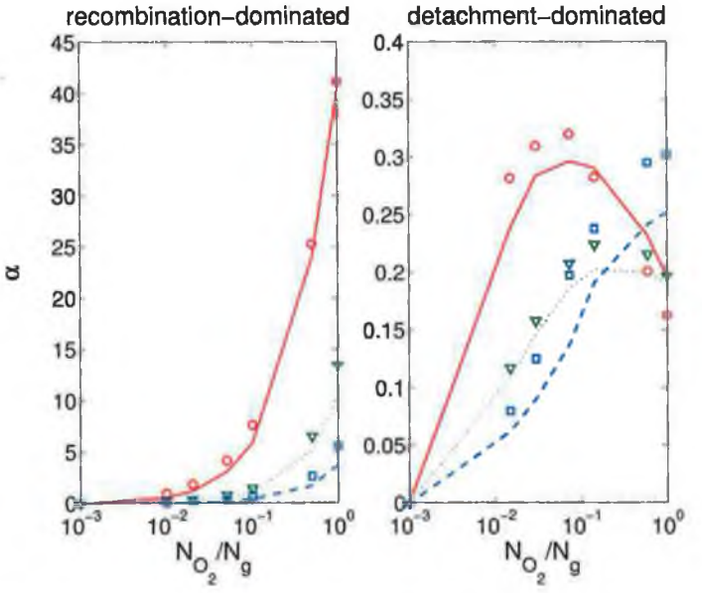

Figure 5.9: *Electronegativity, α, as a function of gas composition and pressure. Symbols/lines retain the identities listed under figure 5.4.*

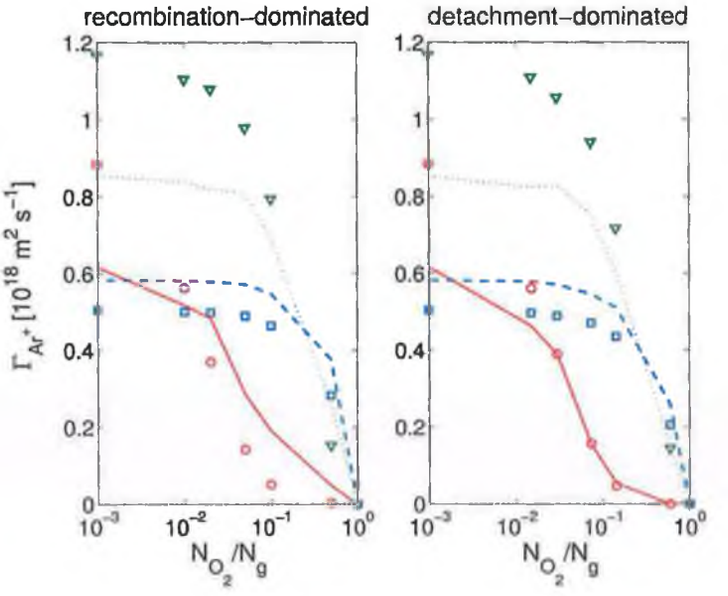

Figure 5.10: *Ar^+ wall flux as a function of gas composition and pressure. Symbols/lines retain the identities listed under figure 5.4.*

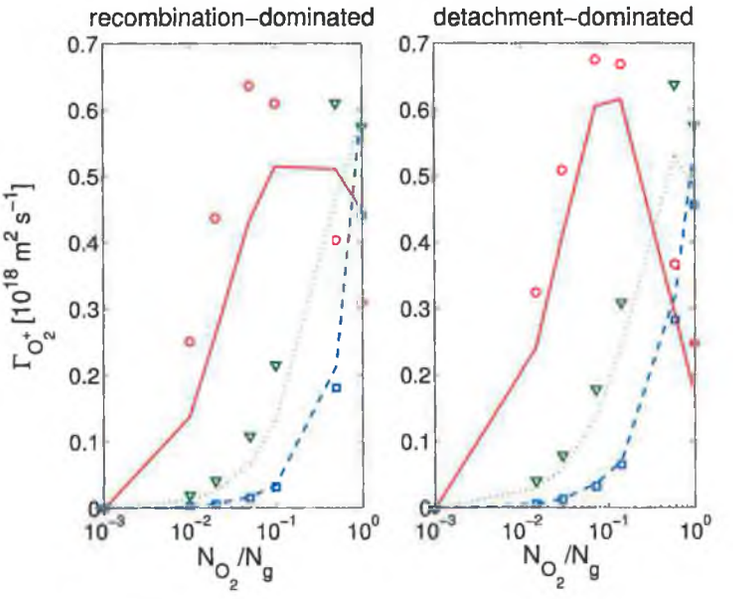

Figure 5.11: *O_2^+ wall flux as function of gas composition and pressure. Symbols/lines retain the identities listed under figure 5.4.*

5.3 Discussion

5.3.1 Electropositive Model

Looking first at the more tractable electropositive data shown in figure 5.1, a significant feature is the model's propensity to consistently underestimate the electron temperature and over estimate the electron density. While these descrepancies comprise all model approximations with respect to the simulations, we have found that they may be largely accounted for by explicitly identifying the difference between the global model parameter n, and the simulation parameters n_0 (the centre density) and $\bar{n}$ (the volume average density).

Consider a simple electropositive single-component, atomic discharge. Ignoring metastables, the only electron-gas interactions are ionization, ground-

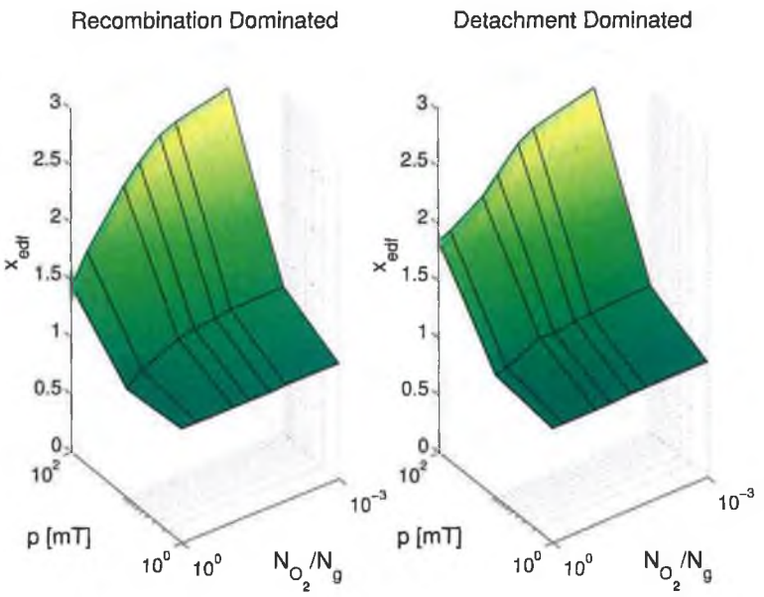

Figure 5.12: *EEDF parameter x as a function of gas composition and pressure. Symbols/lines retain the pressure values indicated under figure 5.4, only now lines correspond to the recombination-dominated regime while symbols correspond to the detachment-dominated regime.*

state excitation and elastic collisions. It is convenient to continue to assume uniform electron temperature and neutral gas density, giving spatially independent ionization and elastic collision frequencies ($\nu_{iz}(T_e)$ and $\nu_{el}(T_e)$, respectively). Global model particle balancing then gives [1]

$$nu_B A_{\text{eff}} = n\nu_{iz} V \tag{5.11}$$

$$\Rightarrow \frac{\nu_{iz}(T_e)}{u_B(T_e)} = \frac{A_{\text{eff}}}{V} \tag{5.12}$$

while simulation particle balance gives

$$n_0 u_B A_{\text{eff}} = \bar{n}\nu_{iz} V \tag{5.13}$$

$$\Rightarrow \frac{\nu_{iz}(T_e)}{u_B(T_e)} = \frac{n_0}{\bar{n}} \frac{A_{\text{eff}}}{V} > \frac{A_{\text{eff}}}{V} \tag{5.14}$$

Thus,

$$T_{e,\text{model}} < T_{e,\text{sim}} \tag{5.15}$$

Now, similar explicit balancing of the absorbed power leads to the global model balance equation

$$P = \mathcal{E}_{iz}\nu_{iz} nV + \mathcal{E}_*\nu_* nV + \frac{3}{2}\delta_i^e k_B T_e \nu_{el} nV + A_{\text{eff}}\left[\frac{5}{2}k_B T_e + eV_s\right] u_B n \tag{5.16}$$

giving

$$n = P\Big\{\mathcal{E}_{iz}\nu_{iz}V + \mathcal{E}_*\nu_*V + \frac{3}{2}\delta_i^e k_B T_e \nu_{el} V + A_{\text{eff}}\Big[\frac{5}{2}k_B T_e + eV_s\Big]u_B\Big\}^{-1} \quad (5.17)$$

While simulation power/energy balance leads to

$$P = \mathcal{E}_{iz}\nu_{iz}\bar{n}V + \mathcal{E}_*\nu_*\bar{n}V + \frac{3}{2}\delta_i^e k_B T_e \nu_{el}\bar{n}V + A_{\text{eff}}\Big[\frac{5}{2}k_B T_e + eV_s\Big]u_B n_0 \quad (5.18)$$

giving

$$\bar{n} = P\Big\{\mathcal{E}_{iz}\nu_{iz}V + \mathcal{E}_*\nu_*V + \frac{3}{2}\delta_i^e k_B T_e \nu_{el} V + A_{\text{eff}}\Big[\frac{5}{2}k_B T_e + eV_s\Big]u_B\frac{n_0}{\bar{n}}\Big\}^{-1} \quad (5.19)$$

and

$$n_0 = P\Big\{\mathcal{E}_{iz}\nu_{iz}V\frac{\bar{n}}{n_0} + \mathcal{E}_*\nu_*V\frac{\bar{n}}{n_0} + \frac{3}{2}\delta_i^e k_B T_e \nu_{el} V\frac{\bar{n}}{n_0} + A_{\text{eff}}\Big[\frac{5}{2}k_B T_e + eV_s\Big]u_B\Big\}^{-1} \quad (5.20)$$

This indicates the relation

$$\bar{n} < n < n_0 \quad (5.21)$$

contradicting figure 5.1.

In deriving this second relation we have ignored (5.15). The lower value of T_e implicit in the global model approximation leads to correspondingly lower values of ν_{iz}, ν_*, ν_{el}, u_B and V_s. From equation (5.17) we see that this will typically increase the value of n such that a simple relation between n and n_0 no longer exists, and n may well exceed n_0.

Introducing the modified ion transport parameter

$$h_i' = \frac{n_{0+}}{\bar{n}_p} h_i \tag{5.22}$$

in place of h_i in the model (where the dimensionless coefficient $n_{0+}/\bar{n}_p$ was obtained from the simulations), leads to the model results represented by hollow squares in figure 5.1.

The increased number of charged species and chemical reactions inherent in an electronegative discharge prohibits us from extending this analysis to the electronegative simulations. However, in the limit of high electronegativity, volume ion/electron loss dominates wall losses (figure 5.13) and the ambiguity of the model parameter, n, is significantly lessened. Thus, one may expect $n \to \bar{n}$ in this limit. Unfortunately, this limit is also associated with core-halo structure formation, and so one must reconsider what is meant by the term $\bar{n}$.

5.3.2 Electronegative Model

Consider a simple, three species, electronegative discharge with a uniform fixed background gas and a electronegative-electropositive core-halo structure. A rigid global model chemistry scheme may be expressed as follows:

$$V\frac{d\bar{n}_e}{dt} = K_{iz}\bar{n}_g\bar{n}_e V - K_{att}\bar{n}_g\bar{n}_e V + K_{det}\langle n_*\rangle_c\langle n_n\rangle_c V_- - Ah_B u_B n_p \tag{5.23}$$

$$V\frac{d\bar{n}_p}{dt} = K_{iz}\bar{n}_g\bar{n}_e V - K_{rec}\langle n_p\rangle_c\langle n_n\rangle_c V_- - Ah_B u_B n_p \tag{5.24}$$

$$V\frac{d\bar{n}_n}{dt} = K_{\text{att}}\bar{n}_g\bar{n}_e V - K_{\text{det}}\langle n_*\rangle_c\langle n_n\rangle_c V_- - K_{\text{rec}}\langle n_p\rangle_c\langle n_n\rangle_c V_- \qquad (5.25)$$

where $\langle n_k\rangle_c$ is the volume average density of species k taken over the core volume only, n_k is the centre density value of species k, and V_- is the volume of the electronegative core.

Clearly, there are two distinct expressions for the volume reaction rate, R, in the above scheme. When a reaction involves no negative ion species it is expressed as

$$R_j = K_j \sum_k \bar{n}_k \qquad (5.26)$$

while reactions involving one or more core-confined negative ions are expressed as

$$R_j = \frac{V_-}{V} K_j \sum_k \langle n_k\rangle_c \qquad (5.27)$$

As this model only solves for the volume average densities we must rewrite the terms on the rhs of equations (5.23), (5.24) and (5.25) in terms the volume average densities, $\bar{n}_k$, only. To do this we, once again, make the substitution $n_p \approx \bar{n}_p$ for the ion Bohm flux and introduce a new variable, $\chi_k = \langle n_k\rangle_c/\bar{n}_k$. Thus, equation (5.27) becomes

$$R_j = \frac{V_-}{V} K_j \sum_k \bar{n}_k\chi_k \qquad (5.28)$$

With some additional assumptions/simplifications we can construct crude generic estimates for the variable χ_k for three general cases: k is a neutral/electron, k is a core-confined negative ion, k is a positive ion. Profile

variation within each of the two regions is still ignored.

The first case can be simply modeled by $\chi_k = 1$. For the second case we simply note that, by definition,

$$\langle n_k \rangle_c V_- = \bar{n}_k V \tag{5.29}$$

which gives

$$\chi_k = \frac{V}{V_-} \tag{5.30}$$

The final case is slightly more complicated, as the core and volume average densities are not simply related for positive ions. However, we may estimate the core density by assuming an ion independent value for χ. Quasi-neutrality gives

$$V \sum_i n_{i(+)} = \sum_i \langle n_{i(+)} \rangle_c V_- + \bar{n}_e (V - V_-) \tag{5.31}$$

$$\Rightarrow \frac{\langle n_{k(+)} \rangle_c}{\bar{n}_{k(+)}} = \chi_{k(+)} \approx \chi_+ = \frac{\sum_i \langle n_{i(+)} \rangle_c}{\sum_i \bar{n}_{i(+)}} = \frac{V}{V_-} - \frac{\bar{n}_e}{\sum_i \bar{n}_{i(+)}} \left(\frac{V - V_-}{V_-} \right) \tag{5.32}$$

Using these simple models for χ, and including the dimensionless core parameter V/V_- as an additional input, we can explicitly incorporate core-halo stratification into equations (5.23), (5.24) and (5.25) leading to the following equation set

$$\frac{d\bar{n}_e}{dt} = K_{\mathrm{iz}} \bar{n}_g \bar{n}_e - K_{\mathrm{att}} \bar{n}_g \bar{n}_e + K_{\mathrm{det}} \bar{n}_* \bar{n}_n - \frac{A}{V} h_B u_B n_p \tag{5.33}$$

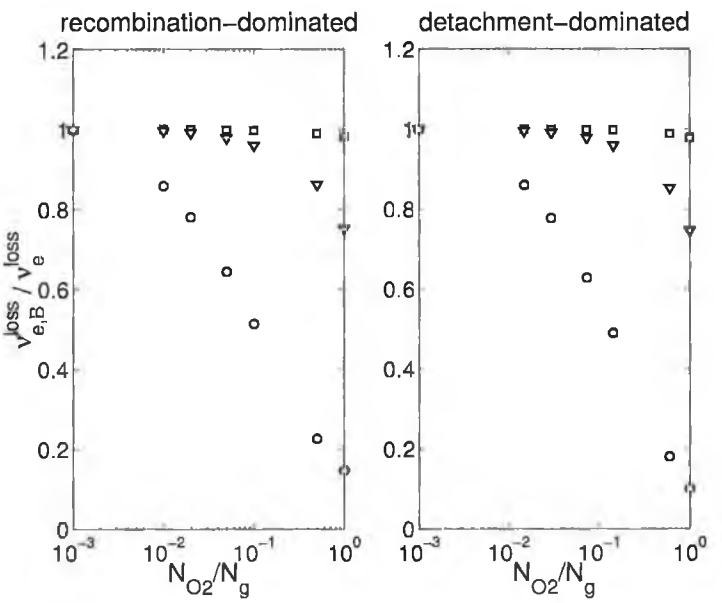

Figure 5.13: *Ratio of electron surface loss frequency ($\nu_{e,B}^{loss}$) to total electron loss frequency (ν_e^{loss}) estimated by the global model and show as a function of gas composition and pressure. Symbols retain the identities listed under figure 5.4.*

$$\frac{d\bar{n}_p}{dt} = K_{\text{iz}}\bar{n}_g\bar{n}_e - K_{\text{rec}}\bar{n}_p\bar{n}_n\chi_+ - \frac{A}{V}h_B u_B n_p \tag{5.34}$$

$$\frac{d\bar{n}_n}{dt} = K_{\text{att}}\bar{n}_g\bar{n}_e - K_{\text{det}}\bar{n}_*\bar{n}_n - K_{\text{rec}}\bar{n}_p\bar{n}_n\chi_+ \tag{5.35}$$

This is identical to the elementary volume averaged formulation with an additional factor of χ_+ incorporated into the ion-ion recombination term. This accounts for the original observation that the global model formulation appears to be relatively robust when applied to structured discharges.

The effective profile difference between the single region and the two region volume averaged models is illustrated in figure 5.14, while the efficacy of the new model is shown in figures 5.15–5.21. Note, these figures compare the two models in the recombination-dominated limit only.

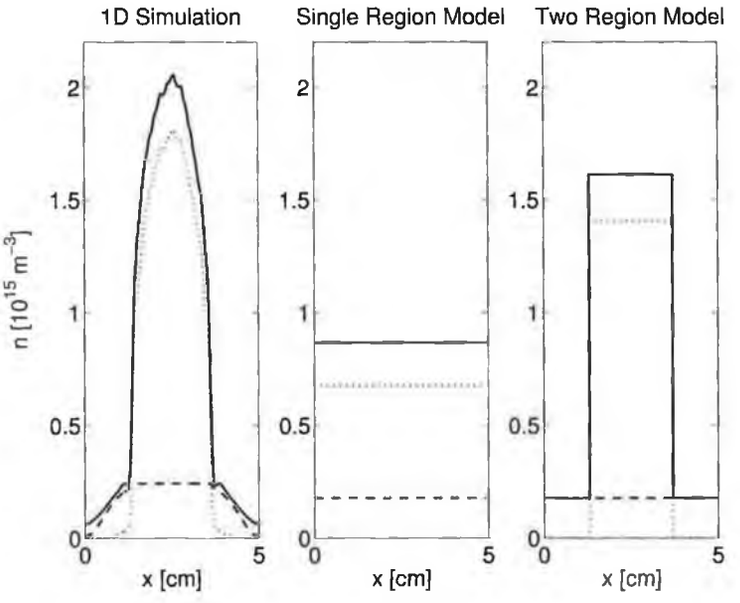

Figure 5.14: *Left: simulated density profiles. Middle: volume average model equivalent. Right: two region model equivalent. Lines retain the identities listed under figure 5.4*

There is a notable improvement in quantitative model-simulation agreement in the recombination-dominated regime. However, as predicted, there was little discernible change in the output of the model in the detachment-dominated limit, where ion-ion recombination has a negligible impact on chemistry. As most qualitative features have already been recovered using the simpler model, it is not surprising that the inclusion of spatial structure does not add markedly to the qualitative agreement. In contrast, assuming a Maxwellian EEDF while continuing to utilize the two region model once again renders the model ineffectual in the transitional to collisional regimes.

Figure 5.22 illustrates the relative dependence of the primary discharge state-variable on both x and V_{-}. It is clear that qualitative and quantitative behavior is effected as the EEDF departs from a Maxwellian, with significant qualitative variation over a small range close to $x = 1$, $1.2 \geq x \gtrsim 1$.

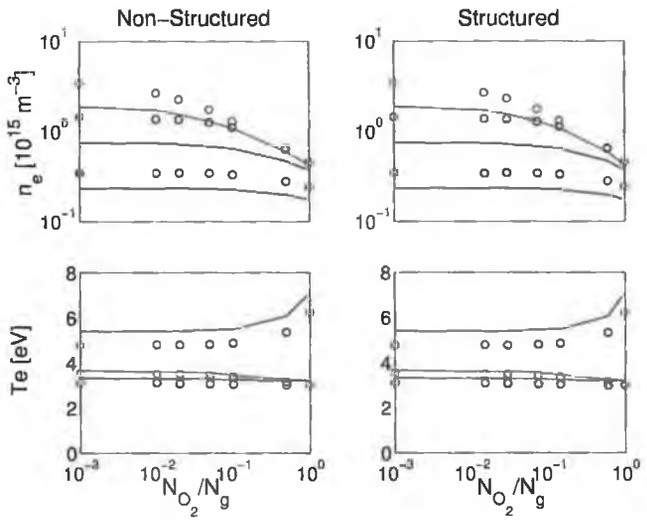

Figure 5.15: *Electron parameters as a function of gas composition and pressure.* **Left:** *Classical volume averaged model;* **Right:** *Two region model. Recombination-dominated simulations used for comparison as these show the greatest change in model efficacy (as predicted). Symbols/lines retain the identities listed under figure 5.4.*

However, it should be noted that this variation predominantly reflects the relationship between the EEDF parameter, x, and the rate constants, K_j. The non-Maxwellian amendments to equations (5.8), (5.9) and (5.10) do not appear to significantly enhance model fidelity. By substituting for these expressions with their more conventional Maxwellian formulations, while continuing to use the non-Maxwellian EEDF to evaluate reaction rate constants, it was found that the densities estimated by the model changed by $< 5\%$, with little discernible loss in qualitative model-simulation agreement. The distortion of the ion wall flux values was notably greater ($< 20\%$). This behavior is examined in more detail in Appendix D.

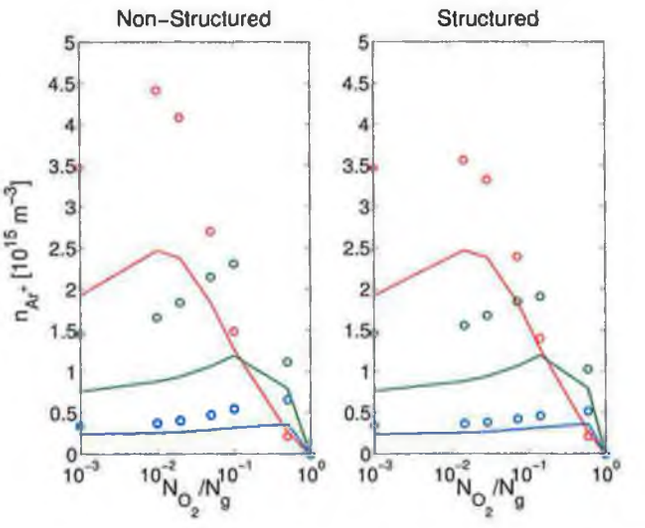

Figure 5.16: *Layout, as per figure 5.15. Compares Ar^+ ion densities as a function of gas composition and pressure. Symbols/lines retain the identities listed under figure 5.4.*

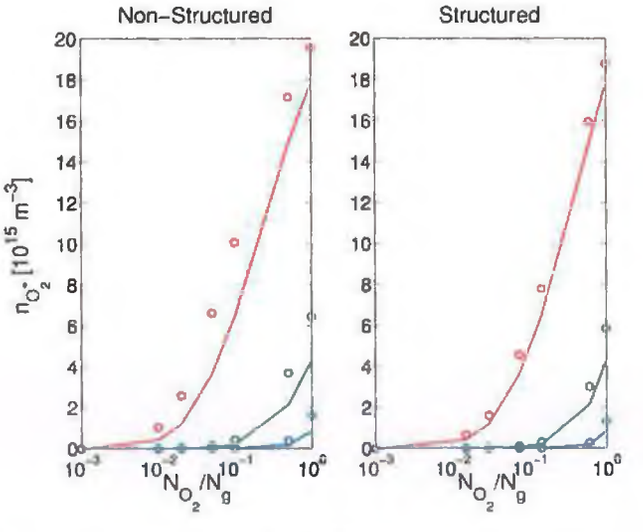

Figure 5.17: *Layout, as per figure 5.15. Compares O_2^+ ion densities as a function of gas composition and pressure. Symbols/lines retain the identities listed under figure 5.4.*

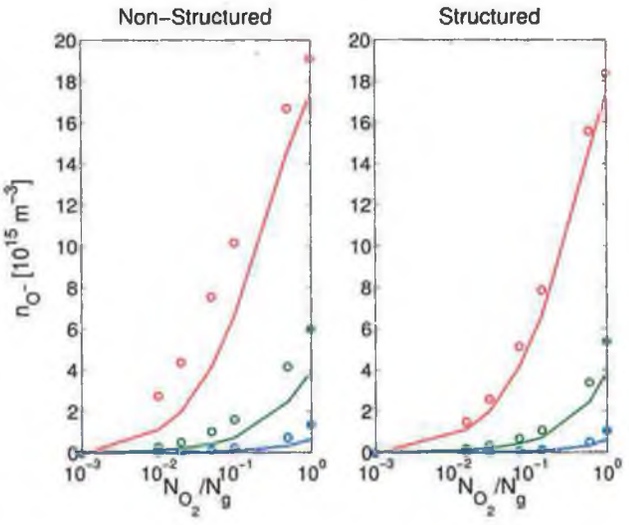

Figure 5.18: *Layout, as per figure 5.15. Compares O^- ion densities as a function of gas composition and pressure. Symbols/lines retain the identities listed under figure 5.4.*

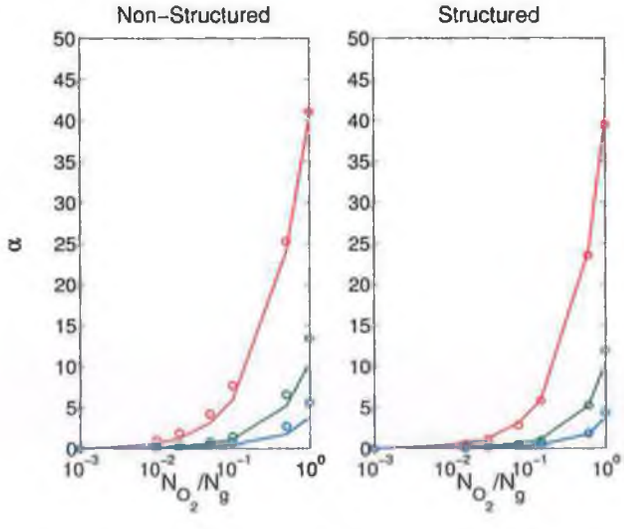

Figure 5.19: *Layout, as per figure 5.15. Compares $\bar{\alpha}$ as a function of gas composition and pressure. Symbols/lines retain the identities listed under figure 5.4.*

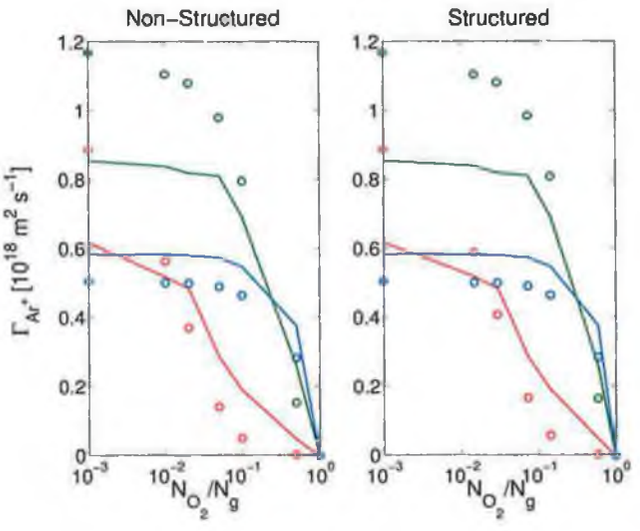

Figure 5.20: *Layout, as per figure 5.15. Compares Ar^+ wall flux as a function of gas composition and pressure. Symbols/lines retain the identities listed under figure 5.4.*

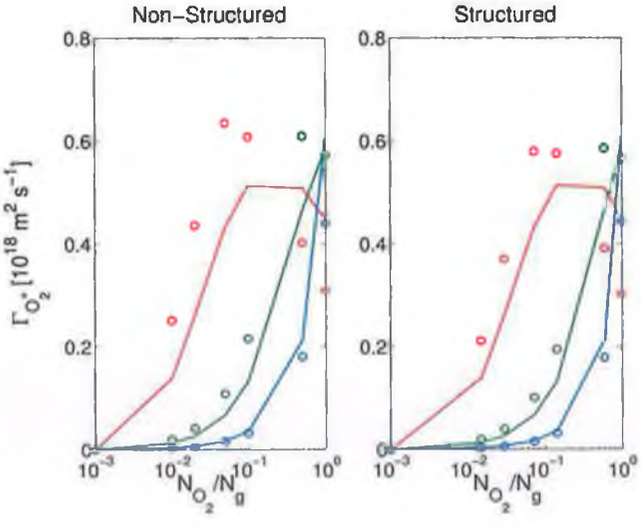

Figure 5.21: *Layout, as per figure 5.15. Compares O_2^+ wall flux as as a function of gas composition and pressure. Symbols/lines retain the identities listed under figure 5.4.*

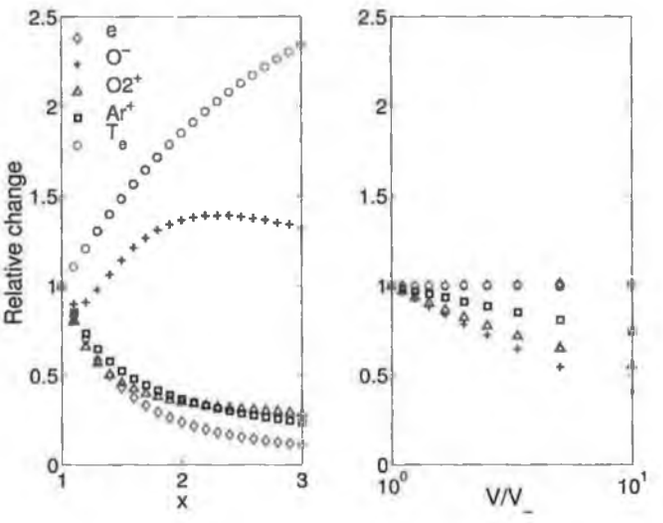

Figure 5.22: *Relative variation in plasma state variables as a function of the EEDF parameter x (left), and the electronegative core fraction V/V_ (right). Ar/O_2 discharge: 100 mT 99 % Ar, 1 % O_2.*

CHAPTER

6

Conclusion

A comprehensive set of low pressure PIC-MCC simulations has been compiled for the purpose of benchmarking. We have used this data to explore the validity of the most prevailing assumptions pertaining to such discharges and to assess the performance of some of the most prevalent analytical treatments and approximations. To assist in this we have compiled a rather extensive critique of the associated literature. We have also utilized this benchmark data to characterize and quantify the efficacy of the fundamental global model approximations, with emphasis on modeling structured electronegative discharges.

6.1 Electronegative Benchmark Study

We noted in our introduction that it is only in recent years that a consistent interpretation of the long-time appreciated discharge structure has begun to emerge. An influential body of work [32, 38, 40, 64], which forms part of this emerging consensus, has been repeatedly castigated by a small, but

very active, group of researchers [20, 52, 53, 54]. These researchers go so far as to accuse this work of 'contaminating' the literature [20] and imply its proliferation has contributed to the obscure nature of the subject. We have shown that this criticism is unjustified, does not withstand scrutiny, and is itself likely to have played a significantly role in obscuring the literature.

It was found that, for a given pressure and attachment rate, detachment dominated discharges have necessarily lower electronegativities and, in the limit of low pressure, have significantly greater negative ion temperatures (or, more correctly, kinetic energy densities). The reduced electronegativity and increased ion temperature also notably alters the discharge structure, and decreases the likelihood of positive ions attaining the local ion sound speed other than at the conventional sheath edge.

In the recombination dominated limit, quasi-neutrality was observed to fail at the abrupt transition between the electronegative and electropositive plasma. This produced a well defined localized double-layer structure, on the order of several Debye lengths thick. This space-charge layer confined cooler negative particles to the core and injected positive ions into the edge with an increased velocity. As a result, the plasma properties on either side of this layer are markedly different. The observed potential profiles were, in all cases, monotonic and the double layers consisted of a single positive and adjoining negative space-charge layer.

Extending the treatment of Stangeby and Allen [5], we have shown that satisfaction of the Bohm criterion is both a sufficient and necessary condition for quasi-neutrality violation in the limit of $\lambda_D/L \to 0$. However, in our simulations, where $\lambda_D/L > 0$, we observed that the ion speed at the edge of the double layer is considerably lower than the local ion sound speed.

At sufficient O_2 metastable densities ($O_2(a^1\Delta_g)$) the discharge shifts

back towards the recombination dominated limit as the Ar concentration is increased. Although there is an associated decrease in attaching gas density it was found that the negative ion density may actually increase with increasing Ar concentration.

The propensity for negative ions to form at all points in the discharge potential well, resulted in the distinct energy distributions depicted in figure 4.18. The observed increase in negative ion temperature, as the dominant negative ion loss mechanism is switched from recombination-dominated to detachment-dominated, has been attributed to the significant reduction in the life time of the negative ions, many of which are created in the high field electropositive region and destroyed before thermalising to the gas temperature. A simple energy balance model was constructed, supporting this fact and, for the first time, allowing the negative ion energy to be estimated in a simple manner.

Parameters such as D_{a+} and l_{-} were found to be sensitive to the value of the negative ion temperature, with poor approximations ensuing from the popular assumption $\gamma_n = \gamma_p = \gamma_g$.

6.2 Survey of the Global Model Approximation

The application of this benchmark data set to the study of the global model approximation, also yielded some interesting results. As expected, the most significant limitation on such models was shown to be the frequently employed assumption of a Maxwellian EEDF. Significant improvement in model performance was obtained by adopting the non-Maxwellian modifications proposed in [133]. This method may be easily incorporated into existing global model algorithms with negligible computational cost.

The electron temperature was found to be sensitive to relatively small

changes in the EEDF parameter, x. Changing the value of x from 1.0 (Maxwellian) to 1.28 at 10 mT (in accordance with the simulation data) was seen to increase the value of T_e by $> 20\%$. Such departure from a Maxwellian distribution may well go unnoticed/ignored in experimental measurement.

It was found that the volume averaged chemistry approximation was quite robust to the formation of electronegative-electropositive discharge segregation. Modifying the model to account for this structure (in a volume averaged manner) was seen to give, at best, a modest improvement in quantitative model efficacy only. This is further illustrated in figure 5.22, where the relationship between the primary discharge state-variables can be seen to vary both qualitatively and quantitatively as the parameter x is varied, while only a quantitative deviation is observed as the core fraction, V/V_{-} is increased from 1 to 10.

Finally, it is important to stress we are not advocating that efforts made to incorporate one-dimensional structure analysis into the global model formulation have been extraneous. In fact, such detailed modifications may be requisite when state variables are particularly sensitive to the electron-ion wall losses, or when one has a particular interest in modeling this property. However, bulk discharge chemistry appears to be more robust to the occurrence of ion profile structures than one might assume. In the limit of high electronegativity, where the electron density may be substantially lower than the plasma density, one should not expect cogent global model efficacy without also considering the non-Maxwellian nature of the EEDF.

CHAPTER

7

The Appendix

Appendix A

Franklin Tests

In [52], Franklin and Snell criticize the related works of Lichtenberg *et al* [32, 38, 64], Lieberman and Lichtenberg [23], and Kouznetsov *et al* [40, 85], stating that, when deriving an expression for the ambipolar diffusion constant, D_{a+} (equation (2.14)), it was inconsistent to assume that both negative species are in thermal equilibrium

$$\frac{\nabla n_e}{n_e} = -\frac{eE}{k_B T_e} \qquad \frac{\nabla n_n}{n_n} = -\frac{eE}{k_B T_e} \tag{A-1}$$

and that the electronegative profile was flat

$$\alpha(x) = \alpha_0 \qquad 0 \leq x \leq l_- \tag{A-2}$$

unless $T_n = T_e$. As noted in section 2.2.8, this statement is true but the criticism is unwarranted as these authors never made the assumption $\alpha(x) = \alpha_0$.

To stress this point, Franklin and Snell [52] devised five tests to test for physical consistency in limiting cases. Without demonstration, they simply conclude by noting that the expression derived in [38] fails all but one of these tests.

We will show below that this is not the case. We will not be using equation (2.14), however, as this has the additional assumptions that $\mu_n/\mu_c, \mu_p/\mu_c \ll 1$ and $\gamma_n \approx \gamma_p$. Starting instead with equation (2.12) and dividing the top and bottom by μ_c gives

$$D_{a+} = D_p \left\{ \frac{(1+\alpha\frac{\mu_n}{\mu_e}) + \frac{\mu_p}{\mu_e}(1+\alpha)\frac{D_e}{D_p}\frac{\nabla n_e}{\nabla n_p} + \frac{\mu_p}{\mu_e}(1+\alpha)\frac{D_n}{D_p}\frac{\nabla n_n}{\nabla n_p}}{1+\alpha\frac{\mu_n}{\mu_e} + (1+\alpha)\frac{\mu_p}{\mu_n}} \right\} \quad \text{(A-3)}$$

Assuming, both negative species are in thermal equilibrium

$$\frac{\nabla n_n}{n_n} = \gamma_n \frac{\gamma n_e}{n_e} \quad \text{(A-4)}$$

and zero current

$$\nabla n_p = \nabla n_n + \nabla n_e \quad \text{(A-5)}$$

we may derive the following relations for the density gradients

$$\frac{\nabla n_e}{\nabla n_p} = \frac{1}{1+\gamma_n\alpha} \qquad \frac{\nabla n_n}{\nabla n_e} = \frac{\gamma_n\alpha}{1+\gamma_n\alpha} \quad \text{(A-6)}$$

while the Einstein relation becomes

$$\frac{D_e}{D_p} = \gamma_p \frac{\mu_e}{\mu_n} \qquad \frac{D_n}{D_p} = \frac{\gamma_p}{\gamma_n}\frac{\mu_n}{\mu_p} \quad \text{(A-7)}$$

Substituting (A-6) and (A-7) into (A-3) gives

$$D_{a+} = D_p \left\{ \frac{\left(1+\frac{\mu_n}{\mu_e}\alpha\right) + \frac{(1+\alpha)\gamma_n}{1+\gamma_n\alpha} + \frac{\mu_n}{\mu_e}\frac{(1+\alpha)\gamma_p\alpha}{1+\gamma_n\alpha}}{1+\frac{\mu_n}{\mu_e}\alpha + \frac{\mu_n}{\mu_e}(1+\alpha)} \right\} \quad \text{(A-8)}$$

Tests

1. *when $\alpha = 0$ the standard result is recovered;*

   Setting $\alpha = 0$ gives

$$\begin{aligned} D_{ap} &= D_p \frac{1+\gamma_p}{1+\mu_p/\mu_e} \\ &= D_p \frac{1+\mu_p D_e/\mu_e D_p}{1+\mu_p/\mu_e} \\ &= D_p \frac{\mu_e D_p + \mu_p D_e}{\mu_e + \mu_p} \end{aligned} \tag{A-9}$$

   $\Rightarrow$ *passed*

2. *if we interchange the subscripts e and n and then replace α_0 by $1/\alpha_0$ the expression remains the same;*

   Substitutions

$$\begin{aligned} \mu_n &\rightarrow \mu_e \\ \mu_e &\rightarrow \mu_n \\ \mu_p &\rightarrow \mu_p \\ \alpha &\rightarrow 1/\alpha \\ \gamma_n &\rightarrow 1/\gamma_n \\ \gamma_p &\rightarrow \gamma_p/\gamma_n \end{aligned} \tag{A-10}$$

   give

$$D_{a+} = D_p \left\{ \frac{1 + \frac{\mu_e}{\mu_n}\frac{1}{\alpha} + \frac{(1+1/\alpha)\gamma_p/\gamma_n}{1+1/\gamma_n\alpha} + \frac{\mu_e}{\mu_n}\frac{(1+1/\alpha)\gamma_p/(\gamma_n-\alpha)}{1+1/\gamma_n\alpha}}{1 + \frac{\mu_e}{\mu_n}\frac{1}{\alpha} + \frac{\mu_p}{\mu_n}\left(1+\frac{1}{\alpha}\right)} \right\} \tag{A-11}$$

$\Rightarrow$ *passed*

3. *in the limit* $\alpha_0 \to \infty$ *we find the corresponding expression to* $\alpha_0 \to 0$ *with* n *replacing* e*;*

$$\begin{aligned} \lim_{\alpha\to\infty} D_{a+} &= D_p \left[\frac{\mu_n/\mu_e + \mu_n\gamma_p/\mu_e\gamma_n}{\mu_n/\mu_e + \mu_p/\mu_e} \right] \\ &= D_p \left[\frac{1 + T_n/T_p}{1 + \mu_p/\mu_n} \right] \end{aligned} \tag{A-12}$$

replace n with e in (A-8)

$$\lim_{\alpha\to 0} D_{a+} = D_p \frac{1+\gamma_p}{1+\mu_p/\mu_e} \tag{A-13}$$

$\Rightarrow$ *passed*

4. *if then we set* $\mu_n = \mu_p = \mu_i$ *and* $T_n = T_p = T_i$ *then* $\Gamma = -\nabla n \cdot \mu_i T_i$ *and* $E \equiv 0$*;*

Making the appropriate substitutions in (A-12), it can easily be shown to give $D_{a+} = D_i = \mu_i T_i$.

Next, combining the drift diffusion equations for positive ions, negative ions, and electrons, we may solve for E, yielding

$$E = -\frac{\nabla n_e}{n_e} \frac{D_e + \alpha D_n - (\alpha+1)D_p}{\mu_e + \alpha\mu_n + (\alpha+1)\mu_p} \tag{A-14}$$

which clearly approaches zero in the limit $\alpha \to \infty$ when $\mu_n = \mu_p = \mu_i$ and $T_n = T_p = T_i$.

$\Rightarrow$ *passed*

5. *if all types of particles have the same mobility and temperature* μ *and* T *then* $\Gamma = -\nabla n \cdot \mu T$ *independent of* α_0*;*

   Substituting

$$\mu_e = \mu_p = \mu_n = \mu \tag{A-15}$$

$$T_e = T_p = T_n = T \tag{A-16}$$

$$\Rightarrow \gamma_p = \gamma_n = 1 \tag{A-17}$$

   into (A-14), one immediately finds that $E \equiv 0$.

   Making the same substitutions in (A-8) gives

$$D_{a+} = \mu T \frac{1 + \alpha + \dfrac{1+\alpha}{1+\alpha} + \dfrac{(1+\alpha)\alpha}{1+\alpha}}{1 + \alpha + 1 + \alpha} = \mu T \tag{A-18}$$

   $\Rightarrow$ *passed*

Appendix B

Core Size Estimation

As discussed in section [60], we may estimate the size of the electronegative core by integrating the negative ion continuity equation, assuming a characteristic negative ion profile shape and utilizing the boundary condition of vanishing flux. In figures B-2, B-3, B-4 and B-5 we have plotted the core size estimates obtained assuming the profile shapes discussed earlier.

Figure B-4 clearly stands out as being the only figure without a full range of solutions. The core size estimates shown in this figure have been generated by assuming a truncated parabolic profile and using equation (4.13) to approximate the scale-length l. In fact only handful of solutions have been found. In all other cases we find there is no solution to (4.13) within the domain $l_- \leq l < \infty$. Examining the limits of this domain, we find that an acceptable solution to equation (4.13) only exists if

$$\frac{u_{B0} l_-}{2\alpha_0} \leq D_{a+} < \infty \tag{B-1}$$

However, this is not a damning observation. In most cases where a solution was not found quasi-neutrality was either preserved, or only marginally violated, at the core-halo transition point. Unfortunately, where solutions are obtained, agreement between the analysis and the simulation is marginal.

In the three pure O_2 simulations, a solution was found, albeit only at the lower limit the solution domain in the 100 mT simulation (i.e. $l = l_-$). The non-existence of solutions in the limit of high Ar concentration with moderate quasi-neutrality violation may also reflect the rather ad hoc extension of this theory to the limit of multiple positive ions.

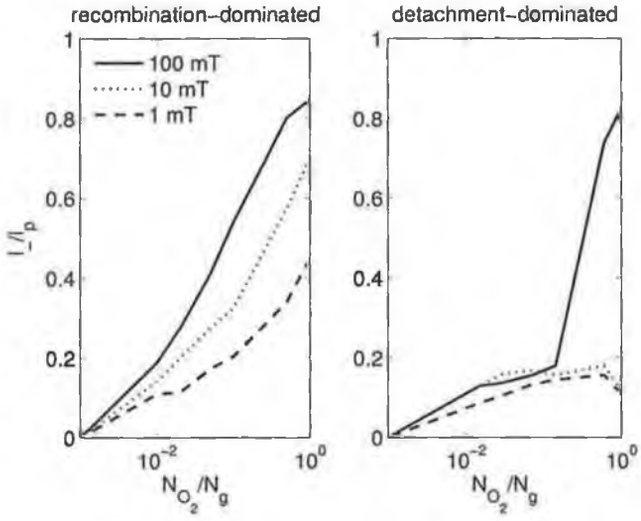

Figure B-1: *Approximated core size extracted from the simulation shown as a function of gas composition and pressure.*

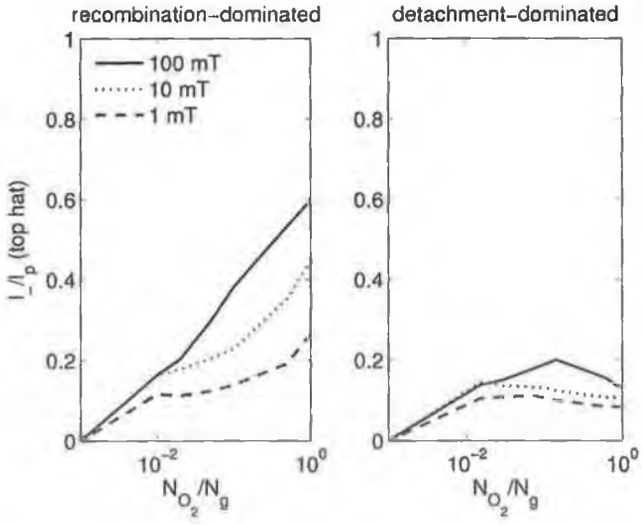

Figure B-2: *Core size estimated using equation (4.18) assuming a top had negative ion profile and a parabolic electron edge profile.*

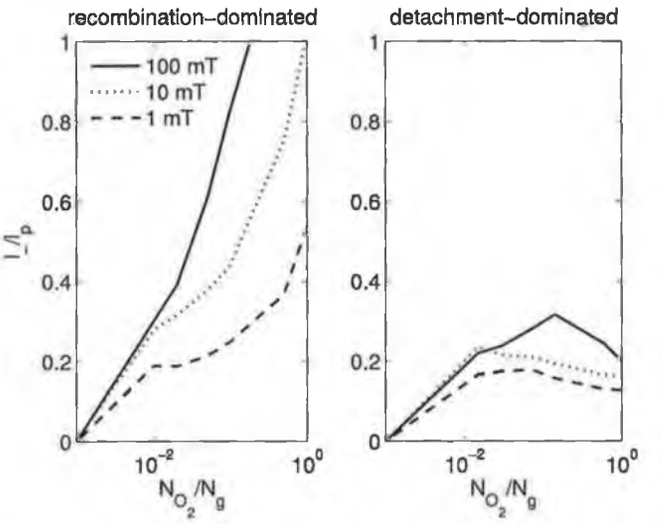

Figure B-3: *Core size estimated using equation (4.18) assuming a parabolic negative ion profile and a parabolic electron edge profile.*

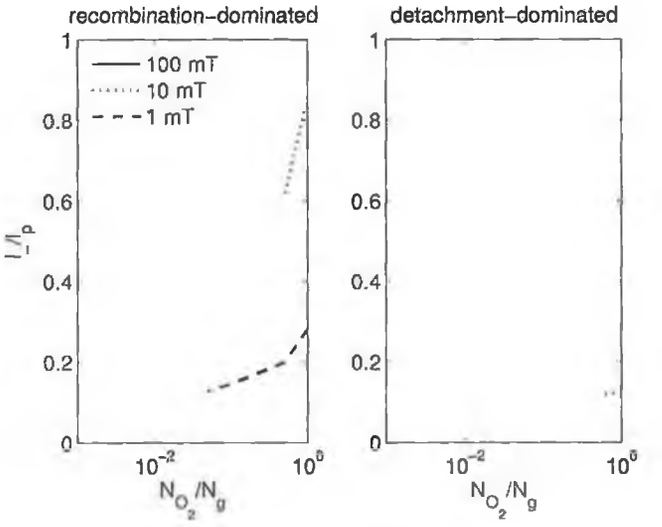

Figure B-4: *Core size estimated using equation (4.18) assuming a truncated parabola with l estimated using equation (4.13). Note only a limit number of solutions exist. Solution for pure O_2 recombination dominated exists, but gives $l_- \approx l$, which gives a estimate for $l_-/l_p > 1$ (see figure B-3).*

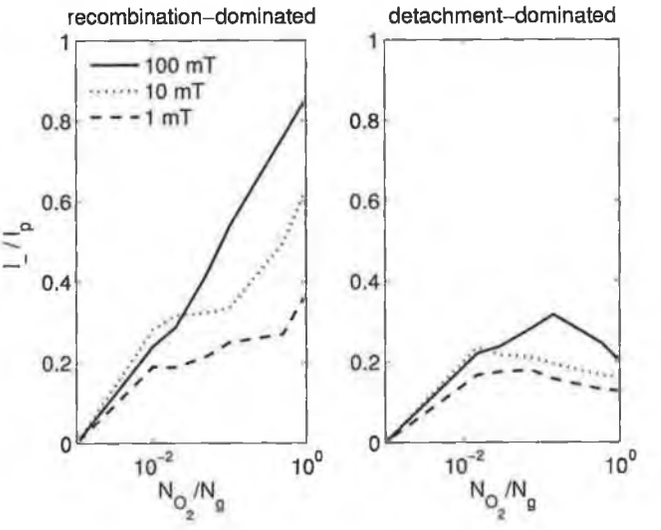

Figure B-5: *Core size estimated using equation (4.18) assuming a truncated parabola with l estimated using equation (4.27).*

Appendix C

Ion Transport Parameter

Godyak and Maksimov 1977

Godyak and Maksimov [44] constructed a simple one-dimensional two-species, quasi-neutral, electropositive, steady-state plasma fluid model with finite ion inertia effects assuming a constant ion mean free path. Electron-ion pairs are generated by single step ionization processes in the bulk and destroyed by recombination at the walls. This model had a particular advantage over the classical Schottky theory of the positive column, in that the density at the edge of the quasi-neutral plasma could be determined self-consistently[a]. The base equations for this model were

$$\frac{d}{dx}nv = zn \tag{C-1}$$

$$n = n_0 \exp\left(\frac{e\phi}{k_B T_e}\right) \tag{C-2}$$

$$v = \left(\frac{2\lambda_i eE}{\pi m_i}\right) \tag{C-3}$$

with the radial boundary conditions

$$\phi(0) = E(0) = 0 \tag{C-4}$$

$$v(R) = u_B = \sqrt{\frac{k_B T_e}{m_i}} \tag{C-5}$$

Analytically solving the above system of equations (with some addi-

[a]In the classical Schottky theory the edge density is a boundary condition.

tional approximations) and heuristically matching the solution to the low pressure Langmuir solution, Godyak and Maksimov obtained the following expressions for the edge to centre density ratios in planar and radial coordinates respectively

$$h_l = \frac{n_s}{n_0} = 0.86\Big(3 + \frac{l_p}{\lambda_i}\Big)^{-1/2} \tag{C-6}$$

$$h_R = \frac{n_s}{n_0} = 0.80\Big(4 + \frac{R}{\lambda_i}\Big)^{-1/2} \tag{C-7}$$

Lee *et al.* 1994

Utilizing the one dimensional high pressure electronegative discharge analysis of Lichtenberg *et al.* [38], Lee and Lieberman [43] obtained an expression for $h_{l,R}$ for a structured electronegative plasma. Heuristically matching this expression with those of Godyak and Maksimov (and their high pressure diffusion equivalents), they constructed general expressions for h which, they claimed, could be used for transitions from low to high pressure and from electropositive to electronegative regimes. However, implicit in their analysis is the assumption that the negative ion density is sufficiently low such that $D_{a+} \approx \gamma_+ D_+$ in the core[b]. The expressions obtained were

$$h_l = \frac{1 + 2\alpha_0/\gamma_+}{1 + \alpha_0} \frac{0.86}{[3 + (l_p/\lambda_i) + (0.86 l_p u_B/\pi\gamma_+ D)^2]^{1/2}} \tag{C-8}$$

$$h_R = \frac{1 + 2\alpha_0/\gamma_+}{1 + \alpha_0} \frac{0.80}{[4 + (R/\lambda_i) + \{0.80 R u_B/2.405 J_1(2.405)\gamma_+ D\}^2]^{1/2}} \tag{C-9}$$

[b]The distinction between γ_+ and γ_- was not made in the original work of Lee and Lieberman.

Kouznetsov *et al.* 1996

Shortly after the work of Lee and Lieberman, Kouznetsov *et al.* [40] derived a new expression for h in their extended treatment of the one dimensional electronegative discharge analysis. They noted that, at low pressure, the electropositive edge plasma in a planar discharge could be viewed as being equivalent to the electropositive plasma modeled by Godyak and Maksimov [44] with a finite wall directed ion flux (ions ejected from the core) at the centre/zero coordinate. They were then able to obtain an expression for h_l in terms of the velocity of the positive ions at the edge region

$$h_l = \left(\frac{a + w_0^3}{a+1}\right)^{1/3} \tag{C-10}$$

where

$$w_0 = u_{in}/u_{B0} \tag{C-11}$$

$$a = \frac{2\nu_{iz}\lambda_i}{\pi u_{B0}} \tag{C-12}$$

When the transition from electronegative core to electropositive edge occurs without the ions reaching the local ion sound speed, the ion flux at the core edge was approximated by the ambipolar expression

$$\Gamma_{in} \approx \frac{2\bar{D}_{a+} n_{e0} \alpha_0}{l} \tag{C-13}$$

where l is the length scale characterizing the parabolic negative ion profile (in this limit, $l = l_-$, the core length). Equations (C-10)–(C-13) can be solved iteratively with the following equation for l_-

$$\frac{1}{6}\ln\left(\frac{(a^{1/3}+1)^3}{a+1}\right)+\frac{1}{\sqrt{3}}\arctan\left(\frac{2-a^{1/3}}{\sqrt{3}\,a^{1/3}}\right)$$
$$-\frac{1}{6}\ln\left(\frac{(a^{1/3}+w_0)^3}{a+w_0^3}\right)-\frac{1}{\sqrt{3}}\arctan\left(\frac{2w_0-a^{1/3}}{\sqrt{3}\,a^{1/3}}\right) \qquad \text{(C-14)}$$
$$=\frac{\pi(l_p-l_-)}{2\lambda_i}a^{2/3}$$

When the transition from electronegative core to electropositive edge occurs with the ions reaching the local ion sound speed, l is no longer the same as l_- and an additional equation is needed. In this case the injected flux becomes

$$\Gamma_{in}\approx\frac{2\bar{D}_{a+}n_{e0}\alpha_0 l_-}{l^2} \qquad \text{(C-15)}$$

and the additional equation is obtained by combining quasi-neutrality and flux conservation with the assumption of a flat core electron profile

$$\frac{2\bar{D}_{a+}\alpha_0 n_{e0}l_-}{l^2}=(\alpha_-+1)n_{e0}u_B(\alpha_-) \qquad \text{(C-16)}$$

where α_- is the electronegativity at the point where the local Bohm criterion is violated, and $u_B(\alpha)$ is the ion sound speed as a function of α. From the assumption of a truncated parabolic profile

$$\alpha_-=\alpha_0\left(1-\frac{l_-^2}{l^2}\right) \qquad \text{(C-17)}$$

Note that the above expressions for h relate the electropositive edge ion density to the core edge ion density, and not the discharge centre density. If one does not solve for the ion densities at the transition point, one may still utilize this expression approximately by multiplying by an additional factor of $\frac{1}{1+\alpha_0}$.

Kim *et al.* 2006

Kim *et al.* [45, 46] identified three distinct ion profiles for a one dimensional planar electronegative discharge

1. parabolic-profile core with low pressure electropositive edge;
2. one-region electronegative plasma with parabolic-profile;
3. one-region electronegative plasma with flat profile.

An additional two-region flat-topped core profile was also identified, but is incorporated in the transition between regions 1 and 3, above. According to [64] these regimes correspond to the following regions of parameters space, respectively

1. low pressure, moderately high n_{e0}, moderate α_0;
2. low to high pressure, low n_{e0}, high α_0;
3. high pressure, moderately high n_{e0}, moderately high α_0.

The parameter space in which the positive ions may reach their local ion sound speed within the plasma (low/high pressure, moderately low n_{e0}, moderately high α_0) is not considered.

Utilizing the one dimensional analysis of [64], approximate expressions for h in each of these regimes were derived, yielding [45]

$$h_a \approx \frac{0.86}{[3+\eta(l_p/\lambda_i)]^{1/2}} \frac{1}{1+\alpha_0} \tag{C-18}$$

$$h_b \approx \left(\gamma_-^{1/2} + \gamma_+^{1/2} \frac{\eta}{\sqrt{2\pi}} \frac{l_p}{\lambda_i}\right)^{-1} \frac{\alpha_0}{1+\alpha_0} \tag{C-19}$$

$$h_c \approx \left(\gamma_-^{1/2} + \gamma_+^{1/2} \frac{n_*^{1/2} n_{+0}}{n_{-0}^{3/2}}\right)^{-1} \tag{C-20}$$

where

$$\eta = \frac{2T_+}{T_+ + T_-} \tag{C-21}$$

$$n_* = \frac{15}{56}\left(\frac{8eT_+}{\pi m_i}\right)^{1/2} \frac{\eta^2}{K_{\text{rec}}\lambda_i} \tag{C-22}$$

Equations (C-18), (C-19) and (C-20) were patched together heuristically, utilizing the linear ansatz

$$h_l = h_a + h_b + h_c \tag{C-23}$$

This approximation for h_l is expected to cover a reasonable volume of parameter space, with significant exceptions being the internal ion shock regime (identified above) and the highly electronegative regime, for which the wall sheath potential collapses and negative ions may reach reach the walls.

Comparison

Figure C-1 compares the positive ion edge densities obtained from the benchmark $O_2(/O_2(a^1\Delta_g))$ PIC simulation with those estimated using equations (C-8), (C-10) and (C-23). The centre electronegativity and plasma density are extracted directly from the simulation, while λ_i is estimated from the chemistry data using

$$\lambda_i = \frac{1}{\sum_j n_g \sigma_{j,O_2^+}} \tag{C-24}$$

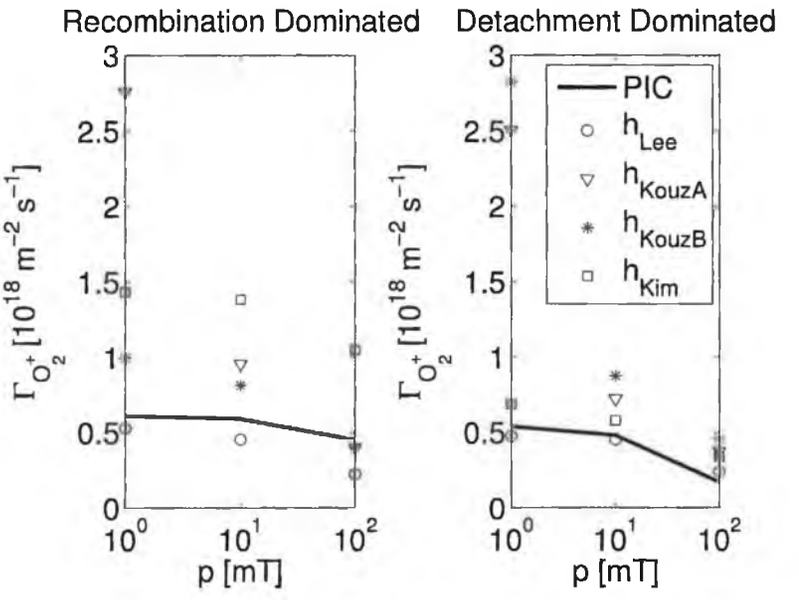

Figure C-1: *Graph comparing the positive ion wall fluxes obtained from the O_2 PIC simulations with fluxes estimated using equations (C-8), (C-10) and (C-23) and the values in table C-1.*

The relevant data is shown in table C-1.

Somewhat surprisingly, the original expression derived by Lee *et al* in 1994 appears to perform well over the extended parameter space. This result, however, is misleading.

As stated earlier, Lee's result was derived under the assumption of very low electronegativity. Our recombination-dominated simulations clearly do not correspond to this limit. However, the resulting error beguilingly produces the perceived model efficacy[c].

The, significantly more complex, formulation of Kouznetsov *et al* produces reasonable estimates at higher pressure, but significantly overestimates $\Gamma_{O_2^+}$ at low pressure. This is not surprising, as Kouznetzov's expres-

[c]Note the $2\alpha_0/\gamma_+$ term in equations (C-8) and (C-9). This term, which originates from the assumption $\alpha_0 \ll 1$, constitutes a significant perturbation in the highly electronegative recombination-dominated simulations.

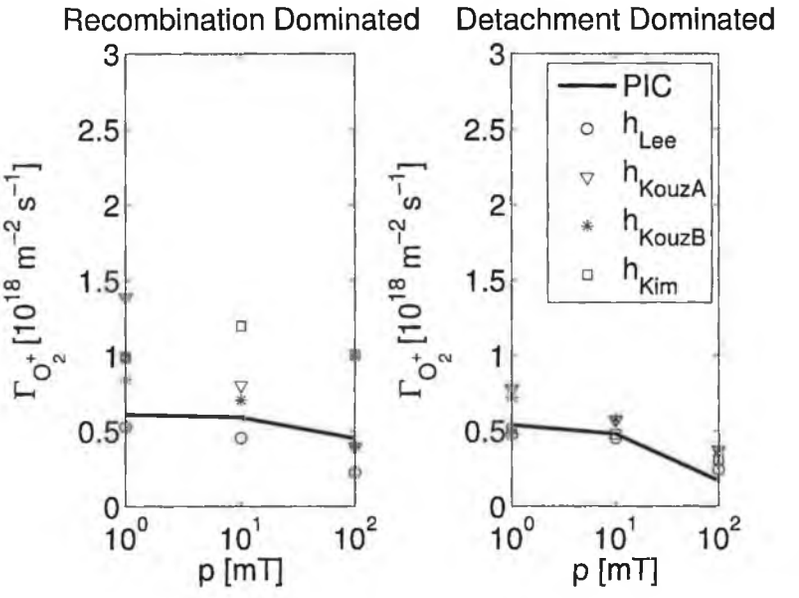

Figure C-2: *Graph comparing the positive ion wall fluxes obtained from the O_2 PIC simulations with fluxes estimated using equations (C-8), (C-10) and (C-23) and the common assumption $\gamma_- \approx \gamma_+ \approx \gamma_g$.*

sion was derived in the limit of diffusion-dominated ion dynamics, and is not matched to the low pressure Langmuir limit.

It should also be noted that Kouznetsovs' expression is quite sensitive to the value of the EEDF parameter x, due to the dependence of ν_{iz} on x (see table C-1). Failing to account for change in a with the parameter x, causes h_l to be significantly overestimated in the limit of high pressure (where $h_l \rightarrow a^{1/3}$).

Finally, the most recently published approximation for h_l, that of Kim *et al*, is seen to produce a satisfactory level of agreement in the detachment-dominated limit. However, the model appears to consistently overestimate the ion wall flux, most notably in the highly electronegative limit of the recombination-dominated simulations. This is feature is also not so surprising when one recalls that Kim's formulation does not incorporate the region

p mT	n_{e0} 10^{15} m^{-3}	α_0	γ_+ 10^{-3}	γ_- 10^{-3}	T_e eV	x	l_p/λ_i	ν_{iz} 10^5 s^{-1}
1	0.25	7.2	3.1	11.6	7.01	1.00	0.805	1.17 (1.17)
10	0.45	17.2	7.4	11.5	3.23	1.00	8.050	0.64 (0.64)
100	0.47	49.9	7.5	8.7	3.21	1.45	80.500	2.09 (6.26)
1	0.28	0.61	4.5	93.7	4.91	1.00	0.809	0.83 (0.83)
10	0.63	0.38	8.8	141.2	2.62	1.07	8.090	0.49 (0.61)
100	1.04	0.23	9.8	213.1	2.44	1.86	80.900	0.23 (4.13)

Table C-1: *Values extracted from the simulations and used in the calculations in this section. The values in the brackets correspond to the values ν_{iz} obtained assuming a Maxwellian distribution.*

of parameter space in which ion shock fronts are formed.

Note that in figure C-1 we have used the values of γ_+ and γ_- extracted from the simulation and shown in table C-1. In figure C-2 we present the same data only instead utilizing the common assumption $\gamma_- \approx \gamma_+ \approx \gamma_g$.

Ansatz Formulation

Implicit in the linear ansatz proposed by Kim *et al.* is the assumption that the three approximations for h_l fall-off/build-up in the transitional regions of parameter space, in such a way as their sum remains a reasonable estimate of the actual value. In our recombination-dominated simulations, it appears as though this, unfounded, assumption fails. The following, more general ansatz has therefore been proposed [139]

$$h_l \approx (h_a^x + h_b^x + h_c^x)^{1/x} \tag{C-25}$$

where x is a value ≥ 1. For $x > 1$, this ansatz ascribes greater weight to the largest approximation of h. Figures C-1 and C-3 suggest a value for x greater than 1. Considering integer values only, the terse investigation in figure C-4

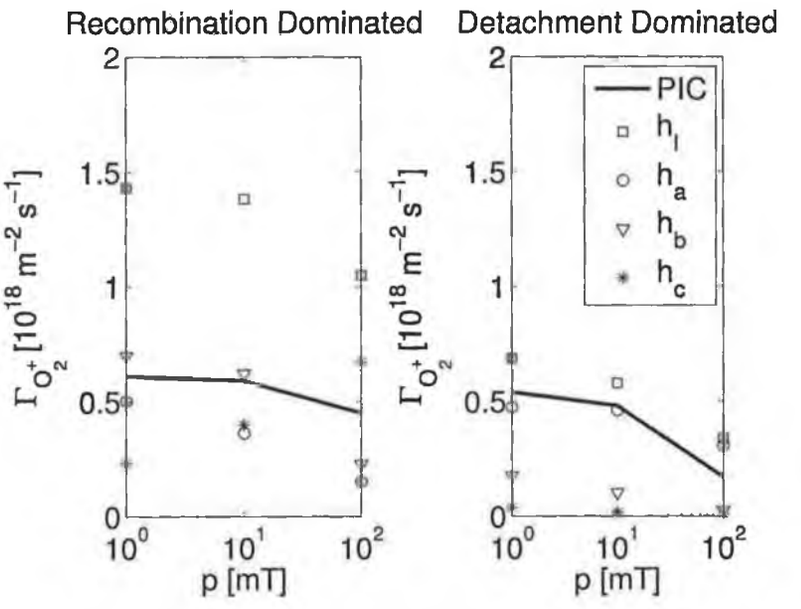

Figure C-3: *Linear ansatz of Kim* et al *[45].*

indicates that a value of $x \approx 2$ represents a reasonable compromise between qualitative and quantitative model-simulation agreement.

Note: $h_a(T_-)$

Finally, we have thus far neglected to mention that, in order to attain a reasonable level of model simulation agreement, we have been forced to set $\eta \approx 1$ in equation (C-18). Figure C-5 shows the results obtained without this modification.

Curiously, (C-18) implies that, in the limit of medium to high pressures and very low electronegativity ($\alpha_0 \to 0$), a negligible density of negative ions may continue to have a significant effect on the discharge dynamics if $T_- \gg T_+$.

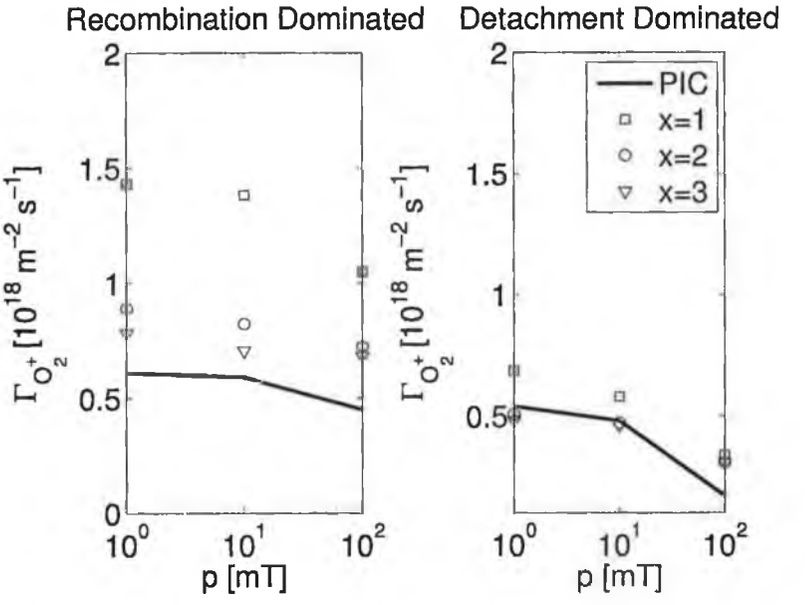

Figure C-4: *Investigation of a more general ansatz having the form of (C-25).*

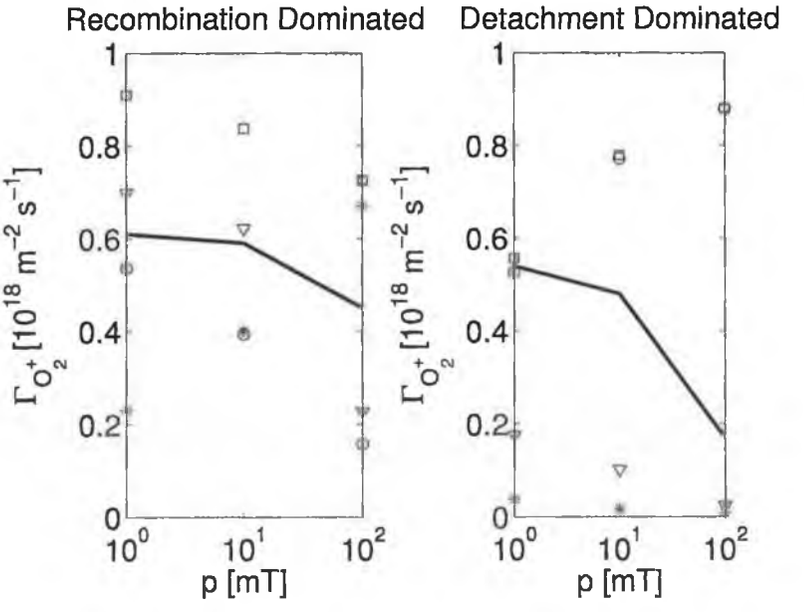

Figure C-5: *Kim ansatz with $x = 2$ and $\eta \neq 1$ in (C-18).*

Appendix D

Scaling With EEDF Parameter x

A simple low-pressure Ar global model, which may be solved analytically for T_e and n_{e0}, is constructed in [23] (section 10.2). In this appendix we shall extend this model by examining its scaling with the EEDF parameter x. The resulting expressions for T_e and n_{e0} are, respectively,:

$$\frac{K_{iz}(T_e, \mathrm{x})}{u_B(T_e, \mathrm{x})} = \frac{2A_{eff}}{n_g \pi R^2 L} \tag{D-1}$$

$$n_{e0}(T_e, \mathrm{x}) = \frac{P_{abs}}{e u_B(T_e, \mathrm{x}) A_{eff} \mathcal{E}_T(T_e, \mathrm{x})} \tag{D-2}$$

where $\mathcal{E}_T$ is the total energy lost per electron-ion pair recombining at the walls, and is given by:

$$\mathcal{E}_T = \mathcal{E}_c + \mathcal{E}_{ie} \tag{D-3}$$

where

$$K_{iz}\mathcal{E}_c \approx K_{iz}\mathcal{E}_{iz} + K_*\mathcal{E}_* + K_{**}\mathcal{E}_{**} + K_{el}\delta_{ei}k_B T_e \tag{D-4}$$

$K_{iz}(T_e, \mathrm{x})$ Scaling

Bearing in mind the observation in section 5.3.2, that the global model scaling with x appears to be dominated by it's effect on the reaction rate coefficients, we shall first endeavor to establish a general appreciation for the scaling of the rate coefficient $K_{iz}(T_e, \mathrm{x})$, where:

$$K_{iz}(Te, \mathrm{x}) = \int_{\mathcal{E}_{iz}}^{\infty} \sigma(\mathcal{E}) v(\mathcal{E}) f(\mathcal{E}; T_e, \mathrm{x}) d\mathcal{E} \tag{D-5}$$

Figure D-1 shows how $f(\mathcal{E}; T_e, \mathrm{x})$ varies with x. We see that for given values of T_e and x (> 1) there exists a lower bounded domain, $\{\mathcal{E}_{crit}(T_e, \mathrm{x}), \infty\}$ in energy space, defined by $f(\mathcal{E}; T_e, \mathrm{x} > 1) < f(\mathcal{E}; T_e, \mathrm{x} = 1)\ \forall \mathcal{E} > \mathcal{E}_{crit}(T_e, \mathrm{x})$. If $\mathcal{E}_{crit}(T_e, \mathrm{x}) < \mathcal{E}_{iz}$ the following inequality must therefore be satisfied:

$$K_{iz}(T_e, \mathrm{x} > 1) < K_{iz}(T_e, \mathrm{x} = 1) \tag{D-6}$$

regardless of the shape of the function $\sigma(\epsilon)$. It can be shown that $\mathcal{E}_{crit}(T_e, \mathrm{x}) = g(\mathrm{x})T_e$, where $g(\mathrm{x})$ is some function of x only[d]. Therefore, if $T_e < \mathcal{E}_{iz}/g(\mathrm{x})$ the above inequality most be satisfied. For $\mathrm{x} \gtrsim 1.1$, $g(\mathrm{x}) \approx 3$.

As T_e begins to exceed $\mathcal{E}_{iz}/g(\mathrm{x})$ one may reasonably expect the inequality (D-6) to continue to be satisfied (though it will no longer be a mathematical certainty). For most physically reasonable cross sections[e] and temperatures, $v(\mathcal{E})f(\mathcal{E}; T_e, \mathrm{x})$ will exceed $v(\mathcal{E})f(\mathcal{E}; T_e; 1)$ over most of the domain where $\sigma_{iz}(\mathcal{E})$ is an increasing / approximately-constant (slowly decreasing) function of $\mathcal{E}$. $K_{iz}(T_e, x > 1)$ will therefore continue to exceed $K_{iz}(T_e, x = 1)$ until one approaches relatively large values of T_e.

Moreover, the same arguments apply to any two values of x, x_1 and x_2, where $\mathrm{x}_2 > \mathrm{x}_1 > 1$, giving

$$K_{iz}(T_e, \mathrm{x}_2) < K_{iz}(T_e, \mathrm{x}_1) \tag{D-7}$$

and so, we conclude that $K_{iz}(T_e, \mathrm{x})$ is a decreasing function of x for physically

[d]To prove this, one must construct a relationship between two energy distributions having the same arbitrary value of x but having different values of T_e, T_{e1} and T_{e2}. This relationship has been found to be $f(\mathcal{E}; T_{e1}, \mathrm{x}) = \beta f(\beta\mathcal{E}; T_{e2}, x)$, where $\beta = T_{e2}/T_{e1}$. The two distributions are, therefore, related by a vertical (first β) and horizontal (second β) stretching/compressing which is directly proportional to β and independent of x. Thus, two distributions having different x will scale identically with change in T_e and the relationship between T_e and they're points of intersection will remain fixed.

[e]Typically, $\sigma_{iz}(\mathcal{E})$ increases over an extended region starting from 0 at $\mathcal{E} = \mathcal{E}_{iz}$, after which it peaks and finally decreases slowly with an approximate $\ln(\mathcal{E})/\mathcal{E}$ dependence [23].

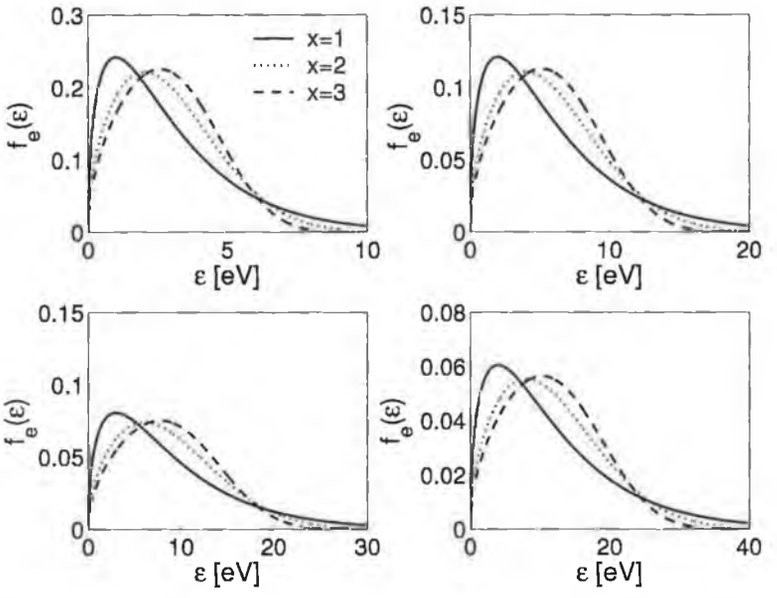

Figure D-1: *Variation of the energy distribution function defined by equation (5.3) with x and T_e. Note that the second point of intersection between these curves is approximately independent of x, and above this point $f_e(\mathcal{E};T_e,1) > f_e(\mathcal{E};T_e,2) > f_e(\mathcal{E};T_e,3)$.* **Top-left:** $T_e = 2eV$; **Top-right:** $T_e = 4eV$; **Bottom-left:** $T_e = 6eV$; **Bottom-right:** $T_e = 8eV$.

reasonable values of T_e.

Note that, in an argon discharge all ground state excitations have a relatively large threshold energy and so the same arguments may be applied to infer a similar scaling of $K_*(T_e, \mathrm{x})$ and $K_{**}(T_e, \mathrm{x})$ with x (but with a lower hypothesized limiting value of T_e). For reactions having small (relative to T_e) or zero threshold energies (such as K_{el}) these arguments are no longer valid[f].

Observed Scaling

Using the electron neutral cross section data referenced in table 3.1 (and illustrated in figure D-2), we may examine in more detail the scaling of

[f]Corresponding the limit of large T_e.

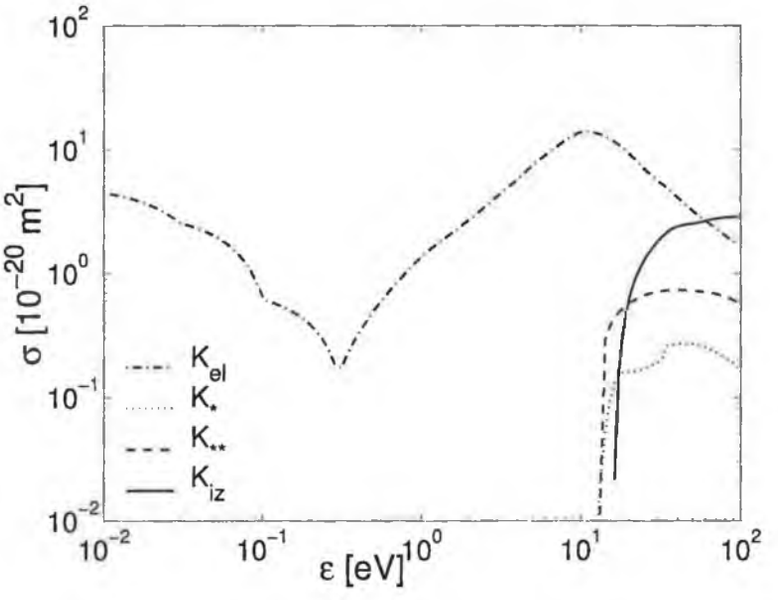

Figure D-2: *Electron-neutral cross sections referenced in table 3.1 for an argon discharge.*

the x dependent parameters in equations (D-1) and (D-2). These scalings are depicted in figures D-3, D-4 and D-5.

As predicted, we see that $K_{iz}(T_e, \mathrm{x})$, $K_*(T_e, \mathrm{x})$, and $K_{**}(T_e, \mathrm{x})$ are all decreasing functions x. The rate at which these reaction rate coefficients decrease scales inversely with T_e and is approximately exponential in x.

It is clear from equations (5.8) and (5.10) that the relative change in the Bohm velocity, u_B, and the electron temperature coefficient in the expression for $\mathcal{E}_{ie}$ are independent of T_e. Surprisingly, however, the relative change in the value of the sheath voltage, V_s, with x (given by equation (5.9)) also appears to be independent of T_e. This leads to the scaling depicted in figure D-4.

Finally, the scaling of the combined parameters $K_{iz}(T_e, \mathrm{x})/u_B(T_e, \mathrm{x})$ and $u_B(T_e, \mathrm{x})\mathcal{E}_T(T_e, \mathrm{x})$ are shown in figure D-5. We see that the first of

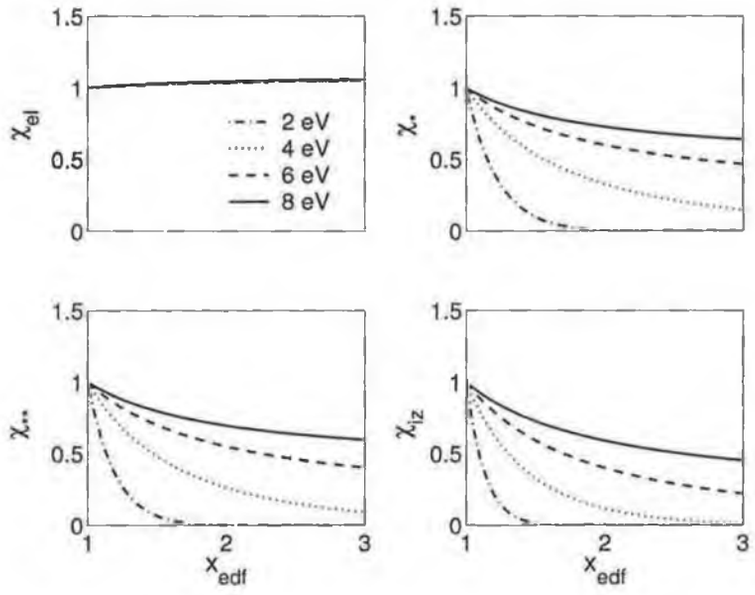

Figure D-3: *Relative variation in reaction rate constants with T_e and x where $\chi_a(T_e, x) \equiv K_a(T_e, x)/K_a(T_e, x = 1)$.*

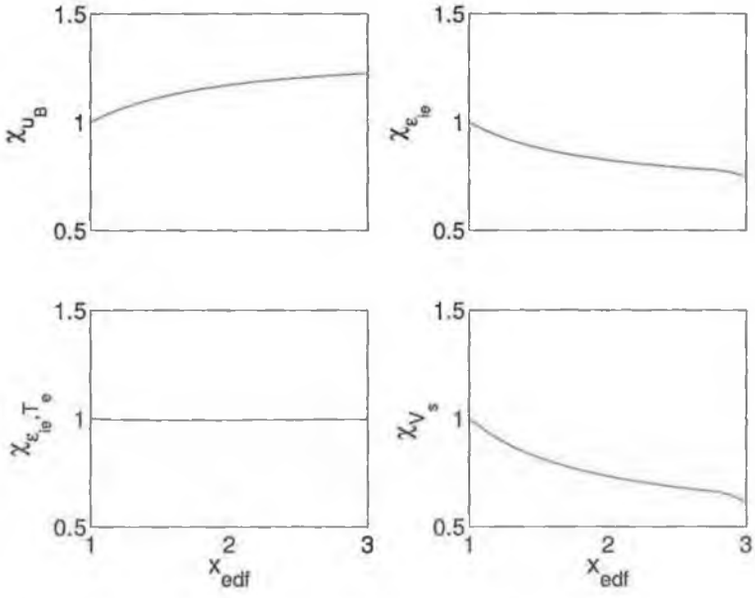

Figure D-4: *Relative variation in additional parameters of interest with T_e and x where χ has been defined in figure D-3. Note, $\mathcal{E}_{ie}, T_e$ indicates the x dependent T_e coefficient in equation 5.10.*

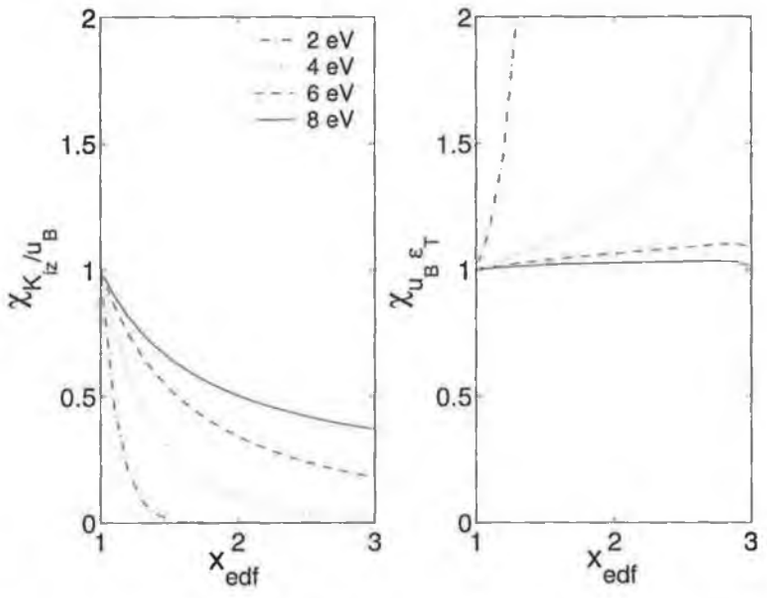

Figure D-5: *Relative variation the lhs of equation (D-1) and the denominator in equation (D-2).*

these, $K_{iz}(T_e, \mathrm{x})/u_B(T_e, \mathrm{x})$, is an increasing function of T_e and a decreasing function of x. Thus, for a given geometry and pressure, T_e will be an increasing function of x, increasing more rapidly at lower values of T_e.

In contrast, the denominator on the rhs of equation (D-2) is found to be an exponentially increasing function x at low values of T_e and approximately constant at larger values. This can be understood by examining equations (D-3), (D-4) and the scaling in figures D-3 and D-4. At very low values of T_e, $\mathcal{E}_c$ may be approximated by:

$$\mathcal{E}_c \sim \frac{K_{el}(T_e, \mathrm{x})}{K_{iz}(T_e, \mathrm{x})} \delta_{ei} k_B T_e \tag{D-8}$$

where $K_{el}(T_e, \mathrm{x}) \gg K_{iz}(T_e, \mathrm{x})$, and $K_{iz}(T_e, \mathrm{x})$ is an exponentially decreasing function of x. The expression for $\mathcal{E}_T$ is dominated by $\mathcal{E}_c$ in this regime, and is therefore a sensitive (exponentially increasing) function of x. As T_e is

increased, $K_{el}(T_e, \mathrm{x})$ remains approximately constant, $K_{iz}(T_e, \mathrm{x})$ increases exponentially and becomes less sensitive to x, while $\mathcal{E}_{ie}$ increases linearly. At very large values of T_e, therefore, the rhs of (D-3) is dominated by $\mathcal{E}_{ie}$, and $\mathcal{E}_T$ decreases with x. This decrease will be offset by the similar rate of increase of $u_B(T_e, \mathrm{x})$ with x and so the denominator in (D-2) becomes approximately independent of the parameter x.

We conclude, therefore, that for a given geometry, pressure and value of P_{abs}, moving from from a Maxwellian EEDF toward a Druyvesteyn-like EEDF will increase T_e and decrease n_{e0}. The relative change in these parameters will be greatest at lower electron temperatures (higher pressures), with n_{e0} becoming particularly sensitive to the EEDF parameter x in this regime.

Appendix E

The Mobility-Limited Bohm Criterion

Equation (1.51) may be rewritten with an equality in place of the inequality to give the following expression for the ion Bohm speeds in a multi-ion electropositive plasma

$$\sum_{j}^{N_p} \frac{z_j^2 n_{js}}{m_j u_{js}^2} = \frac{n_{es}}{k_B T_{es}} \tag{E-1}$$

where N_p is the total number of positive ions in the discharge, z_j is the ion charge number, and s denotes the quasi-neutral plasma edge. It has been assumed that $m_j u_{js}^2 \gg k_B T_j \ \forall j$ (which limits (E-1) to electropositive discharges only).

This equation may be solved for the individual ion Bohm speeds, u_{is}, yielding the following implicit expression

$$u_{is}^2 = \frac{k_B T_{es}}{m_i} \frac{z_i^2 n_{is} + \sum_{j,j\neq i}^{N_p} z_j^2 n_{js} \frac{m_i u_{is}^2}{m_j u_{js}^2}}{\sum_{j}^{N_p} n_j} \tag{E-2}$$

When $\mu_e \gg \mu_i$ and $T_e \gg T_i$, the pressure gradient term in the mobility diffusion equation is small compared to the mobility term. The motion therefore becomes "mobility-limited" and the ion velocities may be approximated as follows [23]

$$u_i \approx \mu_i E \tag{E-3}$$

Equation (E-2) may therefore be expressed explicitly in this limit, yielding

$$
\begin{aligned}
u_{is}'^2 &\approx \frac{z_i^2 n_{is} + \sum_{j,j\neq i}^{N_p} z_j^2 n_{js} \frac{m_i}{m_j} \frac{\mu_i^2}{\mu_j^2}}{\sum_j^{N_p} n_j} \\
&= \frac{z_i^2 n_{is} + \sum_{j,j\neq i}^{N_p} z_j^2 n_{js} \frac{z_i}{z_j} \frac{m_j}{m_i} \frac{\nu_{m,j}^2}{\nu_{m,i}^2}}{\sum_j^{N_p} n_j}
\end{aligned}
\tag{E-4}
$$

This expression is valid at pressures where the ion thermal velocity determines the time between collisions and a constant-mobility may be assumed. At lower pressures it is the ion drift velocity, and not the ion thermal velocity, which characterizes the the ion-neutral collisions, and so we must utilize the variable-mobility approximation [23]

$$
\mu_i \approx \frac{2ez_i\lambda_i}{\pi m_i |\boldsymbol{u_i}|} \tag{E-5}
$$

giving the one-dimensional scalar relation

$$
u_i^2 \approx \frac{2ez_i\lambda_i}{\pi m_i} E \tag{E-6}
$$

where $\boldsymbol{u_i} \parallel \boldsymbol{E}$ is assumed. Now, substituting (E-6) into (E-2) gives the following explicit expression the normalized ion velocities satisfying the Bohm criterion

$$u_{is}'^2 \approx \frac{z_i^2 n_{is} + \sum_{j,j\neq i}^{N_p} z_j^2 n_{js} \frac{z_i}{z_j}\frac{\lambda_i}{\lambda_j}}{\sum_j^{N_p} n_j} \tag{E-7}$$

Note the particularly elegant form (E-7) attains in the commonly encountered case of a plasma containing two singly-charged positive ions

$$u_{1s}'^2 = \frac{n_{1s} + n_{2s}\frac{\lambda_1}{\lambda_2}}{n_{1s} + n_{2s}} \tag{E-8}$$

$$u_{2s}'^2 = \frac{n_{1s}\frac{\lambda_2}{\lambda_1} + n_{2s}}{n_{1s} + n_{2s}} \tag{E-9}$$

We may extend this analysis to electronegative plasmas having N_n negative ions in thermal equilibrium with the electric field by simply modifying the rhs of equation (E-1) as follows

$$\sum_j^{N_p} \frac{z_j^2 n_{js}}{m_j u_{js}^2} = \frac{nes}{k_B T_{es}}\left(1 + \sum_k^{N_n} \gamma_{ks}\alpha_{ns}\right) \tag{E-10}$$

where $\gamma_{ks} = k_B T_{es}/k_B T_{ks}$ and $\alpha_{ns} = n_{ns}/n_{es}$. Thus, one need only replace the summation in the denominator of (E-2), (E-4) and (E-7) with

$$n_{es}\left(1 + \sum_k^{N_n} \gamma_{ks}\alpha_{ks}\right) \tag{E-11}$$

Comparison with Simulation

The multi-ion plasmas investigated in this work are, by design, electronegative. However, field penetration at the sheath edge insures that the negative ion densities are negligible at the plasma-sheath interface. We may therefore use these simulations to investigate the validity of (E-7). Figures

E-1, E-2, E-3, E-4, E-5 and E-6 constitute this investigation with u_i' and u_i'' denoting the normalized velocities

$$u_i'(x) \equiv u_i(x)\sqrt{\frac{m_i}{k_B T_e(x)}} \tag{E-12}$$

and

$$u_i''(x) = u_i'(x)\left[\frac{z_i^2 n_i(x) + \sum_{j,j\neq i}^{N_p} z_j^2 n_j(x)\frac{z_i}{z_j}\frac{\lambda_i}{\lambda_j}}{\sum_j^{N_p} n_j(x)}\right]^{-1} \tag{E-13}$$

where all variables (with the exception of λ_i are extracted directly from the simulations.

At very low pressures (1 mT), we see that $u'_{Ar^+}(x)$ and $u'_{O_2^+}(x)$ both approach unity at approximately the same point. Thus, as predicted, each ion attains it's individual sound speed at a single point, where the Bohm criterion is satisfied. However, we see that as pressure increases this solution becomes a poor approximation. Instead, it is the values of u_i'' which begin to approach one close to the same point.

It should be noted that λ_{Ar} and, to a lesser extent, λ_{O_2} are poorly estimated in the limit of high O_2 and high Ar gas fractions, respectively. This is due to the fact that cross-section data is not provided for the $Ar^+ - O_2$ and $O_2^+ - Ar$ collisions (see table 3.3). Instead σ (which is used to estimate λ_i) must be estimated from the value of the rate constant. It is the minority ion which is most sensitive to errors in the value of λ_i.

Transitional Approximation

In between the collisionless and mobility-limited regimes the ion velocity may be obtained by solving the following differential equation

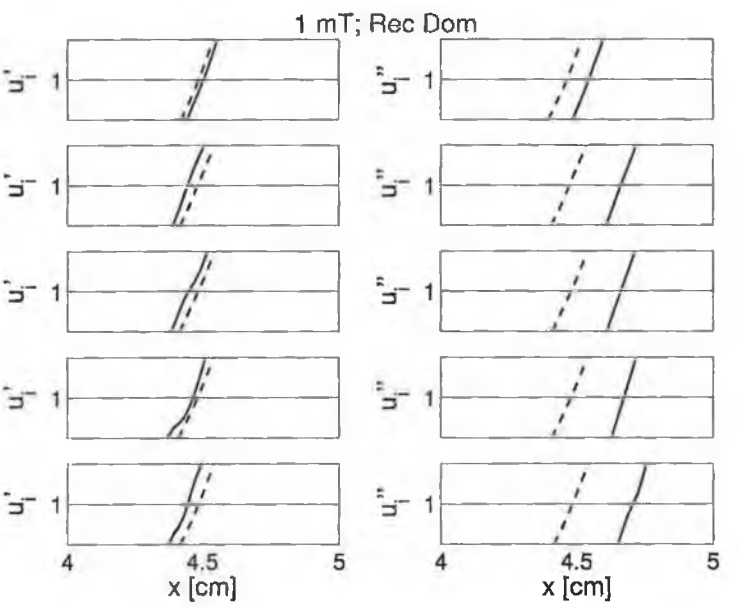

Figure E-1: *Normalized ion velocities obtained from the Ar/O_2 PIC simulations.* **Top-to-Bottom**: *n_{Ar}/n_{O_2} =, 0.01, 0.02, 0.05, 0.11 , 1.0.* **Left**: *$u_i'(x)$;* **Right**: *$u_i''(x)$. The solid blue line corresponds to the O_2^+ ion, while the dashed green line corresponds to the Ar^+ ion. When both velocities approach 1 at the same point, they correspond to a valid solution of the multiple-ion Bohm criterion.*

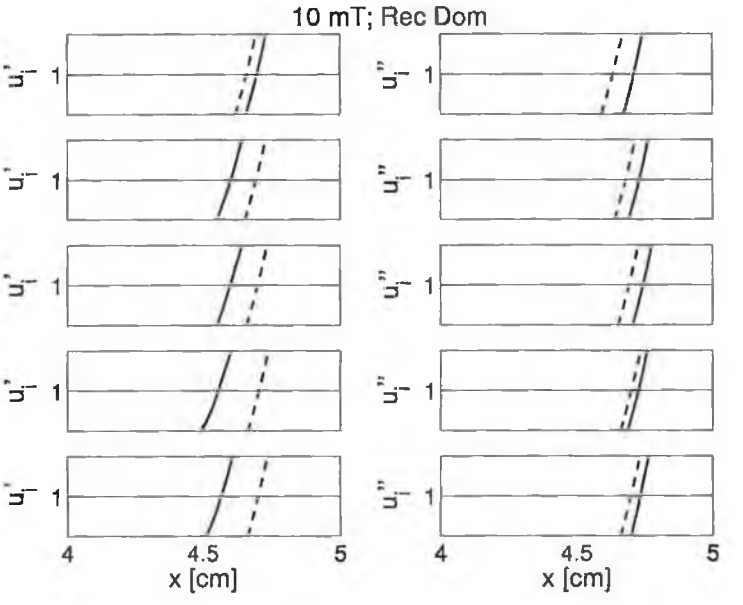

Figure E-2: *Normalized ion velocities obtained from the Ar/O_2 PIC simulations. See figure E-1.*

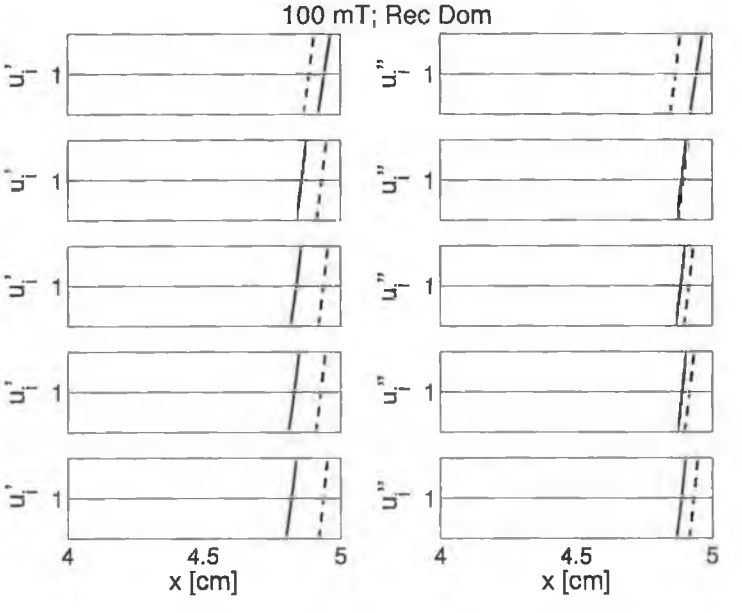

Figure E-3: *Normalized ion velocities obtained from the Ar/O_2 PIC simulations. See figure E-1.*

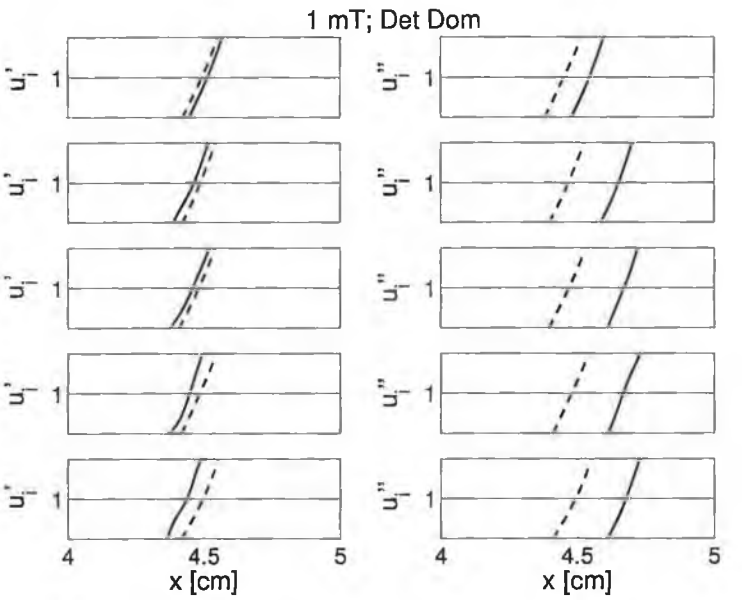

Figure E-4: *Normalized ion velocities obtained from the $Ar/O_2/O_2(a^1\Delta_g)$ PIC simulations. See figure E-1.*

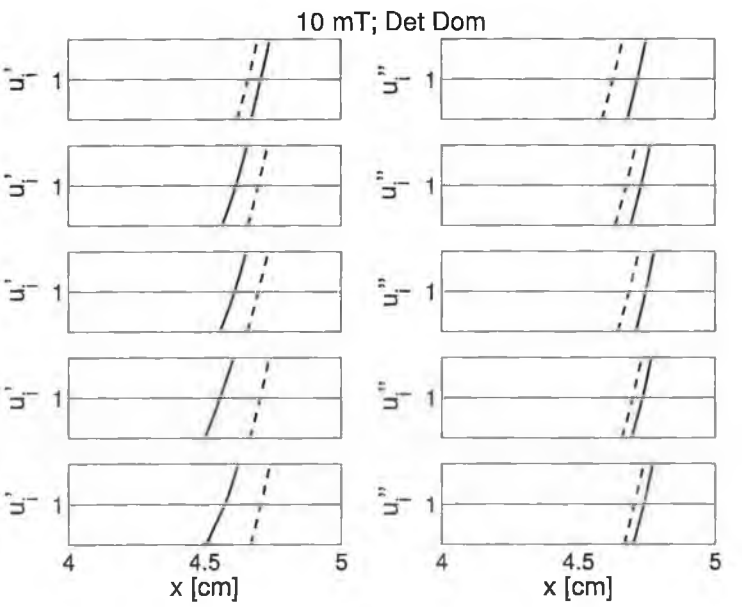

Figure E-5: *Normalized ion velocities obtained from the $Ar/O_2/O_2(a^1\Delta_g)$ PIC simulations. See figure E-1.*

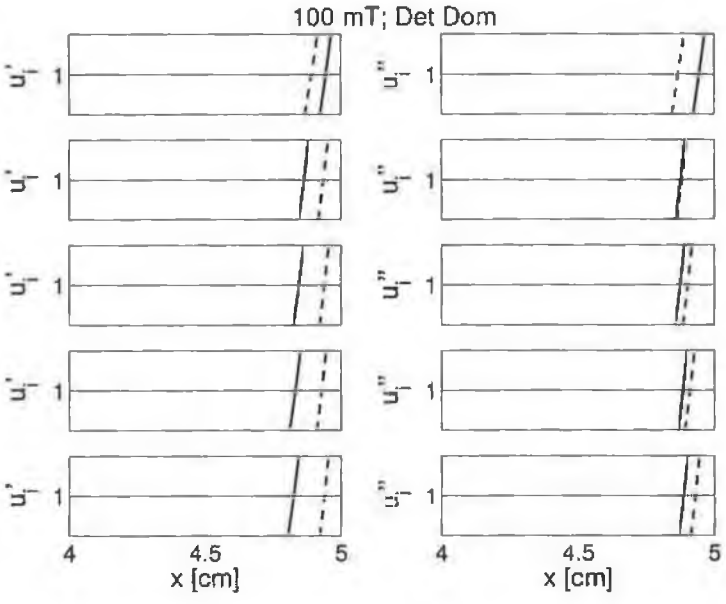

Figure E-6: *Normalized ion velocities obtained from the $Ar/O_2/O_2(a^1\Delta_g)$ PIC simulations. See figure E-1.*

$$\boldsymbol{u}_i \cdot \nabla \boldsymbol{u}_i = z_i e \boldsymbol{E} - mn\nu_{mi}\boldsymbol{u}_i \tag{E-14}$$

The non-linear nature of this equation (which must be coupled the the appropriate continuity and Boltzmann equations) prevents us from obtaining a simple analytical solution in the transitional regime. However, assuming a smooth transition, one may construct a simple empirical formula which approaches the the collisionless and mobility-limited solutions in the limits $\bar{\lambda}_i/l_p \gg 1$ and $\bar{\lambda}_i/l_p \ll 1$, respectively. We propose the following empirical modification to equation (E-7)

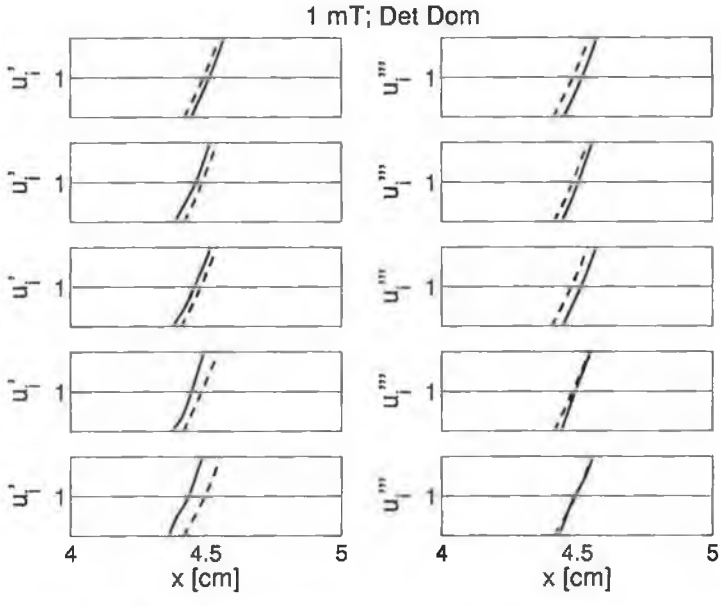

Figure E-7: *Normalized ion velocities obtained from the Ar/O_2 PIC simulations.* **Top-to-Bottom/ Left:** *Same as figure E-1.* **Right:** *ion velocity normalized to the empirical formulation given in equation E-15 with $\beta = 2$.*

$$u_{is}^{\prime 2} \approx \frac{z_i^2 n_{is} + \sum_{j,j\neq i}^{N_p} z_j^2 n_{js} \left[1 + \left(1 + \frac{\bar{\lambda}_i}{l_p}\right)^{-\beta} \left(\frac{z_i}{z_j}\frac{\lambda_i}{\lambda_j} - 1\right)\right]}{\sum_{j}^{N_p} n_j} \tag{E-15}$$

where $\bar{\lambda}_i = (\sum \lambda_i)/N_+$ and β is an arbitrary dimensionless fitting parameter. Our simulations suggest a choice of $\beta \approx 2$–3. This empirical approximation to the low-pressure Bohm criterion is examined (with $\beta = 2$) in figures E-7–E-12.

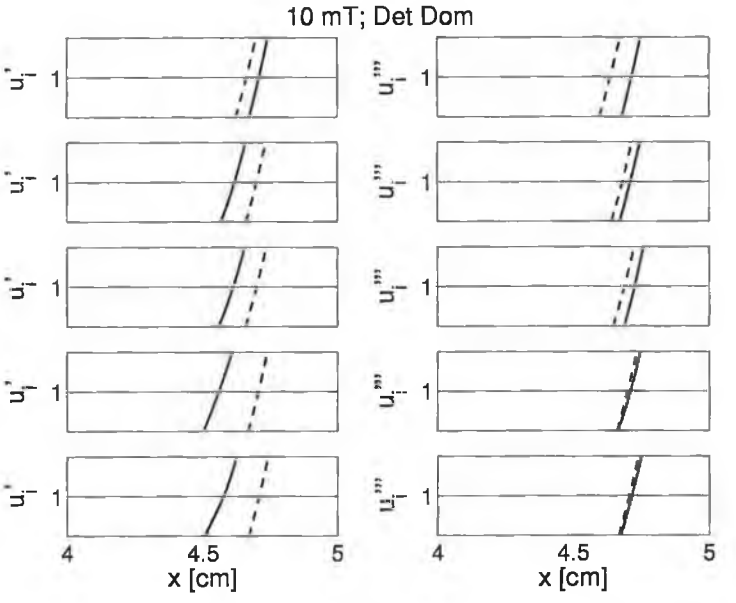

Figure E-8: *Normalized ion velocities obtained from the Ar/O_2 PIC simulations. See figure E-7.*

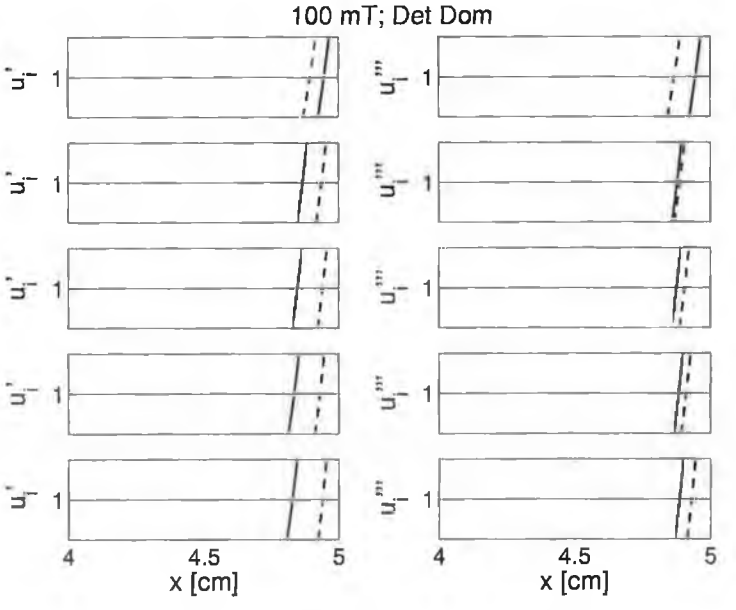

Figure E-9: *Normalized ion velocities obtained from the Ar/O_2 PIC simulations. See figure E-7.*

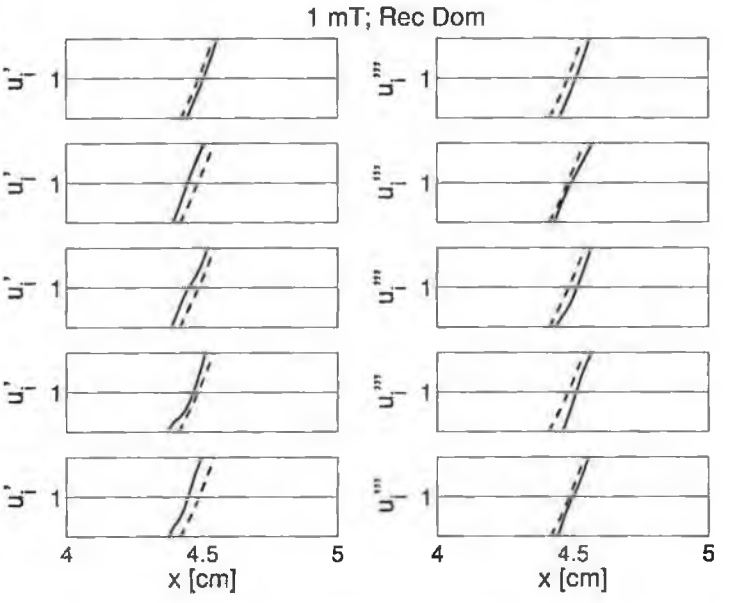

Figure E-10: *Normalized ion velocities obtained from the $Ar/O_2/O_2(a^1\Delta_g)$ PIC simulations. See figure E-7.*

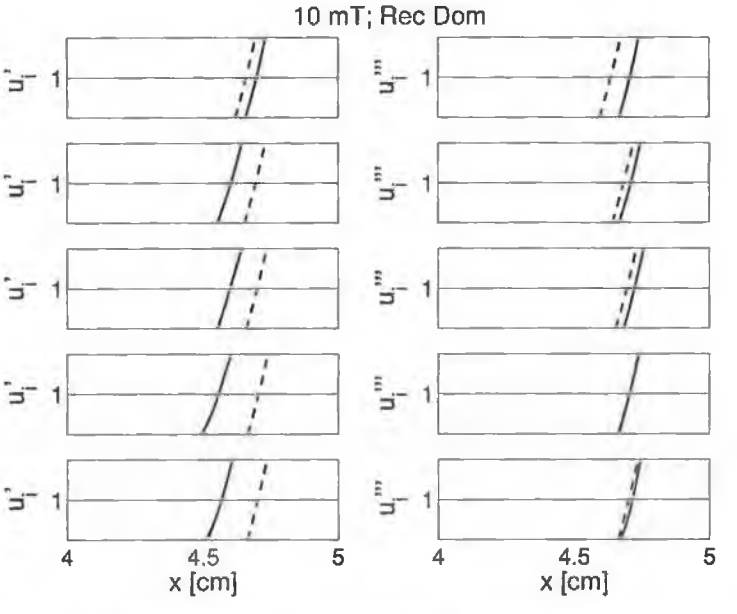

Figure E-11: *Normalized ion velocities obtained from the $Ar/O_2/O_2(a^1\Delta_g)$ PIC simulations. See figure E-7.*

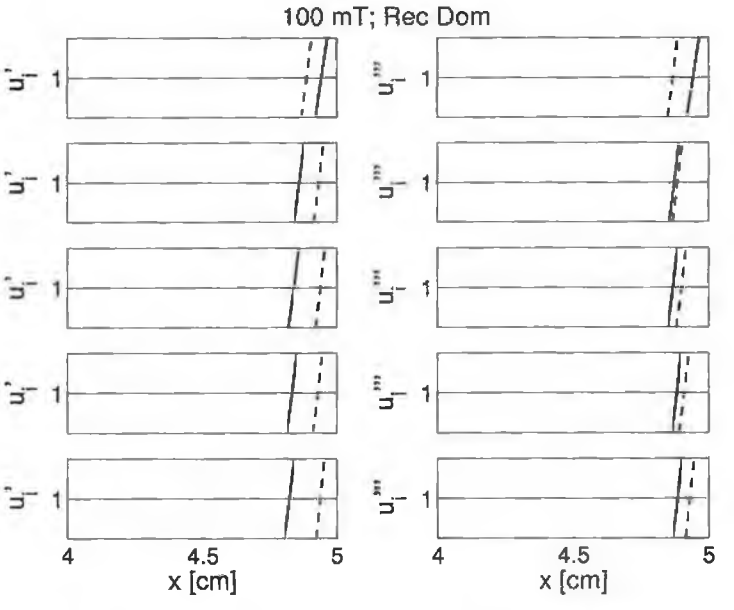

Figure E-12: *Normalized ion velocities obtained from the $Ar/O_2/O_2(a^1\Delta_g)$ PIC simulations. See figure E-7.*

Bibliography

[1] M. A. Lieberman and A. J. Lichtenberg, *Principles of Plasma Discharges and Materials Processing - 2nd Edition.* John Wiley & Sons, inc., 2005.

[2] L. Tonks and I. Langmuir, "A general theory of the plasma of an arc," *Phys. Rev.*, vol. 34, pp. 876–922, 1928.

[3] A. Fridman and L. A. Kennedy, eds., *Plasma Physics and Engineering.* Taylor & Francic, 2004.

[4] T. E. Sheridan, P. Chabert, and R. W. Boswell, "Positive ion flux from a low-pressure electronegative discharge," *Plas. Sourc. Sci. Technol.*, vol. 8, pp. 457–462, 1999.

[5] P. C. Stangeby and J. E. Allen, "Plasma boundary as a mach surface," *J. Phys. A: Gen. Phys*, vol. 3, pp. 304–308, 1970.

[6] F. F. Chen, ed., *Introduction to Plasma Physics and Controlled Fusion - Volume 1: Plasma Physics.* Plenum Press, New York, 1983.

[7] A. Kono, "Plasma-sheath transition and ion sound speed in weakly collisional plasmas," *Phys. of Plas.*, vol. 10, pp. 4181–4184, 2003.

[8] L. P. Block, "A double layer review," *Astrophys. and Space Sci.*, vol. 55, pp. 59–83, 1978.

[9] M. A. Raadu and J. J. Rasmussen, "Dynamical aspects of electrostatic double layers," *Astro. and Space Sci.*, vol. 144, pp. 43–71, 1987.

[10] H. Amemiya and G. Guchs, "Double sheath formed between two electronegative plasmas," *Plas. Sourc. Sci. Technol.*, vol. 13, pp. 213–222, 2004.

[11] S. Iizuka, K. Saeki, N. Sato, and Y. Hatta, "Buneman instability, pierce instability, and double-layer formation in a collisionless plasma," *Phys. Rev. Lett.*, vol. 43, pp. 1404–1407, 1979.

[12] P. Carlqvist, "On the physics of relativistic double layers," *Astro. and Space Sci.*, vol. 87, pp. 21–39, 1982.

[13] F. Verheest and M. A. Hellberg, "Bohm sheath criteria and double layers in multispecies plasmas," *J. Plasma Physics*, vol. 57, pp. 465–477, 1997.

[14] K. U. Riemann, "The bohm criterion and boundary conditions for a multicomponent system," *IEEE Trans. Plas. Sci.*, vol. 23, p. 709, 1995.

[15] J. F. McKenzie, "Stationary structures in multi-ion plasmas with differential streaming," *J. Plas. Phys.*, vol. 65, pp. 181–195, 2001.

[16] P. D. Edgley and A. von Engel, "Theory of positive columns in electronegative gases," *Proc. R. Soc. Lond. A*, vol. 370, pp. 375–387, 1980.

[17] R. L. F. Boyd and J. B. Thompson, "The operation of langmuir probes in electronegative plasmas," *Proc. Royal Soc. Lond. A*, vol. 252, pp. 102–119, 1959.

[18] K. G. Emeleus and G. A. Woolsey, eds., *Discharges in Electronegative Gases.* Taylor & Francis Ltd., 1970.

[19] J. B. Thompson, "Negative ions in the positive column of the oxygen discharge," *Proc. Phys. Soc.*, vol. 34, pp. 11–15, 1959.

[20] R. N. Franklin, "Electronegative plasmas – why are they so different," *Plasma Sources Sci. Technol.*, vol. 11, pp. A31–A37, 2002.

[21] M. Lampe, W. M. Manheimer, R. F. Fernsler, S. P. Slinker, and G. Joyce, "The physical and mathematical basis of stratification in electronegative plasmas," *Plas. Sourc. Sci. Technol.*, vol. 13, pp. 15–26, 2004.

[22] C. M. Ferreira, G. Gousset, and M. Touzeau, "Quasi-neutral theory of positive columns in electronegative gases," *J. Phys. D: Appl. Phys.*, vol. 21, pp. 1403–1413, 1988.

[23] M. A. Lieberman and A. J. Lichtenberg, *Principles of Plasma Discharges and Materials Processing.* John Wiley & Sons, inc., 1994.

[24] P. G. Daniels and R. N. Franklin, "The positive column in electronegative gases – a boundary layer approach," *J. Phys. D: Appl. Phys.*, vol. 22, pp. 780–785, 1989.

[25] P. G. Daniels, R. N. Franklin, and J. Snell, "The contracted positive column in electronegative gases," *J. Phys. D: Appl. Phys.*, vol. 23, pp. 823–831, 1990.

[26] N. S. J. Braithwaite and J. E. Allen, "Boundaries and probes in electronegative plasmas," *J. Phys. D: Appl.Phys.*, vol. 21, pp. 1733–1737, 1988.

[27] J. E. Allen, "A note on the bohm criterion for electronegative gases," *Plasma Sources Sci. Technol.*, vol. 13, pp. 48–49, 2004.

[28] J. P. Boeuf, "Numerical model of rf glow discharges," *Physical Review A*, vol. 36, pp. 2782–2792, 1987.

[29] D. B. Graves and F. J. Klavs, "A continuum model of dc and rf discharges," *IEEE Trans. Plas. Sci.*, vol. PS-14, pp. 78–91, 1986.

[30] Y. H. Oh, N. H. Choi, and D. I. Choi, "A numerical simulation of rf glow discharge containing an electronegative gas composition," *J. Appl .Phys*, vol. 67, p. 326, 1990.

[31] M. Meyyappan and T. R. Govindan, "Modeling of electronegative radio-frequency discharges," *IEEE Trans. Plas. Sci.*, vol. 19, pp. 122–129, 1991.

[32] A. J. Lichtenberg, Y. T. Kouznetsov, M. A. Lieberman, I. D. Kaganovich, and L. D. Tsendin, "Modelling plasma discharges at high electronegativity," *Plas. Sourc. Sci. Technol.*, vol. 6, pp. 437–449, 1997.

[33] R. N. Franklin and S. J, "The recombination-dominated positive column with finite ion temperature," *J. Phys. D: Appl. Phys.*, vol. 27, pp. 2102–2106, 1994.

[34] R. N. Franklin, D. P. G, and S. J, "Characteristics of electric discharges in the halogens: the recombination-dominated positive column," *J. Phys. D: Appl. Phys.*, vol. 26, pp. 1638–1649, 1993.

[35] J. A. Johnson III and R. Ramaiah, "Plasma instability in the presence of negative ions," *Phys. Rev. A*, vol. 36, pp. 774–794, 1987.

[36] R. N. Franklin and J. Snell, "The free fall column with negative ions," *J. Phys. D: Appl. Phys.*, vol. 25, pp. 453–457, 1992.

[37] V. A. Feokistov, V. V. Ivanov, A. M. Popov, A. T. Rakhimov, T. V. Rakhimov, D. I. Slovetsky, and V. N. Volynets, "The influence of anisotropy and non-locality of the electron distrubition function as well as non-equilibrium ion diffusion on the electrodynamics of CF_4 dc discharges at low pressure," *J. Phys. D: Appl. Phys.*, vol. 30, pp. 423–431, 1997.

[38] A. J. Lichtenberg, V. Vahedi, M. A. Lieberman, and T. Rognlien, "Modelling electronegative plasma discharges," *J. Appl. Phys.*, vol. 75, pp. 2339–2347, 1994.

[39] R. N. Franklin, "Ambipolar diffusion is a misnomer," *J. Phys. D: Appl. Phys.*, vol. 36, pp. 828–831, 2003.

[40] I. G. Kouznetsov, A. J. Lichtenberg, and M. A. Lieberman, "Modelling electronegative discharges at low pressure," *Plasma Sources Sci. Technol.*, vol. 5, pp. 662–676, 1996.

[41] C. Lee, D. B. Graves, M. A. Lieberman, and D. W. Hess, "Global model of plasma chemistry in a high density oxygen discharge," *J. Electrochem. Soc.*, vol. 141, pp. 1546–1555, 1994.

[42] M. A. Lieberman and R. A. Gottscho, *Chapter 1: Physics of Thin Films*, vol. 18. New York Academic Press, 1994.

[43] C. Lee and M. A. Lieberman, "Global model of Ar, O_2, Cl_2, and

Ar/O_2 high-density plasma discharges," *J. Vac. Sci. Technol. A*, vol. 13, pp. 368–380, 1995.

[44] V. A. Godyak and V. N. Maksimov, "Spatial distribution of a bounded plasma," *Fizika*, vol. 32, pp. 51–56, 1977.

[45] S. Kim, M. A. Lieberman, A. J. Lichtenberg, and J. T. Gudmundsson, "Improved volume-averaged model for steady and pulsed-power electronegative discharges," *J. Vac. Sci. Technol. A*, vol. 24, pp. 2025–2040, 2006.

[46] S. Kim, *An Improved Global Model for Electronegative Discharge and Ignition Conditions for Peripheral Plasma Connected to a Capacitive Discharge.* PhD thesis, University of California at Berkeley, 2006. http://www.eecs.berkeley.edu/Pubs/TechRpts/2006/EECS-2006-56.html.

[47] J. T. Gudmundsson and M. A. Lieberman, "Model and measurements for a planar inductive oxygen discharge," *Plas. Sourc. Sci. Technol.*, vol. 7, pp. 1–12, 1998.

[48] T. Kimura and K. Ohe, "Probe measurements and global model of inductively coupled Ar/CF_4 discharges," *Plas. Sourc. Sci. Technol.*, vol. 8, pp. 553 -560, 1999.

[49] T. Kimura and M. Noto, "Experimental study and global model of inductively coupled CF_4/O_2 discharges," *J. Appl. Phys.*, vol. 100, p. 063303, 2006.

[50] G. L. Rogoff, "Ambiploar diffusion coefficients for discharges in attaching gases," *J. Phys. D: Appl. Phys.*, vol. 18, pp. 1533–1545, 1985.

[51] V. N. Volynets, A. V. Lukyanova, A. T. Rakhimov, D. I. Slovetsky, and N. V. Suetin, "Experimental and theoretical study of the cf_4 dc glow discharge positive column," *J. Phys. D: Appl. Phys.*, vol. 26, pp. 647–656, 1993.

[52] R. N. Franklin and J. Snell, "Modelling discharges in electronegative gases," *J. Phys. D: Appl. Phys.*, vol. 32, pp. 2190–2203, 1999.

[53] R. N. Franklin and J. Snell, "The boltzmann relation in electronegative plasmas: When is it permissible to use it?," *J. Plas. Phys.*, vol. 64, pp. 131–153, 2000.

[54] R. N. Franklin, "A critique of models of electronegative plasmas," *Plas. Sourc. Sci. Technol.*, vol. 10, pp. 162–167, 2001.

[55] R. N. Franklin and S. J, "The low-pressure positive column in electronegative gases including space charge-matching plasma and sheath," *J. Phys. D: Appl. Phys.*, vol. 31, pp. 2532–2542, 1998.

[56] R. N. Franklin, "The fluid model of the positive column of a discharge with negative ions at low pressure joining plasma and sheath," *J. Phys. D: Appl. Phys.*, vol. 32, pp. L71–L74, 1999.

[57] R. N. Franklin and J. Snell, "The positive column with negative ions in a magnetic field at low pressure," *J. Phys. D: Appl. Phys.*, vol. 32, pp. 1031–1038, 1999.

[58] R. N. Franklin, "The plasma-wall boundary region in negative-ion-dominated plasmas at low pressure," *J. Phys. D: Appl. Phys*, vol. 9, pp. 191–198, 2000.

[59] R. N. Franklin, "Fluid model of the collisional positive column in electronegative gases: Transition from detachment dominated to recom-

bination dominated," *J. Phys. D: Appl. Phys*, vol. 33, pp. 2019–2024, 2000.

[60] R. N. Franklin and J. Snell, "Are the oscillations found in electronegative plasmas at low pressure an artefact," *J. Phys. D: Appl. Phys*, vol. 33, pp. 1990–1995, 2000.

[61] R. N. Franklin, "Modelling the electron temperature characteristic for discharges in electronegative recombination dominated gases," *J. Phys. D: Appl. Phys.*, vol. 34, pp. 1243–1247, 2001.

[62] R. N. Franklin, "The role of $O_2(a^1\Delta_g)$ metastables and associateive detachment in discharges in oxygen," *J. Phys. D: Appl. Phys.*, vol. 34, pp. 1834–1839, 2001.

[63] R. N. Franklin, "A comprehensive treatment of the positive column of discharges in electronegative gases," *Proc. R. Soc. Lond. A*, vol. 547, pp. 307–330, 2001.

[64] A. J. Lichtenberg, M. A. Lieberman, I. G. Kouznetsov, and T. H. Chung, "Transitions and scaling laws for electronegative discharge models," *Plas. Sourc. Sci. Technol.*, vol. 9, pp. 45–56, 2000.

[65] I. D. Kaganovich, D. J. Economou, B. N. Ramamurhi, and V. Midha, "Negative ion density fronts during ignition and extinction of plasmas in electgronegative gases," *Phys. Rev. Lett.*, vol. 84, pp. 1918–1921, 2000.

[66] I. D. Kaganovich, "Negative ion density fronts," *Phys. of Plas.*, vol. 8, pp. 2540–2548, 2001.

[67] T. Takeuchi, S. Iizuka, and N. Sato, "Ion acoustic shocks formed in

a collisionless plasma with negative ions," *Phys. Rev. Lett.*, vol. 80, pp. 77–80, 1998.

[68] I. D. Kaganovich and L. D. Tsendin, "Formation of discontinuities in multistage evolution associated with diffusion of a multicomponent weakly ionized hot-electron plasma," *Plas. Phys. Rep.*, vol. 19, pp. 645–650, 1993.

[69] J. T. Gudmundsson, I. G. Kouznetsov, K. K. Patel, and M. A. Lieberman, "Electronegativity of low-pressure high-density oxygen discharges," *J. Phys. D: Appl. Phys.*, vol. 34, pp. 1100–1109, 2001.

[70] R. N. Franklin, "Basic relationships in electronegative plasmas with a multiplicity of negative and positive ion species," *J. Phys. D: Appl. Phys.*, vol. 36, pp. 823–827, 2003.

[71] R. N. Franklin, "The effect of including the ion flux issuing from the core of an electronegative plasma on the electron temperature versus pressure characteristic," *Plas. Sour. Sci Technol.*, vol. 11, pp. 279–282, 2002.

[72] R. N. Franklin, "Basic relationships in electronegative plasmas with more than one species of negative ion," *J. Phys. D: Appl. Phys.*, vol. 35, pp. 536–542, 2002.

[73] H. J. Yoon and T. H. Chung, "One-dimensional analysis of electronegative discharge plamas with four charged species," *J. Korean Phys. Soc.*, vol. 34, pp. 29–35, 1999.

[74] A. Kono, "Negative ions in processing plasmas and their effect on the plasma structure," *Applied Surface Science*, vol. 192, pp. 115–134, 2002.

[75] B. Bezzerides, D. W. Forslund, and E. L. Lindman, "Existence of rarefaction shocks in a laser-plasma corona," *Phys. Fluids.*, vol. 21, pp. 2179–2185, 1978.

[76] L. M. Wickens and A. J. E, "Free expansion of a plasma with two electron temperatures," *J. Plas. Phys.*, vol. 22, pp. 167–185, 1979.

[77] G. Hairapetian and R. L. Stenzel, "Expansion of a two-electron-population plasma into vacuum," *Phys. Rev. Lett.*, vol. 61, pp. 1607–1610, 1988.

[78] G. Hairapetian and R. L. Stenzel, "Observation of a stationary, current-free couble layer in a plasma," *Phys. Rev. Lett.*, vol. 65, pp. 175–178, 1990.

[79] K. Sato and F. Miyawaki, "Formation of presheath and current-free double layer in a two-electron-temperature plasma," *Phys. Fluids B*, vol. 4, pp. 1247–1254, 1992.

[80] T. E. Sheridan, N. S. J. Braithwaite, and R. W. Boswell, "Relation between double layers and flux for a collisionless discharge with two negative components," *Phys. of Plas.*, vol. 6, pp. 4375–4381, 1999.

[81] V. I. Kolobov and D. J. Economou, "Ion-ion plasmas and double layer formation in weakly collisional electronegative discharges," *Appl. Phys. Lett.*, vol. 72, pp. 656–658, 1998.

[82] R. Deutsch and E. Rauchle, "Influence of negative ions on the plasma boundary sheath," *Phys. Rev. A*, vol. 46, pp. 3442–5453, 1992.

[83] A. Kono, "Formation of an oscillatory potential structure at the plasma boundary in electronegative plasmas," *J. Phys. D: Appl. Phys.*, vol. 32, pp. 1357–1363, 1999.

[84] T. E. Sheridan, "Double layers in a modestly collisional electronegative discharge," *J. Phys. D: Appl. Phys.*, vol. 32, pp. 1761–1767, 1999.

[85] I. G. Kouznetsov, A. J. Lichtenberg, and M. A. Lieberman, "Internal sheaths in electronegative discharges," *J. Appl. Phys.*, vol. 8, pp. 4142–4153, 1999.

[86] M. S. Benilov and R. N. Franklin, "Joining sheath to plasma in electronegative gases at low pressures using matched asymptotic approximations," *J. Plas. Phys.*, vol. 62, pp. 541–559, 1999.

[87] L. Schott, "Plasma boundary layer in the presence of fast primary electrons," *Phys. Fluids*, vol. 8, pp. 1795–1799, 1987.

[88] P. Chabert and T. E. Sheridan, "Kinetic model for a low-pressure discharge with negative ions," *J. Phys. D: Appl. Phys.*, vol. 33, pp. 1854–1860, 2000.

[89] K. U. Riemann, "The bohm criterion and sheath formation," *J. Phys. D: Appl. Phys.*, vol. 24, pp. 493–518, 1991.

[90] A. Kono, "Intrinsic sheath edge conditions for sheath instability in low-pressure electronegative plasmas," *J. Phys. D: Appl. Phys.*, vol. 36, pp. 465–472, 2003.

[91] A. Kono, "Complex sheath formation around a spherical electrode in electronegative plasmas: a comparison between a fluid model and a particle simulation," *J. Phys. D: Appl. Phys.*, vol. 34, pp. 1083–1090, 2001.

[92] R. Dendy, ed., *Plasma Physics: An Introductory Course.* Cambridge University Press, 1995.

[93] R. D. Hazeltine and F. L. Waelbroeck, *The Framework of Plasma Physics.* Perseus Books, 1998.

[94] J. M. Dawson, "Particle simulation of plasmas," *Rev. Mod. Phys.*, vol. 55, pp. 403–447, 1983.

[95] C. K. Birdsall and A. B. Langdon, *Plasma Physics via Computer Simulation.* Institute of Physics, 1991.

[96] W. H. Press, S. A. Teukolsky, W. T. Vetterling, and B. P. Flannery, *Numerical Recipes in C — The Art of Scientific Computing.* Cambridge University Press, 2nd ed., 1992.

[97] P. C. Boyle, *Modelling of Dual Frequency Capacitively Coupled Plasma Devices.* PhD thesis, Dublin City University, 2004.

[98] A. Jaun, "Numerical methods for partial differential equations — course notes." Online Course run by the Swedish Netuniversity, http://www.lifelong-learners.com/pde.

[99] M. Surendra, "Radiofrequency discharge benchmark model comparison," *Plas. Sources Sci. Technol.*, vol. 4, pp. 56–73, 1995.

[100] A. Meige, *Numerical Modeling of Low-Pressure Plasmas: Applications to Electric Double Layers.* PhD thesis, Australian National University, 2006. http://prl.anu.edu.au/Members/mdl112/thesis.pdf.

[101] M. M. Turner, "Kinetic properties of particle-in-cell simulations compromised by monte carlo collisions," *Phys. of Plas.*, vol. 51, p. 13:033506, 2006.

[102] M. Hayashi, "Technical report," *Nagoya Institute of Technology (unpublished)*, 1991.

[103] K. Tachibana, "Excitation of the $1s_5$, $1s_4$, $1s_3$, and $1s_2$ levels of argon by low-energy electrons," *Phys. Rev. A*, vol. 34, pp. 1007–1015, 1986.

[104] D. Rapp and P. Englander-Golden, "Total cross sections for ionization and attachment in gases by electron impact. 1. Positive ionization," *J. Chem. Phys.*, vol. 43, pp. 1464–1479, 1965.

[105] I. P. Zapesochny and L. L. Shimon, "Absolute excitation cross sections of alkali metals," *J. Appl. Phys.*, vol. 79, pp. 9379–9381, 1996.

[106] R. H. McFarland and J. D. Kinney, "Absolute cross sections of lithium and other alkali metal atoms for ionization by electrons," *Phys. Rev. A*, vol. 137, pp. A1058–A1061, 1965.

[107] L. Vriens, "Collision theory of ionization of atoms by electrons," *Phys. Lett.*, vol. 8, p. 260, 1964.

[108] A. V. Phelps, "The application of scattering cross section to ion flux models in discharge sheaths," *J. Appl. Phys*, vol. 76, pp. 747–753, 1994.

[109] A. V. Phelps, "Cross sections and swarm coefficients for nigrogen ions and neutrals in N_2 and argon ions and neutrals in Ar for energies from 0.1 ev to 10 kev," *J. Phys. Chem. Ref. Data*, vol. 20, pp. 557–573, 1991.

[110] A. V. Phelps, "Atomic and molecular data." JILA, NIST-CU, http://jilawww.colorado.edu/ avp/collision_data/.

[111] "Kinema research & software – air chemistry." Kinema url: http://www.kinema.com/download.htm.

[112] S. Trajmar, D. C. Cartwright, and W. Williams, "Differentaial and

integral cross sections for electron-impact excitation of the $a^1\Delta_g$ and $b^1\Sigma_g^+$ states of O_2," *Phys. Rev. A*, vol. 4, pp. 1482–1492, 1971.

[113] M. J. Mumma and E. C. Zipf, "Dissociative excitation of vacuum ultraviolet emission features by electron impact on molecular gases. 1. h_2 and o_2," *The Journal of Chemical Physics*, vol. 55, p. 1661, 1971.

[114] B. F. Gordiets, C. M. Ferreira, V. L. Guerra, J. Loureiro, J. Nahorny, D. Pagnon, M. Touzeau, and M. Vialle, "Kinetic-model of a low-pressure $N_2 - O_2$ flowing glow discharge," *IEEE Trans. Plas. Sci.*, vol. 34, pp. 755–766, 2006.

[115] E. Meeks, R. Larson, P. Ho, C. Apblett, S. M. Han, E. Edelberg, and E. S. Aydil, "Modeling of SiO_2 deposition in high density plamsa reactors and comparisons of model prediations with experimental measurements," *J. Vac. Sci. Technol. A*, vol. 16, pp. 544–563, 1998.

[116] B. M. Smirnov, ed., *Physics of Ionized Gases*. Wiley-VCH, 2001. Rates computed using polarizability theory.

[117] H. B. Valentini, "Sheath formation in low-pressure discharges," *Plas. Sourc. Sci. Tech.*, vol. 9, pp. 574–582, 2000.

[118] K. U. Riemann, "Kinetic analysis of the collisional plasma-sheath transition," *J. Phys. D: Appl. Phys.*, vol. 36, pp. 2811–2820, 2003.

[119] R. W. Boswell, "Bohm velocity with a two-temperature distribution of negative particles," *IEEE Trans. Plas. Sci.*, vol. 20, pp. 62–65, 1992.

[120] M. Zeuner and J. Meichsner, "High energy negative ions in a radio-frequency discharge," *J. Appl. Phys.*, vol. 79, pp. 9379–9381, 1996.

[121] M. Zeuner and H. Neumann, "Sputter process diagnostics by negative ions," *J. Appl. Phys.*, vol. 83, pp. 5083–5086, 1998.

[122] H. Amemiya, "Diagnostics of negative ions using probe and laser in plasmas (oxygen discharge)," *Vacuum*, vol. 58, pp. 100–116, 2000.

[123] S. Mraz and J. M. Schneider, "Energy distribution of O^- ions during reactive magnetron sputtering," *Appl. Phys. Lett.*, vol. 89, p. 051502, 2006.

[124] H. Amemiya, "Plasmas with negative ions — probe measurements and charge equilibrium," *J. Phys. D: Appl. Phys.*, vol. 23, pp. 999–1014, 1990.

[125] P. Chabert, T. E. Sheridan, R. W. Boswell, and J. Perrin, "Electrostatic probe measurement of the negative ion fraction in an SF_6 helicon discharge," *Plas. Sourc. Sci. Tehcnol.*, vol. 8, pp. 561–566, 1999.

[126] E. Meeks and J. Won Son, "Modeling of plasma-etch processes using well stirred reactor approximations and including complex gas-phase and surface reactions," *IEEE Trans. Plas. Sci.*, vol. 23, pp. 539–549, 1995.

[127] Y. T. Lee, M. A. Lieberman, A. J. Lichtenberg, F. Bose, H. Baltes, and R. Patrick, "Global model for high pressure electronegative radio-frequency discharges," *J. Vac. Sci. Technol. A*, vol. 15, pp. 113–126, 1997.

[128] R. Zorat and D. Vender, "Global model of a radiofrequency H_2 plasma in denise," *Plasma Sources Sci. Technol.*, vol. 9, pp. 161–168, 2000.

[129] T. Kimura and K. Ohe, "Global model of inductively coupled Ar plasmas using two-temperature approximation," *J. Appl. Phys.*, vol. 89, pp. 4240–4246, 2001.

[130] M. W. Kiehlbauch and D. B. Graves, "Modeling argon inductively coupled plasmass: The electron energy distribution function and metastable kinetics," *J. Appl. Phys.*, vol. 91, pp. 3539–3546, 2002.

[131] K. R. Stadler, V. R. J, G. Nersisyan, and W. G. Graham, "Modeling the chemical kinetics of high-pressure glow discharges in mixtures of helium with real air," *J. Appl. Phys.*, vol. 99, 2006.

[132] S. Ashida and M. A. Lieberman, "Spatially averaged (global) model of time modulated high density chlorine plasmas," *Jpn. J. Appl. Phys.*, vol. 36, pp. 854–861, 1997.

[133] J. T. Gudmundsson, "On the effect of the electron energy distribution on the plasma parameters of an argon discharge: a global (volume-averaged) model study," *Plas. Sourc. Sci. Technol.*, vol. 10, pp. 76–81, 2001.

[134] H. Amemiya, "Sheath formation criterion and ion flux for a non-maxwellian plasma containing negative ions," *J. Phys. Soc. Jap.*, vol. 67, pp. 1955–1962, 1998.

[135] J. T. Gudmundsson, T. Kimura, and M. A. Lieberman, "Model and measurements for a planar inductive oxygen discharge," *Plas. Sourc. Sci. Technol.*, vol. 7, pp. 1–12, 1998.

[136] V. A. Godyak, "Non-equilibrium eedf in gas discharge plasmas," *IEEE Trans. Plas. Sci.*, vol. 34, pp. 755–766, 2006.

[137] H. Singh and D. B. Graves, "Measurements of the electron energy distribution function in molecular gases in a shielded inductively coupled plasma," *J. Appl. Phys.*, vol. 88, pp. 3889–3898, 2000.

[138] S. Cho and M. A. Lieberman, "Local and global particle and power balance in large area capacitive discharges," *Plas. Sourc. Sci. Technol.*, vol. 12, pp. 244–254, 2003.

[139] A. J. Lichtenberg, "Private communication."